





THESIS 2 2003 54524267

LIBRARY

Microgan State
University

This is to certify that the dissertation entitled

CONSTITUTIVE MODELING FOR POLYCRYSTALLINE ALUMINUM ALLOY EXTRUSIONS AND APPLICATION TO HYDROFORMING OF THIN-WALLED TUBES

presented by

Yabo Guan

has been accepted towards fulfillment of the requirements for the

Ph.D. degree in Mechanical Engineering

Major Professor's Signature

8/6/03

Date

PLACE IN RETURN BOX to remove this checkout from your record. TO AVOID FINES return on or before date due. MAY BE RECALLED with earlier due date if requested.

DATE DUE	DATE DUE	DATE DUE
		EP 9 2 2004 011 2 05
		011 2 05
_		

6/01 c:/CIRC/DateDue.p65-p.15

CONSTITUTIVE MODELING FOR POLYCRYSTALLINE ALUMINUM ALLOY EXTRUSIONS AND APPLICATION TO HYDROFORMING OF THIN-WALLED TUBES

Ву

Yabo Guan

A DISSERTATION

Submitted to
Michigan State University
in partial fulfillment of the requirements
for the degree of

DOCTOR OF PHILOSOPHY

Department of Mechanical Engineering

2003

ABSTRACT

CONSTITUTIVE MODELING FOR POLYCRYSTALLINE ALUMINUM ALLOY EXTRUSIONS AND APPLICATION TO HYDROFORMING OF THIN-WALLED TUBES

By

Yabo Guan

Hydroforming of thin-walled hollow extrusions has become popular with automotive and materials industries for making complex structural components. Because most of the hydroformed parts are made with steel, very little research has been done on the hydroforming of extruded aluminum tubes, which are lighter and environmentally friendly. As for any forming operation, computer modeling, using finite element analysis (FEA), is today a common tool used at the design stage of the process. However, in order to obtain realistic predictions, accurate material descriptions (constitutive models) will be needed. In this work, several material models have been developed for accurate simulation of metal forming processes, specifically hydroforming of extruded aluminum tubes.

A Taylor-type polycrystalline model, based on a rate-independent single crystal yield surface and rigid plasticity, has been developed and implemented into ABAQUS/Explicit finite element (FE) code using VUMAT. It has served directly as a constitutive law in the FE to calculate the crystallographic texture evolution during the hydroforming of an extruded aluminum tube. Initial crystallographic texture measured with OIM and uniaxial tensile test results are input to this FEA model. Although very accurate in representing the material anisotropy, finite element analysis based on direct use of a polycrystal model is extremely CPU-intensive, making it unfeasible for design purposes.

To develop the most accurate phenomenological model for forming of extruded aluminum tubes, this polycrystal model was used to predict the anisotropy coefficients of Barlat's Yld96 yield function. This phenomenological anisotropic yield function was also implemented into ABAQUS/Implicit finite element code, using UMAT, for simulation of bulging and hydroforming of a 6061-T4 extruded aluminum tubes. It was shown that compared with von Mises and Hill's 1948 yield function, the Yld96 material model's predictions are in better agreement with experimental results.

In order to take into account the anisotropic hardening of aluminum tubes a new flow potential, as a function of the anisotropy coefficients and deviatoric stresses, was proposed. The evolution of the anisotropy coefficients was proposed to be a linear function of the strain path, with its proportionality constant determined from experimental measurements. This model was also implemented into ABAQUS/Implicit code and shown to be capable of predicting deformation strains very accurately. It is concluded that in the absence of experimental results or reliable data, the anisotropic model could be used at early design stage to evaluate the accuracy of the phenomenological models' predictions.

ACKNOWLEDGMENTS

I would like to express gratitude to major professor, Dr. Farhang Pourboghrat, for his instruction, guidance, patience and encouragement during the Ph.D. Study.

Special thanks are extended to Dr. Frédéric Barlat for his excellent support and valuable assistance through this work.

I would like to thank my committee members, Drs. R. Averill, T. Pence and M. Miklavcic for viewing this dissertation and for their valuable comments.

Thanks are due to the research members in our group, including Dr. W-R Yu, Dr. M. Zampaloni and Mr. N. Abedrabbo.

I would like to thank Mr. John Brem for providing valuable assistance to perform mechanical testing of 6111-T4 tubes, and Mr. Edward Llewellyn for conducting and analysis of Orientation Imaging Microscopy (OIM) of the aluminum tubes.

A final note of appreciate must go to my parents and my wife Haiyan for their support and encouragement through all these years.

Funding of this research by National Science Foundations is most gratefully acknowledged.

TABLE OF CONTENTS

LIST OF TABLES	vii
LIST OF FIGURES	viii
CHAPTER 1	
INTRODUCTION	1
1.1 What's Tube Hydroforming	1
1.2 Constitutive Models	2
1.3 Methodology	3
1.4 Literature Reviews	5
CHAPTER 2	
PRELIMINARY OF CRYSTAL PLASTICITY	11
2.1 Slip in Single Crystal	11
2.2 Deformation of Polycrystals	13
2.3 Self-hardening and Latent-hardening	16
CHAPTER 3	
POLYCRYSTAL MODELING BASED ON GAMBIN'S SINGLE CRYS	STAL MODEL
AND ITS APPLICATION TO FINITE ELEMENT ANALYSIS	18
3.1 Grain Orientation	19
3.2 Gambin's Single Crystal Model	20
3.3 Boundary Conditions	21
3.4 Strain Hardening	25
3.5 Spin and Rotation	27
3.6 Implementation into Finite Element Code	29
3.7 Verification of the Polycrystal Model	33
CHPATER 4	
PHENOMENOLOGICAL MODELING	49
4.1 Phenomenological Yield Function	49
4.2 Yld96 Yield Function	50
4.3 Material Characterization of 6061-T4 Extruded Aluminum Tube	52
4.4 Implementation of Barlat's Yld96 into ABAQUS	55
CHAPTER 5	
PHENOMENOLOGICAL MODELING WITH ANISOTROPIC STRAIN	1
HARDENING	64
5.1 Strain Hardening in Single Crystal and Polycrystal	64
5.2 Isotropic and Anisotropic Strain Hardening	65
5.3 Formulation for Prediction of Anisotropic Coefficients	66
5.4 Evaluation of the Anisotropic Strain Hardening Model	70

89
89
90
92
94
ESS CASE
98
OADING 104
114

LIST OF TABLES

Table 2-1 FCC single crystal vertices	16
Table 3-1 Dimensions and mechanical properties of the tube	37
Table 3-2 Sensitivity with respect to total simulation times (1 grain orientation, 10 elements)	39
Table 3-3 Sensitivity with respect to number of grain orientations (1.0ms, 10 elements)	4(
Table 3-4 Sensitivity with respect to number of grain orientations (10ms, 10 elements)	41
Table 3-5 Sensitivity with respect to number of elements (1 grain orientation, 1 ms)	42
Table 4-1 Yld96 yield function coefficients for 6061-T4 extruded aluminum tube	54
Table 5-1 Hoop strain at element 1421 & 1429 for different yield functions	79
moop strain at element 1421 & 1429 for different yield functions	/ >

LIST OF FIGURES

Figure 1-1 The orthogonal anisotropy axes of tube	10
Figure 2-1 Slip elements in uniaxial tension	12
Figure 3-1 Slip systems rotation when a crystal with only one slip system is subjected to extension	an 29
Figure 3-2 Rotation axis and angle corresponding to a spin $W - \Omega$	29
Figure 3-3 Pole figure (111) with 1005 grain orientations representing the undeformed tube	32
Figure 3-4a OIM pole figure representing the undeformed 6061-T4 aluminum tube	33
Figure 3-4b CODF for the undeformed 6061-T4 aluminum tube	33
Figure 3-5 Uniaxial tension simulation (one single element)	34
Figure 3-6 Comparison of experimental uniaxial tension strain/stress curve with those obtained by ABAQUS using polycrystal model (VUMAT)	, 35
Figure 3-7 Strain/stress curves predicted for uniaxial tension using polycrystal model outside of ABAQUS (100 of 100,000 increments from VUMAT were used)	36
Figure 3-8 Finite element model used for simulating the uniaxial tension test with ABAQUS/implicode	icit 86
Figure 3-9 Predicted strain/stress curves for uniaxial tension using polycrystal model outside of ABAQUS (all 508 increments from ABAQUS/implicit code were used)	37

Figure 3-10 Kinetic and internal energy histories for 10ms, 10 grain orientations, 10 elements simulation	42
Figure 3-11 Undeformed and deformed shape of bulged tube	43
Figure 3-12 Strain and stress distribution of the bulged tube (a) hoop strain, (b) axial strain, (c) hostress, (d) axial stress	op 43
Figure 3-13 (a) strain path from explicit simulation (10ms, 10 grain orientations) (b) strain path from implicit simulation (Yld96)	45
Figure 3-14 (111) pole figure after bulging (strain path obtained from ABAQUS/explicit)	47
Figure 3-15 (111) pole figure after bulging (strain path obtained from ABAQUS/implicit)	47
Figure 3-16 (111) pole figure after bulging obtained from OIM	47
Figure 3-17 (a) OIM pole figure representing the bulged 6061-T4 aluminum tube (b) CODF representing the bulged 6061-T4 aluminum tube	48
Figure 4-1 Experimental stress-strain curve measured in the extrusion direction (ED)	53
Figure 4-2 Stress vs. plastic work in various directions	53
Figure 4-3 Yield surface (Yld96) for 6061-T4 (plane stress case and shear stress is equal to zero)	54
Figure 4-4 Specimen used for uniaxial tensile test	55
Figure 4-5 Stress/strain curve comparison between experiment and Yld96	56
Figure 4-6 Hoop strain comparison for different yield functions	57

Figure 4-7 Deformation and strain/stress distribution for bulged tube	59
Figure 4-8 Corner region of the tube deformed in a square die (circle grids were used to measu strains)	re the 60
Figure 4-9 Major strain distribution comparison between numerical simulation and experiment	62
Figure 4-10 Deformed tube, square die and strain distribution (a) deformed tube (b)square die (c) axial strain (d) hoop strain	63
Figure 5-1 Predicted initial yield surface based on a 0.5% plastic strain offset for the 6061-T4 extruded aluminum tube	71
Figure 5-2 Yield surface based on von Mises model Yield surface based on isotropic hardening Yld96 model, α equal to zero Yield surface based on anisotropic hardening Yld96 model, α equal to -0.00001	74 75 76
Figure 5-3 Different strain paths predicted by different material models	77
Figure 5-4 (a) Strain paths for element #1429 (b) Strain paths for element #1421	78
Figure 5-5a-d Yield surfaces comparison based on different strain paths for element 1429	80-83
Figure 5-6a-d Yield surfaces comparison based on different strain paths for element 1421	84-87
Figure 5-7 Hoop strain distribution with different α -values	88
Figure 6-1 Experimental setup in MSU laboratory	90
Figure 6-2 The die set used for experiment	91

Figure 6-3 The principle of tube hydroforming (a) original tube shape and (b) final tube shape (before unloading)	91
Figure 6-4 Working diagram for the hydroforming process	92
Figure 6-5 Failure modes occurring in tube hydroforming	92
Figure 6-6 Deformed tubes without failure	93
Figure A1 (a) Axes and unit base vectors; (b) two-dimensional rotation; (c) small threstotation	ee-dimensional 97
Figure A2 Rotation of a vector r viewed as a rotation about a fixed axis $\theta = \theta$ e according theorem; on the right a top view along the axis θ is shown	ng to Euler' 97
Figure B1 Stress-strain curve (extrusion direction) from polycrystal simulation and exresult	xperimental
Figure B2 Boundary condition in different reference frames	102
Figure C1a-d Yield surface comparison for uniaxial tension (ED)	104-105
Figure C2a-d Yield surface comparison for uniaxial tension (TD)	106-107
Figure C3a-d Yield surface comparison for plane strain ($\varepsilon_{22} = 0$)	108-109
Figure C4a-d Yield surface comparison for plane strain ($\varepsilon_{11} = 0$)	110-111
Figure C4a-d Yield surface comparison for balanced biaxial tension	112-113

CHAPTER 1

INTRODUCTION

1.1What's Tube Hydroforming

Tube hydroforming has shown itself to be a competitive alternative to conventional stamping when producing tube-like components by reducing process steps and the overall production cost. Tube hydroforming also tends to improve the structural strength and stiffness of a component compared to those consisted of several stamped sheets. This allows weight reduction without losing component performance.

During a hydroforming process, a tube is first placed in the closed cavity of a forming die. After the ends of the tubes are sealed, the hydraulic fluid is injected into the inner of the tube and the tube is formed to conform the shape of the die cavity [Dohmann and Hartl 1997].

Hydroforming of thin-walled extrusion tubes is receiving the greatest attention, especially in the auto industry [Vari-Form Inc 1998], because existing multi-piece, stamped/welded assemblies in auto body and frame structures potentially can be replaced with less expensive hydroformed parts that are lighter, stronger and more precise. If components are manufactured from aluminum alloy tubes, this can translate into significant weight saving for the structure as well. Because most of the hydroformed parts are made with steel, very little research has been performed on hydroforming of aluminum alloy tubes. As for any forming operation, computer modeling (using finite element analysis) is today a major tool used at the design stage of the process. However, in order to obtain realistic predictions, accurate material descriptions (constitutive models) are needed to simulate hydroforming processes specifically for aluminum alloy tubes.

1.2 Constitutive Models

A constitutive model is necessary for the description of the material behavior in numerical simulations of any forming operations. Large plastic deformation taking place in the process requires using a plasticity model. The plasticity of materials can be described using two types of models: physical (based on crystallographic texture, dislocation, precipitate, solute, etc) and phenomenological.

1.2.1 Polycrystal Constitutive Model

Most man-made materials are an aggregate of crystals or 'polycrystals'. Their crystallographic orientation is generally non-random. All non-random orientation distributions are called preferred orientations or 'texture'. In textured polycrystals, many macroscopic physical (mechanical) properties are anisotropic, i.e. they depend on direction [Kocks UF, et al. 2000]. Plasticity is one of the most anisotropic of material behaviors. Plastic anisotropy of polycrystals arises from two causes: anisotropy of the single crystal's properties and texture. It is important to study the single crystal properties and the way in which grains interact in a polycrystal since it leads to a formulation of the constitutive relations to be used in the simulations of polycrystal plasticity.

Plastic deformation is one of the main causes of texture formation and change. Glide of many dislocations results in slip, which is the most common manifestation of plastic deformation in crystalline solids [Hull and Bacon, 1984]. Polycrystal plasticity embodies the slip systems and the crystallographic orientation (texture) in a constitutive framework that can be incorporated in numerical formulations for the analysis of the deformation process.

1.2.2 Phenomenological Constitutive Model

The basic of a phenomenological constitutive model comprises of a yield criterion representing a surface which separates the elastic and plastic regions of the stress space, a flow potential (yield function if it is associated) which its gradient represents the direction of the plastic strain, and a strain hardening rule.

1.2.3 Combination of Polycrystal Plasticity and FEM

Incorporation of polycrystal plasticity with finite element formulation can be grouped into two categories. One category includes those simulations that have a single orientation within each finite element. Elements represent crystals or portions of crystals. The second category includes simulations in which every element contains an approximation to the crystal orientation. The orientations in each element may number as few as only tens of grains, or may be in the thousands [Dawson and Marin 1998]. In this work we focus on the second category of the formulations.

1.3 Methodology

In this work, polycrystalline plasticity serves as a constitutive theory in essentially the same way as a continuum elasto-plasticity model. A rate-independent polycrystal model was used to calculate the texture evolution. This is based on a single crystal yield surface with round-off corners, first developed independently by Gambin (1991) and Arminjon (1991). Polycrystal behavior was based on the full constraint homogenization procedure (Taylor assumption). The crystallographic texture of aluminum that was used as input data in the polycrystalline was characterized experimentally using Orientation Imaging Microscopy (OIM).

The advantage of polycrystalline constitutive models is that they can predict anisotropic strain hardening effects due to the crystallographic texture evolution during the hydroforming process of tubes. However, in practice, numerical simulations using polycrystal models are difficult to perform and time-consuming; and, therefore, they can't be used at a design stage by process engineers. So a phenomenological constitutive model that can be implemented in the commercial code needs to be developed.

In the phenomenological constitutive theory, the plastic behavior is assumed to be well described with a yield surface that evolves during plastic deformation. For an aluminum alloy tube, only yield stress in extrusion direction (ED) (see Figure 1-1) can be measured and it is difficult to measure the yield stresses and r values (width to thickness strain ratio) in the tangential direction (TD), radial direction (RD), and 45° between ED and TD, which must be used for the prediction of the yield surface. Since the crystallographic texture of the aluminum can be characterized using OIM, we can use this crystallographic texture as input data for polycrystalline model to numerically determine the yield stresses and r-values in other three directions. Once these values are determined, the coefficients of yield function (which describe the yield surface) can be computed by solving a system of nonlinear equations, as described in the appendix B.

In order to take into account the anisotrpic hardening of aluminum tubes a new flow potential, as a function of the anisotropy coefficients and deviatoric stresses, was proposed. The evolution of the anisotropy coefficients was proposed to be a linear function of the strain path, with its proportionality constant determined from experimental measurements. This model was also implemented into ABAQUS/Implicit code and shown to be capable of predicting deformation strains very accurately. It is

concluded that in the absence of experimental results or reliable data, the polycrystal model could be used at early design stage to evaluate the accuracy of the phenomenological models' predictions.

1.4 Literature Reviews

1.4.1Polycrystal Plasticity

Quantitative descriptions of plastic flow by crystallographic slip have been developed during the past 100 years. One of the significant descriptions of them can be attributed to the work of Taylor and co-workers (1934,1938). Constitutive equation for elasto-plastic behavior of ductile single crystal from the standpoint of modern mechanics were first formulated by Mandel (1965) and Hill (1966), and extend to finite deformation by Rice (1971), Hill and Rice (1972), Asaro and Rice (1977), and Asaro (1983a,b). In these models, intended for low homologous temperatures, the plastic deformation of single crystals by crystallographic slip is idealized to be rate independent.

There have been three long-standing problems in the rate-independent theory of crystal plasticity. The first is to determine which slip systems are active and the second is to determine the increments of shear on the active slip systems. Third, because of the typical multiplicity of slip system in ductile crystals, the selection of slip systems required to produce an arbitrary deformation increment is not necessarily unique [Anand et al. 1996]. In order to overcome the slip system ambiguity problem in crystal plasticity, rate sensitive polycrystal models were developed and applied to deformation texture simulations [Bishop and Hill 1951a,1951b, Pan and Rice 1983, Asaro and Rice 1977, Asaro and Needleman 1985, Molinari et al. 1987, Becker 1991, Kalidindi et al. 1992,

Lebensohn and Tome 1993, Beaudoin et al. 1993, Tome and Canova 1998, Dawson and Beaudoin 1998, Dao and Li 2001].

However, the rate sensitivity is more introduced for numerical convergence issues than for accuracy in the physical description of aluminum alloys, which are usually not rate sensitive. In the context of rate independent plasticity, another approach using single crystal yield surface with rounded corners was proposed by Gambin to remove the ambiguity problem [Gambin 1991, 1992; Gambin and Barlat 1997]. Gambin was able to correlate a parameter of the single crystal yield surface to the stacking fault energy (SFE) of the material. The model was able to predict a different percentage of <100> fiber texture in axisymmetric extrusion for materials with different SFE. A polycrystal model based on Gambin's single crystal yield function has been used to predict the texture evolution during the hydroforming process of circular tube [Pourboghrat and Barlat 2002]. It also has been implemented into a finite element solver (ABAQUS) and served directly as constitutive law in the finite element analysis for calculating the evolution of crystallographic texture [Guan, Pourboghrat, and Barlat 2003].

In order to describe the relations between stress and motion at the microscopic scale and the corresponding quantities at the macroscopic scale, a number of micro-macro linking assumptions have been made. Most widely used and perhaps simplest one is the uniform strain assumption [Taylor 1938] that assumes all crystals experience identical strain equal to the macroscopic strain. This assumption ensures compatibility and provides an upper bound to the stress. The Sachs model [Sachs 1928], on the other hand, assumes proportional (not uniform) loading in the grains, and satisfies neither compatibility nor stress equilibrium. It is different from other so-called uniform stress assumption that

requires the stress to be identical from crystal to crystal [Ahzi et al. 1993]. This model gives the low bound to the stress. Self-consistent model [Molinari et al. 1987,1997; Lebensohn and Tome 1993; Tome and Canova 1998; Tome 1999] treats each grain as an inhomogeneity embedded in and interacting with a homogeneous effective medium (HEM). Self-consistent theory can give a solution that satisfies both compatibility and equilibrium.

1.4.2 Phenomenological Plasticity

In the phenomenological approach, the plastic behavior of metals is assumed to be well described by an analytical yield function. To account for the initial anisotropy, several anisotropic yield functions associated with isotropic strain hardening have been proposed. Hill's 1948 planar anisotropic quadratic yield function is certainly the most popular for describing the plastic behavior of orthotropic materials such as rolled steel sheets [Hill 1948]. It is an extension of the von Mises criterion for isotropic plasticity. Several non-quadratic yield functions were developed by Hill (1979,1990), Hershey (1954), Hosford (1972), Bassani (1977), Gotoh (1977), Logon and Hosford (1980), Barlat and Lian (1989), Barlat et al. (1991) and Karafillis and Boyce (1993).

These yield functions can be used to improve the yielding description for aluminum alloys. Hosford (1972) introduced an isotropic yield function based on the results of polycrystal calculations. Barlat and Lian (1989) proposed a non-quadratic yield function that introduces a coupling between normal and shear stress components, which is in agreement with findings based on polycrystalline plasticity theory. The criteria suggested by Barlat et al. (1991) account for six stress components that can be implemented to general three dimensional elasto-plastic continuum codes. The most accurate yield

function for aluminum alloy sheet was proposed by Barlat et al. (1997). This so-called Yld96 yield function simultaneously accounts for the anisotropy of uniaxial yield stresses and r-values. This yield function takes seven parameters into account in the plane stress condition. Lademo et al. (1999) evaluated three criteria proposed by Hill (1948), Barlat and Lian (1989) and Karafillis and Boyce (1993) based on the accurate measurements of the uniaxial behavior of aluminum alloys. Wu et al. (2003) predicted the anisotropic behavior of aluminum alloys using the 3-D yield criteria including Barlat et al. (1991,1997) and Karafillis and Boyce (1993). The evaluations of the yield functions were extended to the comparisons of the computed and experimental forming limit diagrams. Most recently, a new plane stress yield function Yld2000-2d [Barlat et al. 2003] that well describes the anisotropic behavior of sheet metal, in particular, aluminum alloy sheets, was proposed. Since it is based on the formulation using two linear transformations on the Cauchy stress tensor, convexity of yield surface could be proven which is an important requirement in numerical simulation to ensure the uniqueness of a solution.

1.4.3 Finite Element Analysis of Tube Hydroforming

Built on the successful application of the finite element method on sheet metal forming, a number of finite element formulation had been proposed to simulate the hydroforming process. In Hu et al. (1997), a rigid viscoplastic finite element formulation was developed to analyze the gas-pressure constrained bulging processes of superplastic circular sheets in cone disk shape dies. A computational method based on the membrane theory for the analysis of axisymmetric sheet metal forming processes such as punch stretching, deep drawing and hydroforming was presented in Hsu and Chu (1985). In Noh and Yang (1998) work, a general formulation for hydroforming of arbitrarily shaped boxes was

expressed. A finite element program based on rigid-plastic approach and the backward tracing scheme was developed for design in hydroforming [Kim et al. 2002].

In recent years, due to the advent of the high-speed computers, the use of 3D commercial finite element codes (LS-DYNA3D, ABAQUS etc) to model the complex hydroforming became possible. Simulations of forming different automotive parts by hydroforming process were carried out using LS-DYNA3D [Ni 1994; Wu et al. 1996; MacDonald et al. 2001; Trana 2002].

Formability analysis has become a subject of increasing interest in the hydroforming process. Davies et al. (2000) investigated the forming limits of aluminum extrusion AA6051 in both the T4 and T6 tempers under laboratory conditions. In Asnafi et al. (2000), forming limit curve (FLC) was determined by the hydroforming. Lei et al. (2002) predicted the bursting in tube hydroforming process by using rigid-plastic FEM combined with ductile fracture criterion.

Successful tube hydroforming depends on the reasonable combination of internal pressure and the axial feed load at the tube ends. Yang et al. (2001) dealt with the optimal process design of the hydroforming using numerical simulation by the explicit finite element code combined with an optimization tool. In Gelin et al. (2002), different approaches were proposed to find by numerical simulation and optimization the loading curve versus process parameters that minimize the thickness variations. Manabe et al. (2002) studied the effects of process parameter and material properties on deformation process in tube hydroforming.

Two-dimensional model can provide insight into the detailed deformation and stress/strain development otherwise lost in a more complex three-dimensional model.

Chen (2000) studied the tube expansion (also known as corner filling) based on two-dimensional plane stress model. Most recently Guan et al. (2003) and Sharma et al. (2003) proposed a "cross-section" analysis method for calculating tube stretching and bending followed by hydroforming and expansion to fill the die in the hydroforming process.

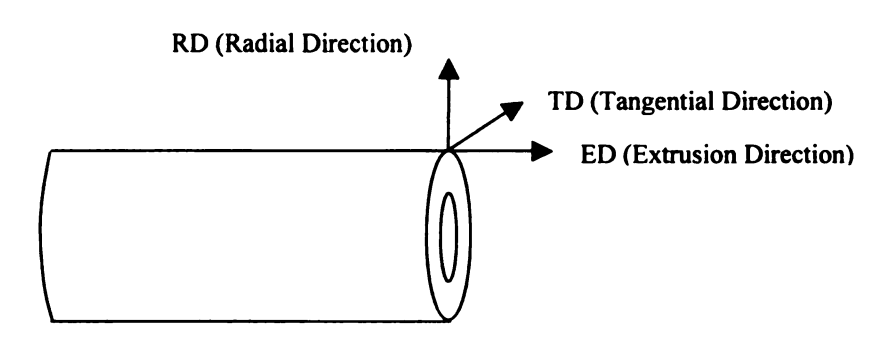


Figure 1-1 The orthogonal anisotropy axes of tube

CHAPTER 2

PRELIMINARY OF CRYSTAL PLASTICITY

In this chapter, basic concepts about crystal plasticity, such as slip system, Schmid law, Taylor assumption, self-hardening, latent hardening are introduced.

2.1 Slip in Single Crystal

It is necessary to introduce the slip in a single crystal because it is the primary deformation mechanism in most crystals. It involves the shearing on crystallographic planes in crystallographic directions. When a crystal is subjected to stress, slip begins when the resolved shear stress τ_{nd} on some slip system reaches a critical value, τ_c (called the critical resolved shear stress). This simple yield criterion for crystallographic slip is called Schmid's Law that can be expressed as the following:

$$\tau_{nd} = \tau_c \tag{2-1}$$

where subscripts n and d refer to the normal of slip plane and the slip direction respectively. If a crystal is subjected to the stress state of σ_{ij} , the shear stress on any slip system can be written as

$$\tau_{pq} = \sum_{i} \sum_{j} l_{pi} l_{qj} \sigma_{ij} = l_{pi} l_{qj} \sigma_{ij}$$
 (2-2)

 l_{pi}, l_{qj} are the direction cosines between the axes of the stress coordinate system and slip system. In a special case, Figure 2-1 shows a crystal with normal cross-section area A. A tensile load acting on it generates a uniaxial stress $P/A = \sigma_{xx}$. The resolved shear stress τ_{nd} in the slip plane n and along the slip direction p can be found from Eq.2-2.

$$\tau_{nd} = l_n l_{dr} \sigma_{xx} \tag{2-3}$$

Defining λ as the angle between the slip direction and the tensile axis, and ϕ as the angle between the tensile axis and the slip plane normal, the Schmid's Law for this special case may be expressed as

$$\tau_c = \sigma_r \cos \lambda \cos \varphi \tag{2-4}$$

or

$$\sigma_{\rm r} = \tau_{\rm c}/m_{\rm r} \tag{2-5}$$

where the Schmid factor $m_x = \cos \lambda \cos \varphi$.

The combination of slip plane and its direction of slip is known as a slip system. There are 12 slip systems (<110>/{111}) in the face-centered cube crystal (e.g. aluminum). <110> denotes the slip directions on the slip plane and {111} denotes the normal of the slip plane.

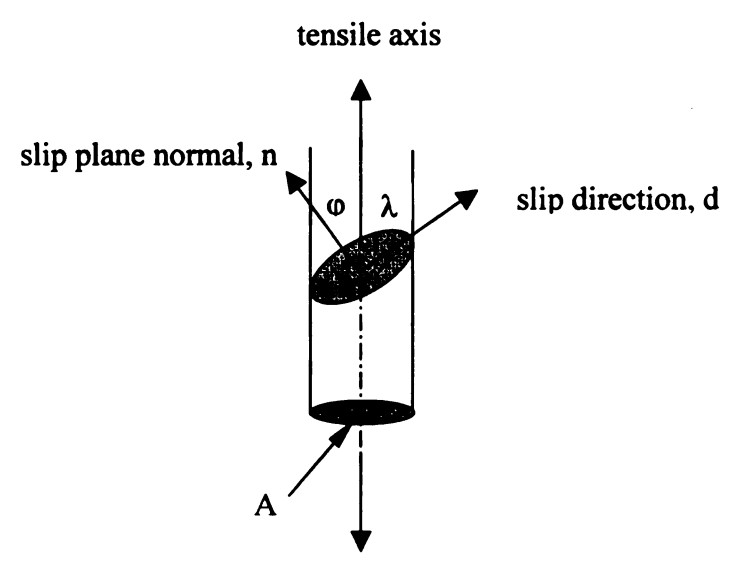


Figure 2-1 slip elements in uniaxial tension

It can be proven that, for all FCC crystals, all orientations within the so-called basic stereographic triangle (bounded by [100],[110], and [111] corners), the Schmid factor for

slip system <110>/{111}is higher than for other system. This slip system is known as primary slip system.

2.2 Deformation of Polycrystals

The mechanical properties of polycrystal are very different from single crystals. Slip on a single slip system cannot occur in a polycrystal because deformation in the various grains has to be compatible.

2.2.1 Independent Slip Systems in Polycrystals

For any FCC (face centered cubic) crystal with tensile axis inside the basic stereographic triangle, the deformation should occur at the primary slip system. However, if this crystal is surrounded by other crystals with different crystallographic orientations (in the polycrystalline aggregate), the strain taking place in the first crystal would have to be compatible with the strain in the other crystals (grains). Von Mises (1928) stated that five independent slip systems are required to produce a general homogenous strain in a crystal by slip. It can be presented as the following: since the plastic flow generally occurs without volume change (incompressibility of plastic deformation), therefore, $\varepsilon_{11} + \varepsilon_{22} + \varepsilon_{33} = 0$. This relationship reduces the components of strain from six $(\varepsilon_{11}, \varepsilon_{22}, \varepsilon_{33}, \varepsilon_{12}, \varepsilon_{23}, \varepsilon_{31})$ to five. Therefore, five independent slip systems are required for the deformation of one grain in a polycrystalline aggregate [Meyers et al. 1984].

2.2.2 Taylor Analysis

The deformation of polycrystal is much more complicated than that of single crystals, and great efforts have been devoted to bridge the gap between mechanical behaviors of single crystal and polycrystals.

Sachs (1928) proposed that the tensile yield strength of a polycrystal should be the average of the tensile yield strength of the crystal. It is also called lower-bound analysis. This idea assumes that only one slip system is active in each grain. In fact, when a polycrystal deforms, the shape change in each grain must be compatible with that of the neighboring grains. Such shape compatibility cannot be maintained by single slip. Consequently, Sachs analysis underestimates the polycrystalline stress-strain curve.

In order to satisfy this compatibility, Taylor (1938) proposed that all the grains undergo the same shape change as the entire polycrystal, namely, all crystals experience identical strain equal to the macroscopic strain. It is also called upper-bound analysis.

He assumed that this strain was imparted to each grain by the operation of five independent slip systems. Since the FCC structure has 12 slip systems, there are 792 different ways of choosing 5 slip systems from a group of 12 using the combination theory ($\frac{12!}{5!7!}$). Many of the 792 slip system combinations are not possible because they can't produce 5 independent strains. Taylor (1938) searched all the possible combinations and calculated the set of five Schmid factors (M_i) for the various slip systems based on the assumption that the critical stress for slips is the same for all active slip systems. He obtained the average \overline{M} (for FCC) over all orientations of the tensile axis and found:

$$\sigma = \overline{M}\tau = 3.06\tau$$

$$\varepsilon = \gamma / \overline{M} = \gamma / 3.06 \tag{2-6}$$

where τ is the critical stress for slip, γ is the accumulated shear strain for all active slip systems. σ and ε are the macroscopic average stress and strain respectively.

This relationship is very important for the later strain hardening analysis in the polycrystal modeling.

2.2.3 Bishop and Hill Analysis

Taylor's analysis can find the slip systems that geometrically produce a specified shape change. However, it cannot be guaranteed if there is a stress state that could physically activate the required slip systems. Bishop and Hill (1951a, 1951b) approached the problem by considering the stress states capable of simultaneously activating five or more slip systems. They found that, for FCC crystals, there are only 28 such stress states. They used the principle of maximum virtual work to determine which of the 28 stress states (or their negatives) would be appropriate for a given shape change. These so-called Bishop and Hill vertices lie on the single crystal yield surface obeying the Schmid's Law. Since these 28 stress states are used as the initial stress guess in the polycrystal modeling calculation that will be discussed in the Chapter 3, it is essential to discuss Bishop and Hill vertices that are listed by Bishop (1953).

These 28 stresses are also reproduced below in terms of A, B, C, F, G and H (see definition below). The corresponding stress states are:

$$s_{11} = (C - B)/3$$
 $s_{22} = (A - C)/3$ $s_{33} = (B - A)/3$ $s_{23} = F$ $s_{31} = G$ $s_{12} = H$ (2-7)

#	$A = s_{22} - s_{33}$	$B = s_{33} - s_{11}$	$C = s_{11} - s_{22}$	$F = s_{23}$	$G = s_{31}$	$H = s_{12}$
1	1	-1	0	0	0	0
2	0	1	-1	0	0	0
3	-1	0	1	0	0	0
4	0	0	0	1	0	0
5	0	0	0	0	1	0
6	0	0	0	0	0	11
7	1/2	-1	1/2	0	1/2	0
8	1/2	-1	1/2	0	- 1/2	0
9	-1	1/2	1/2	1/2	0	0
10	-1	1/2	1/2	- 1/2	0	0
11	1/2	1/2	-1	0	0	1/2
12	1/2	1/2	-1	0	0	- 1/2
13	1/2	0	- 1/2	1/2	0	1/2
14	1/2	0	- 1/2	- 1/2	0	1/2
15	1/2	0	- 1/2	1/2	0	- 1/2
16	1/2	0	- 1/2	- 1/2	0	- 1/2
17	0	- 1/2	1/2	0	1/2	1/2
18	0	- 1/2	1/2	0	- 1/2	1/2
19	0	- 1/2	1/2	0	1/2	- 1/2
20	0	- 1/2	1/2	0	- 1/2	- 1/2
21	- 1/2	1/2	0	1/2	1/2	0
22	- 1/2	1/2	0	- 1/2	1/2	0
23	- 1/2	1/2	0	1/2	- 1/2	0
24	- 1/2	1/2	0	- 1/2	- 1/2	0
25	0	0	0	1/2	1/2	- 1/2
26	0	0	0	1/2	- 1/2	1/2
27	0	0	0	- 1/2	1/2	1/2
28	0	0	0	1/2	1/2	1/2

Table 2-1 FCC single crystal vertices (from Bishop, 1953)

2.3 Self-hardening and Latent-hardening (Asaro RJ, 1983c)

As mentioned before, grains (crystals) deform inhomogeneously, i.e. only certain planes in the family of possible slip planes undergo slip. Moreover, the slip would disrupt the imperfections (dislocations), which in turn would make it more difficult to activate further slip and thus cause strain hardening [Ewing and Rosenhain 1900].

Strain hardening that occurs on the active slip system is called "self-hardening". The individual slip systems harden with strain and that slip on one slip system hardens other slip systems, even if the latter are not active. This is known as "latent hardening".

Two very important aspects of crystal strain hardening were stated in Taylor and Elam (1925): (1) Slip systems are hardened by slip on other systems (whether they themselves are active or not) and (2) this latent hardening is at least comparable in magnitude to self-hardening.

A rate-independent hardening rule can be written as

$$d\tau_c^{(\alpha)} = \sum_{\beta} h_{\alpha\beta} d\gamma^{(\beta)} \tag{2-8}$$

where $\tau_c^{(\alpha)}$ is the current yield strength on the α slip system, and $h_{\alpha\beta}$ the hardening rates. The off-diagonal terms in the matrix **h** represent latent hardening.

If the latent-hardening rates is assumed to be equal to self-hardening rate i.e. $h_{\alpha\beta}=h$ for all α and β , isotropic hardening is assumed. However, experiments actually indicate that the latent-hardening rate is slightly larger than the self-hardening rate.

CHAPTER 3

POLYCRYSTAL MODELING BASED ON GAMBIN'S SINGLE CRYSTAL MODEL AND ITS APPLICATION TO FINITE ELEMENT ANALYSIS

In the polycrystalline approach, the material is assumed to be a polycrystal consisting of many single crystals (grains). Plastic flow is assumed to occur only by crystalline slip on given slip systems within each crystal. A homogenization scheme is necessary in order to calculate the plastic response of a polycrystalline aggregate. Taylor scheme in which the strain rate is considered to be identical in each single crystal and equal to the macroscopic strain rate was used. The yield stress is derived from polycrystal calculations as an averaged behavior over the total number of single crystals. This approach can be used to take crystallographic texture evolution into account during forming operations. Some specifications about the treatment of polycrystals are considered [Besdo et al., 2001]:

- (1) The polycrystal consist of N crystallites (grains) with equal volume, though grain size is known to have a consistent effect on the yield stress and work hardening.
- (2) The statistical orientation of each crystal is given by the Euler angles θ , ϕ , ψ . No information about the spatial arrangement of the crystals in polycrystal is available.
- (3) Elastic anisotropy is neglected, namely, Young's moduli remain constant along different orientation.

In this chapter, a Taylor type (full constraint homogenization scheme) polycrystalline model, based on a rate-independent single crystal yield function will be described. This polycrystal model was directly implemented into a finite element (FE) program as a constitutive law to calculate the crystallographic texture development during the

hydroforming of extruded aluminum tubes. Crystallographic texture measured using Orientation Imaging Microscopy (OIM) and uniaxial tensile test results were used as input to this FEA model. In order to efficiently and practically simulate the tube hydroforming process using the polycrystal model through the explicit finite element code, texture discretization (grain number), loading rate (step time) and element size sensitivities were studied.

3.1 Grain Orientations

A global reference frame, \mathbf{x}_1 , \mathbf{x}_2 and \mathbf{x}_3 are given where a load or a velocity field is applied. Each grain is described by the orientation of its crystallographic axes, \mathbf{c}_1 , \mathbf{c}_2 and \mathbf{c}_3 , and an orthogonal transformation matrix $\mathbf{P} = [p_{ij}]$ as:

$$\begin{bmatrix} \mathbf{x}_1 \\ \mathbf{x}_2 \\ \mathbf{x}_3 \end{bmatrix} = \mathbf{P} \begin{bmatrix} \mathbf{c}_1 \\ \mathbf{c}_2 \\ \mathbf{c}_3 \end{bmatrix} \tag{3-1}$$

The components of a vector \mathbf{v} are denoted by v_i in \mathbf{x}_1 , \mathbf{x}_2 and \mathbf{x}_3 (global frame) and \mathbf{v}_i' in \mathbf{c}_1 , \mathbf{c}_2 and \mathbf{c}_3 (crystal frame). The components of a tensor \mathbf{T} are denoted by t_{ij} in \mathbf{x}_1 , \mathbf{x}_2 and \mathbf{x}_3 and t_{ij}' in \mathbf{c}_1 , \mathbf{c}_2 and \mathbf{c}_3 . The relationships between the components in the two frames are

$$[v'_{i}] = [p_{ij}]^{T} [v_{j}] \text{ and } [v_{i}] = [p_{ij}][v'_{j}]$$

$$[t'_{ii}] = [p_{ik}][t_{kl}][p_{ii}] \text{ and } [t_{ii}] = [p_{ik}][t'_{kl}][p_{ii}]$$
(3-2)

Among the many ways to represent an orientation, the Euler angles are well accepted. Roe's Euler angles define the orientation of a grain, whose crystal axes (c_1, c_2) and (c_3) are initially superimposed on the global reference frame (\mathbf{x}_1 , \mathbf{x}_2 and \mathbf{x}_3). This grain is then subjected to the succession of three rotations, first around $\mathbf{z} = \mathbf{c}_3$, then around \mathbf{c}_2 , and finally around \mathbf{c}_3 . The corresponding transformation matrix \mathbf{P} is

$$\mathbf{P} = \begin{bmatrix} \cos\psi\cos\theta\cos\varphi - \sin\psi\sin\varphi & -\cos\psi\cos\theta\sin\varphi - \sin\psi\cos\varphi & \cos\psi\sin\theta \\ \sin\psi\cos\theta\cos\varphi + \cos\psi\sin\varphi & -\sin\psi\cos\theta\sin\varphi + \cos\psi\cos\varphi & \sin\psi\sin\theta \\ -\sin\theta\cos\varphi & \sin\theta\sin\varphi & \cos\theta \end{bmatrix}$$
(3-3)

3.2 Gambin's Single Crystal Model

This model is based on the single crystal yield surface with round-off corners, first developed independently by Gambin (1991) and Arminjon (1991). Because of the absence of a sharp vertex, there is no ambiguity in the selection of the slip systems. This single crystal model is rate-independent and suitable for aluminum that is not very sensitive to the strain rate.

This model is time independent with a yield function and an associated flow rule

$$\varphi = \sum_{s} \left| \frac{\tau^{s}}{\tau_{c}^{s}} \right|^{a} = 1 \tag{3-4}$$

where τ_c^s is called critical value of the slip system "s" and τ^s is the resolved shear stress on a slip system "s", defined by the slip plane **n** and the slip direction **b**

$$\tau^s = b_i^s n_i^s s_{ii} \tag{3-5}$$

where is s_{ij} the deviatoric stress tensor. For convenience, a homogeneous function of degree one can be used for the yield function

$$\phi = \varphi^{\frac{1}{a}} \tag{3-6}$$

The associated flow rule $L_{ij}^c = \dot{\lambda} \frac{\partial \phi}{\partial s_{ij}}$ gives the rate of deformation $\mathbf{D}^c = [d_{ij}^c]$ tensor and

the plastic spin tensor $\mathbf{\Omega}^c = [\omega_{ij}^c]$

$$d_{ij}^{c} = \frac{\dot{\lambda}}{2} \left(\frac{\partial \phi}{\partial s_{ij}} + \frac{\partial \phi}{\partial s_{ji}} \right) \qquad \text{(symmetric part of } L_{ij}^{c} \text{)}$$

$$\omega_{ij}^{c} = \frac{\dot{\lambda}}{2} \left(\frac{\partial \phi}{\partial s_{ij}} - \frac{\partial \phi}{\partial s_{ji}} \right) \qquad \text{(anti-symmetric part of } L_{ij}^{c} \text{)}$$

The plastic spin tensor expresses the rotation rate of the crystal axes with respect to the principal deformation axes of the crystal. The superscript c denotes the crystal frame.

Note that because τ and ϕ are both first degree homogeneous functions of s_{ij} the plastic work rate can be written as follows

$$\dot{w} = d_y s_y = \dot{\lambda} \frac{\partial \phi}{\partial s_{ii}} s_{ij} = \dot{\lambda} \frac{\partial \phi}{\partial \tau^s} \frac{\partial \tau^s}{\partial s_{ii}} s_{ij} = \dot{\lambda} \frac{\partial \phi}{\partial \tau^s} \tau^s$$
(3-9)

Therefore, the shear rate on each system is given by

$$\dot{\gamma}^{s} = \dot{\lambda} \frac{\partial \phi}{\partial \tau^{s}} = \dot{\lambda} \frac{\phi^{1-a}}{\tau_{c}^{s}} \frac{\tau^{s}}{\tau_{c}^{s}} \left| \frac{\tau^{s}}{\tau_{c}^{s}} \right|^{a-2}$$
(3-10)

3.3 Boundary Conditions

The boundary conditions can be stress-imposed, strain-imposed or mixed. In any case, the material response consists of the set of a stress tensor S, a rate of deformation tensor D and a spin tensor W. Whatever boundary condition imposed, these three tensors are

known after a time increment. The upper bound (Taylor) model will be described in this section.

3.3.1 Taylor Model

The proposed formulation of the Gambin single crystal plasticity may be directly introduced into the upper-bound polycrystal model proposed by Taylor (1938). It is assumed the global kinematical field is imposed on all the grains and the Cauchy stress of polycrystal can be taken as a single number arithmetic average of Cauchy stress in the various grains.

3.3.2 Strain Imposed Boundary Condition

A velocity gradient in a global reference frame x_1 , x_2 , and x_3 can be decomposed into a rate of deformation tensor and a spin tensor

$$L^{g} = [v_{i,j}] = D^{g} + W^{g}$$
 (3-11)

The superscript denotes the global frame. For one crystal, the rate of deformation tensor D^g is imposed and model gives crystal stress S^c and Ω^c , the plastic spin. The Taylor assumption is now enforced i.e. the crystal rate of deformation, D^c , is identical to the global rate of deformation D^g . In the crystal frame, it can be written as

$$\mathbf{P}^T \mathbf{D}^g \mathbf{P} = \mathbf{D}^c \tag{3-12}$$

 Ω^c is different for each grain whereas W^g does not depend on a particular grain. After an incremental time step dt, the principal rate of deformation axes rotates by the quantity $W^g dt$ with respect to the global frame. At the same time, the crystal rotate by $-\Omega^c dt$ with respect to the principal rate of deformation axes. The net result is a rotation

of the crystal by the quantity $(P^TW^gP - \Omega^c)dt$ in the crystal frame. The polycrystalline stress deviator, Σ , is the arithmetic average of the stress deviator in each grain

$$\Sigma = \frac{1}{N_g} \sum_{g} S^g \tag{3-13}$$

where $S^g = PS^cP^T$.

3.3.3 Non-linear System of Equations for Taylor Model

Because the yield function is highly non-linear, the stress in each grain is obtained numerically using a non-linear solver, Newton-Raphson. There are 6 unknowns, the 5 components of the stress deviator and λ . One equation indicates that yield function is satisfied and five equations give the rate of deformation tensor. The system to solve is given by

$$F_1 = \lambda \partial \phi / \partial s_{11} - d_{11} = 0 \tag{3-14-1}$$

$$F_2 = \dot{\lambda} \partial \phi / \partial s_{22} - d_{22} = 0 \tag{3-14-2}$$

$$F_3 = \phi - \phi^{\bullet} = 0 \tag{3-14-3}$$

$$F_4 = \dot{\lambda}(\partial \phi / \partial s_{23} + \partial \phi / \partial s_{32}) - 2d_{23} = 0$$
 (3-14-4)

$$F_5 = \dot{\lambda}(\partial \phi / \partial s_{31} + \partial \phi / \partial s_{13}) - 2d_{31} = 0$$
 (3-14-5)

$$F_6 = \lambda (\partial \phi / \partial s_{12} + \partial \phi / \partial s_{21}) - 2d_{12} = 0$$
 (3-14-6)

where the d_{ij} are the components of D which is imposed to the crystal. Using the vector notation for the tensor (with indices $_{11}$, $_{22}$, $_{33}$, $_{23}$, $_{31}$, $_{12}$, $_{32}$, $_{13}$, $_{21}$), the following derivatives are used for calculating the flow rule and the Jacobian matrix of the non-linear system

$$\frac{\partial \phi}{\partial s_i} = \frac{1}{a} \frac{\phi}{\varphi} \frac{\partial \varphi}{\partial s_i}, i = 1 \text{ to } 9$$
 (3-15-1)

$$\frac{\partial^2 \phi}{\partial s_j \partial s_i} = \frac{1}{a} \frac{\phi}{\varphi} \left[\frac{\partial^2 \varphi}{\partial s_j \partial s_i} - \frac{(a-1)}{a\varphi} \frac{\partial \varphi}{\partial s_i} \frac{\partial \varphi}{\partial s_j} \right], i = 1 \text{ to } 9, j = 1 \text{ to } 9$$
 (3-15-2)

where

$$\frac{\partial \varphi}{\partial s_i} = a \sum_{s} \frac{m_i^s}{\tau_c^s} \frac{\tau^s}{\tau_c^s} \left| \frac{\tau^s}{\tau_c^s} \right|^{a-2}, i = 1 \text{ to } 9$$
(3-16-1)

$$\frac{\partial^2 \varphi}{\partial s_j \partial s_i} = a(a-1) \sum_s \frac{m_i^s}{\tau_c^s} \frac{m_j^s}{\tau_c^s} \left| \frac{\tau^s}{\tau_c^s} \right|^{a-2}, i = 1 \text{ to } 9, j = 1 \text{ to } 9$$
 (3-16-2)

For the first step, several types of initial estimate for the linear solver can be imposed. The Bishop and Hill vertex (Chapter 2) corresponding to maximum plastic work rate for the imposed rate of deformation, or the rate of deformation itself can be used. If there is a convergence problem, the solution can be obtained for a series of exponents, starting at a = 2 (easy convergence) and finishing at the desired exponent. In this method, the solution obtained for an exponent 'a' serves as the initial estimate for iterations with the next exponent. Finally, if all of the above estimates do not lead to a good convergence, the solution for the highest known exponent (less than a) can be used as a reasonable approximation.

For the next steps, the solution for the previous step can be used as the initial estimate in addition to the initial estimates discussed above. The initial estimate for $\dot{\lambda}$ is obtained from the Euler theorem for homogenous functions,

$$s_{ij}\frac{\partial \phi}{\partial s_{ij}} = \phi \tag{3-17}$$

because ϕ is homogeneous of degree one. As a consequence, the initial estimate for $\dot{\lambda}$ is

$$\dot{\lambda} = s_{ij} d_{ij} / \phi^* \tag{3-18}$$

3.4 Strain Hardening

The classical strain hardening law is used in this work. In the time interval dt, the critical resolved shear stress and accumulated shear strain increases on each slip system for a given grain, where $\dot{\tau}_c^r dt$ and $\dot{\gamma}^s dt$, are related through the following expression

$$d\tau_c^r = \sum_s \frac{\partial \tau_c^r}{\partial \dot{\gamma}^s} d \left| \gamma^s \right| \tag{3-19}$$

In the absence of any information concerning hardening, it is reasonable to assume isotropic hardening, i.e., all the partial derivatives are equal. As a result,

$$d\tau_c^r = d\tau_c = h\left(\sum_s \left|\gamma^s\right|\right) \sum_s d\left|\gamma^s\right| = h(\Gamma) d\Gamma$$
 (3-20)

where Γ is the accumulated slip and **h** the rate of hardening for a grain. However, experiments on single crystals (for instance, Franciosi, 1980) report that latent hardening can be higher than self-hardening, i.e., the hardening matrix off-diagonal components are larger than diagonal components. This trend is also suggested by cross-loading experiments on polycrystalline materials (for instance, Sang and Lloyd, 1979; Lloyd and Sang, 1979). Sequences of tension followed by simple shear in a manner that new slip systems become activated on reloading lead generally in higher flow stresses (Lopes et al., 2003). Therefore, for anisotropic hardening, it can be assumed that

$$\frac{\partial \tau_c^r}{\partial \dot{\gamma}^s} = h(\Gamma) H_{rs} \tag{3-21-1}$$

with

$$h(\Gamma) = \frac{dH(\Gamma)}{d\Gamma} \tag{3-21-2}$$

where H is the shear stress – shear strain curve and H_{rs} are the components of a matrix with constant coefficients. The critical resolved shear stress change is therefore given by

$$d\tau_c' = h(\Gamma) \sum_s H_{rs} d \left| \gamma^s \right| \tag{3-22}$$

the shear rate on a system is

$$\dot{\gamma}^s = \dot{\lambda} \phi^{1-a} \frac{\tau^s}{\left(\tau_c^s\right)^2} \left| \frac{\tau^s}{\tau_c^s} \right|^{a-2}$$
 (3-23)

As an application, the shear stress-shear strain curve H and the rate of hardening h can be given by the Voce law

$$H(\Gamma) = A' - B' \exp(-C'\Gamma)$$
 (3-24)

$$h(\Gamma) = B'C' \exp(-C'\Gamma) \tag{3-25}$$

If the macroscopic stress – strain curve of a material can be described by a macroscopic Voce law

$$\sigma = A - B \exp(-C\varepsilon) \tag{3-26}$$

the coefficients A', B' and C' can be roughly approximated from A, B and C, assuming a constant Taylor factor M equal to 3 ($\sigma = M\tau$, $\Gamma = M\varepsilon$, see Chapter 2)

$$A' = A/M$$
 $B' = B/M$ $C' = C/M$ (3-27)

Finally, if the normalized hardening matrix H is assumed to contain only two coefficients, p and q that characterize self hardening and latent hardening, respectively, the critical resolved shear stress changes are given by

$$d\tau_c^s = \left[\left(p - q \right) d\gamma^s + q d\Gamma \right] h(\Gamma) \tag{3-28}$$

3.5 Spin and Rotation

3.5.1 Plastic Spin

Figure 3-1 shows an example of a crystal with only one slip system subjected to an extension to illustrate how the lattice rotates during the plastic deformation. More generally, the plastic spin is given by

$$\omega_{ij} = \frac{\lambda}{2a} \frac{\varphi}{\phi} \left(\frac{\partial \phi}{\partial s_{ij}} - \frac{\partial \phi}{\partial s_{ji}} \right)$$
 (3-29)

3.5.2 Total Spin

The total spin for a grain with respect to the global frame is $W - \Omega$. This is an antisymmetric tensor, which operating on a vector \mathbf{v} , gives the rate of change of this vector (Fig. 3-2). The new crystal axes are given by $\tilde{\mathbf{c}}_{\mathbf{i}} = \mathbf{c}_{\mathbf{i}} + \mathbf{d}\mathbf{c}_{\mathbf{i}} = (I + W - \Omega)\mathbf{c}_{\mathbf{i}}$

However, in a time step dt, the new vectors $\mathbf{c_1} + \mathbf{dc_1}$, $\mathbf{c_2} + \mathbf{dc_2}$ and $\mathbf{c_3} + \mathbf{dc_3}$ do not keep their orthonormal property. Therefore, it is better to find the rotation axis and angle, and to operate the pure rotation on the crystal axes. It is easy to show that there is only one eigenvalue for the tensor $I + W - \Omega$, $\mu = 1$, which corresponds to the rotation axis, \mathbf{r} . Then, the eigenvectors can be calculated. Another way to calculate the rotation vector is to write the spin matrix $\mathbf{O} = W - \Omega$ as a matrix (see A8 in Appendix-A) made of three vectors $\mathbf{o_1}$, $\mathbf{o_2}$ and $\mathbf{o_3}$

$$\mathbf{O} = \mathbf{W} - \mathbf{\Omega} = \begin{bmatrix} \mathbf{o}_1 & \mathbf{o}_2 & \mathbf{o}_3 \end{bmatrix} = \begin{bmatrix} 0 & \mathbf{o}_{12} & -\mathbf{o}_{31} \\ -\mathbf{o}_{12} & 0 & \mathbf{o}_{23} \\ \mathbf{o}_{31} & -\mathbf{o}_{23} & 0 \end{bmatrix}$$
(3-30)

It can be shown that the rotation axis is

$$r = o_2 \times o_3 / |o_2 \times o_3|$$
, or $r = o_3 \times o_1 / |o_3 \times o_1|$, or $r = o_1 \times o_2 / |o_1 \times o_2|$ (3-31)

The rotation angle is (Fig. 3-2)

$$tg\xi_{i} = sign(\mathbf{r.c_{i}} \times d\mathbf{c_{i}})|d\mathbf{c_{i}}|/\sqrt{1-(\mathbf{r.c_{i}})^{2}}$$
(3-32)

where $d\mathbf{c_i} = O\mathbf{c_i}$. As for the rotation axis, there are three possible ways to calculate ξ_i , depending on the choice of $\mathbf{c_i}$. In order to calculate the new transformation matrix \mathbf{P} after rotation, it is necessary to calculate the coordinates of the vectors $\tilde{\mathbf{c_i}}$ rotated from $\mathbf{c_i}$ by ξ_i (see A-13 in Appendix-A)

$$\tilde{\mathbf{c}}_{\mathbf{i}} = \cos \xi \mathbf{c}_{\mathbf{i}} + (\mathbf{r}.\mathbf{c}_{\mathbf{i}})(1 - \cos \xi)\mathbf{r} + \sin \xi \mathbf{r} \times \mathbf{c}_{\mathbf{i}} = Q_{i1}\mathbf{c}_{1} + Q_{i2}\mathbf{c}_{2} + Q_{i3}\mathbf{c}_{3}$$
(3-33)

The transformation matrix **P** becomes **PQ** after the rotation of the crystal, where matrix **Q** is given by

$$\mathbf{Q} = \begin{bmatrix} r_1^2 \left(1 - \cos \xi \right) + \cos \xi & r_1 r_2 \left(1 - \cos \xi \right) + r_3 \sin \xi & r_1 r_3 \left(1 - \cos \xi \right) - r_2 \sin \xi \\ r_2 r_1 \left(1 - \cos \xi \right) - r_3 \sin \xi & r_2^2 \left(1 - \cos \xi \right) + \cos \xi & r_2 r_3 \left(1 - \cos \xi \right) + r_1 \sin \xi \\ r_3 r_1 \left(1 - \cos \xi \right) + r_2 \sin \xi & r_3 r_2 \left(1 - \cos \xi \right) - r_1 \sin \xi & r_3^2 \left(1 - \cos \xi \right) + \cos \xi \end{bmatrix}$$
(3-34)

This transformation matrix and the corresponding Euler angles have to be updated in order to account for the re-orientation of the grains during the plastic straining.

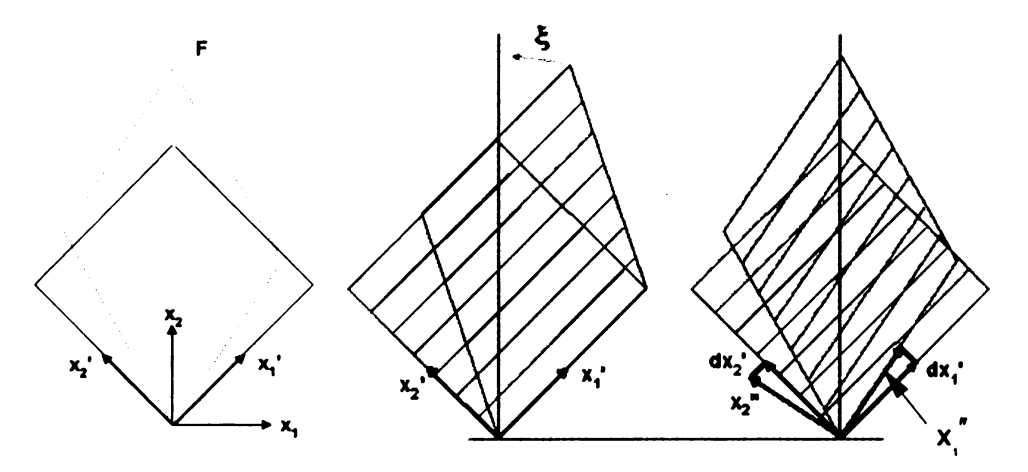


Figure 3-1. Slip systems rotation when a crystal with only one slip system is subjected to an extension

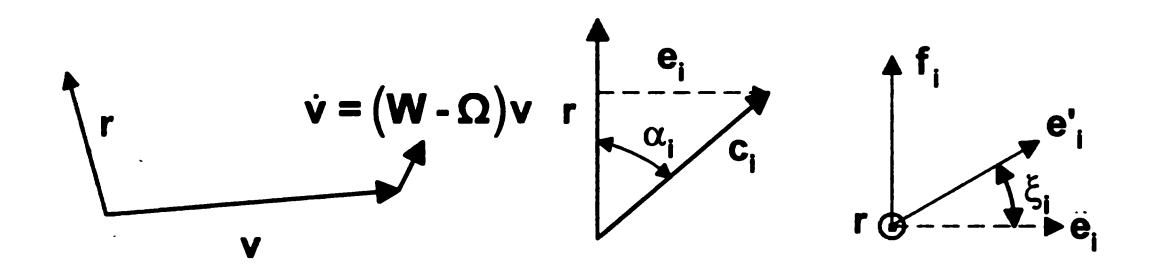


Figure 3-2. Rotation axis and angle corresponding to a spin \mathbf{W} - $\mathbf{\Omega}$.

3.6 Implementation into Finite Element Code

The polycrystal model was implemented into ABAQUS/Explicit FE code, assuming a full polycrystal at each integration point. The orientation and hardening of individual grains associated with each element is updated as deformation proceeds.

3.6.1 Quasi-static Analysis

ABAQUS/Explicit can be an effective tool for solving a wide variety of nonlinear solid and structural mechanics problems. Particularly, it is very efficient in solving certain class of nonlinear problems that are essentially static. Tube hydroforming simulation is one of these highly nonlinear quasi-static problems. It involves very large membrane deformation, buckling and complex frictional contact condition. One might encounter

severe convergence problems if ABAQUS/Standard (implicit solver) is used instead for the simulation.

Applying the explicit dynamics procedure to quasi-static problems requires some special considerations. Since a static solution is, by definition, a long-time solution, it is often computationally impractical to analyze the simulation in its natural time scale, which could require an excessive number of small time increments. To obtain an economical solution, the event must be accelerated in some way. The problem is that as the event is accelerated, the state of static equilibrium evolves into a state of dynamic equilibrium in which inertial forces become more dominant.

The computer time involved in running a simulation using explicit time integration with a given mesh is directly proportional to the time period of the event. This is because numerical stability considerations restrict the time increment to

$$\Delta t \le \min\left(L^{el}\sqrt{\frac{\rho}{\lambda + 2\mu}}\right) \tag{3-35}$$

where the minimum is taken over all elements in the mesh, L'' is a characteristic length associated with an element, ρ is the density of the material in the element, and λ and μ are the effective Lame's constants for the material in the element. Since this condition effectively means that the time increment can be no larger than the time required to propagate a stress wave across an element, the computer time involved in running a quasi-static analysis can be very large. The cost of the simulation is directly proportional to the number of time increment required, $n = T/\Delta t$, if Δt remains constant, where T is time period of the event being simulated. (Δt will not remain constant in general, since

element distortion will change L^{el} and nonlinear material response will change the effective Lame's constants and density. But the assumption is acceptable for the purpose of this discussion, thus,

$$n = T / \max \left(L^{el} \sqrt{\frac{\rho}{\lambda + 2\mu}} \right) \tag{3-36}$$

In polycrystal model approach, using the Newton-Raphson iterative method to compute the Cauchy stress for each integration point through the user material subroutine (VUMAT) is very costly. An inexpensive alternative therefore is to obtain the strain path for any critical location (integration point) from a FE simulation with a phenomenological constitutive model (e.g., von Mises, Yld96, etc.) and use this information as input for the polycrystal model to predict the evolved texture.

3.6.2 Initial Crystallographic Texture Input

In this approach, the polycrystal model discussed above was directly implemented into the ABAQUS/Explicit code via the user material subroutine (VUMAT) option. Each integration point in the shell element was viewed as an aggregate consisting of hundreds of single crystals. The strain increment of each step for each integration point was imposed to each single crystal as required by the Taylor-type model.

The material used in this study was 6061-T4 extruded aluminum tubes, which were obtained by heat treatment (heated to 520 0 C, maintained 1 hour, quenched to room temperature in one minute) of the original 6061-T6 tubes purchased from an aluminum vendor. Figure 3-3 shows the (111) pole figure for this material using 1005 grain orientations. This represents in the statistical sense the texture shown in Figure 3-4 (OIM

pole figures and CODF) without losing the characteristic grain distribution. In the finite element simulation, the initial crystallographic texture characterized by OIM is incrementally updated using the spin tensor. Of course, the more grain orientations are introduced into the calculation, the more accurate the crystallographic texture will be represented. However, considering the expensive CPU time, if all the grain orientations (about 90,000) were to be used to represent the initial crystallographic texture inside the VUMAT, an extraordinary CPU time will be required to simulate the tube hydroforming process. Based on the current computational condition we have used 10, 20 and 40 grain orientations to represent the initial texture of the tube.

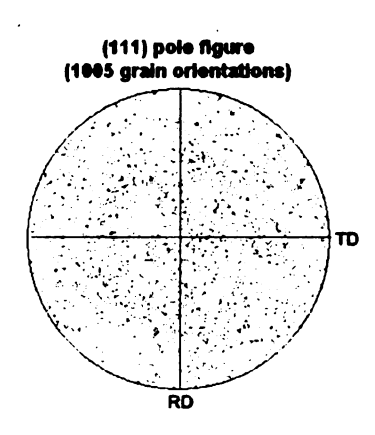


Figure 3-3. Pole Figure (111) with 1005 grain orientations, representing the undeformed tube

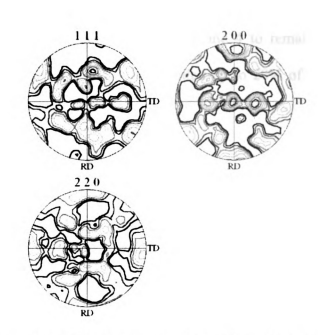


Figure 3-4a. OIM pole representing the undeformed 6061-T4 aluminum tube

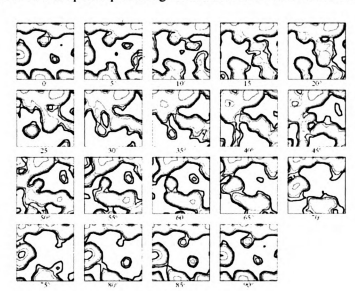


Figure 3-4b. CODF for the undeformed 6061-T4 aluminum tube

3.7 Verification of the Polycrystal Model

3.7.1 Uniaxial Tension Simulation

Uniaxial tension simulations were carried out in order to verify the capability of the polycrystal model. Two finite element models were used for this purpose. The first model considers the uniaxial tension of a single S4R element (see Figure 3-5). MPC (multi-

point-constraints) was used to constrain nodes 3 and 4 to remain on the straight line parallel to the X-axis. Nodes 2 and 3 were pulled up to 20% of the unit length of the element using the displacement control.

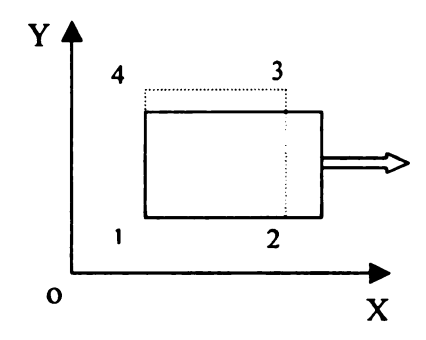


Figure 3-5 Uniaxial tension simulation (one single element)

For comparison, 1, 10 and 20 grain orientations were used in the simulations to represent the initial texture of the material in the VUMAT. The total calculation time for this case was 1ms. The strain/stress curves from ABAQUS and the experiment are shown in Figure 3-6. It can be seen that the experimental stresses are underestimated when only one grain is used, as this does not properly represent the true property (anisotropy) of the material. When 10 grain orientations were used, although the experimental stresses were underestimated, a significant improvement was observed. However, when 20 grain orientations were used although the stress levels increased but a large oscillation in the stresses up to 3% strain was also observed. It is believed that this stress oscillation was due to dynamic effects (loading and unloading), since in this strain range the kinetic energy is still rising, as shown in Figure 3-10. Also the nature of the rigid plastic formulation used in the polycrystal model, which calculates the total stresses rather than incremental stresses for each incremental deformation, contributes to this stress oscillation.

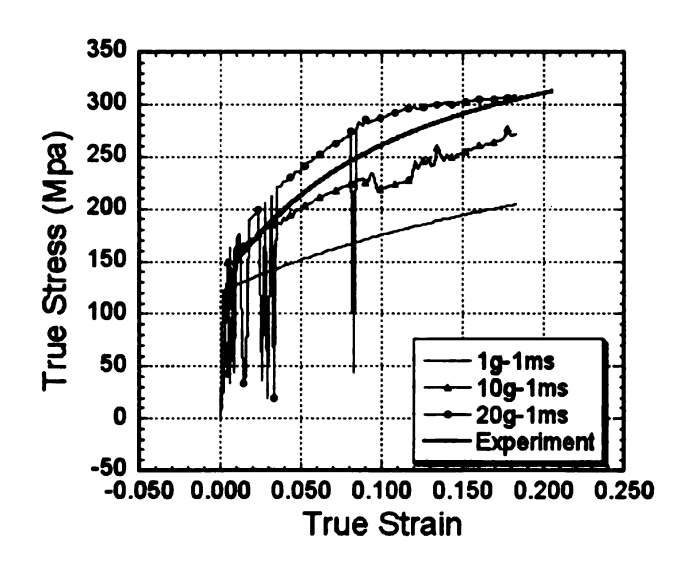


Figure 3-6 Comparison of experimental uniaxial tension strain/stress curve with those obtained by ABAQUS using polycrystal model (VUMAT)

To alleviate the extraordinary CPU cost of directly simulating with the polycrystal model, the strain path for the uniaxial tension was extracted from the explicit code and used as input to run the polycrystal model with large number of grains outside of the ABAQUS. Figure 3-7 shows the strain/stress curves obtained from this approach for different number of grain orientations. Again, some improvements in stress prediction up to 10% strain could be observed by using more grain orientations (up to 1005), but beyond this strain level the polycrystal model consistently underestimates the experimental stresses. The reason for this could be that only 100 of the approximately 1000,000 increments from the explicit code were used to generate these curves.

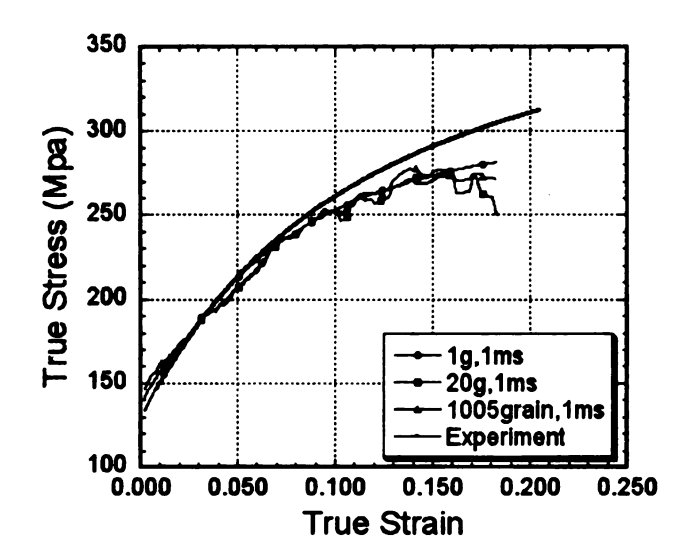


Figure 3-7 Strain/stress curves predicted for uniaxial tension using polycrystal model outside of ABAQUS (100 of 1000,000 increments from VUMAT were used)

Another uniaxial tension simulation was based on the exact (dog bone) shape of the specimen used in the experiment. Due to symmetry, only a quarter model was used for the simulation (see Figure 3-8). Barlat's Yld96 yield function (Chapter 4) was implemented into the ABAQUS implicit code for this purpose. Similar to previous method, the strain path was obtained from this implicit simulation and then was used as input in the polycrystal model to predict the stress-strain curve. Figure 3-9 shows the strain/stress curves from this approach for different number of grains. It could be seen that a significant improvement has resulted regardless of the number of grains used. The reason for this is that the exact strain path (i.e., 580 increments) as used in the implicit code was used to simulate the uniaxial tension test with the polycrystal model.

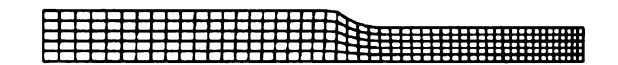


Figure 3-8 Finite element model used for simulating the uniaxial tension test with ABAQUS/implicit code

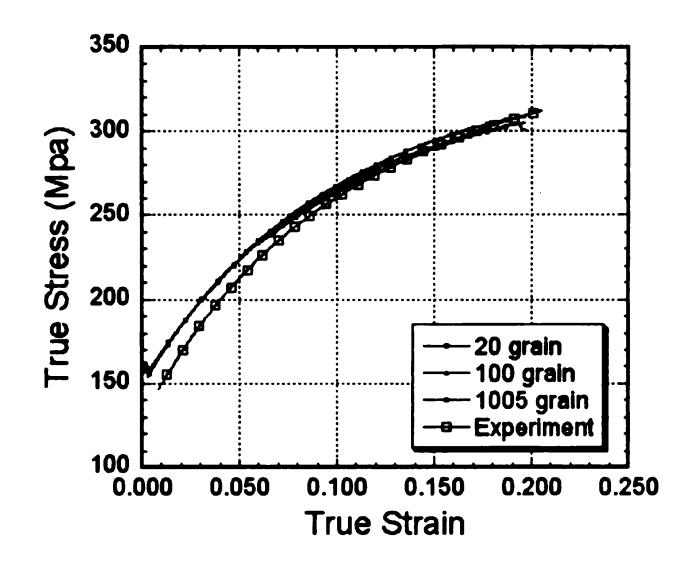


Figure 3-9 Predicted strain/stress curves for uniaxial tension using polycrystal model outside of ABAQUS (all 508 increments from ABAQUS/implicit code were used)

3.7.2 Bulge Test

Geometry, Material Properties and Loading in the FEA

The dimensions and material properties of the sample tube are shown in Table 3-1 below.

Length (inch)	OD (inch)	Thickness (inch)	E (Gpa)	V	σ _ν (Mpa)
8.0	2.0	0.05	71	0.3	129.0

Table 3-1 Dimensions and mechanical properties of the tube

The tube was modeled using SAX element type, which is a 2-node, axisymmetric shell element. Three (3) integration points through the thickness were used in each shell element. Due to the axial symmetry of the aluminum tube, only the meridian of the tube was modeled. The plunger mechanism was not modeled but instead the axial feed was directly applied to the tube's ends by using a displacement boundary condition.

The contact between the tube and the die was modeled with the *CONTACT PAIR option. The outside surface of the tube was defined by means of the *SURFACE DEFINITION option. The die was modeled as analytical rigid surface with the *RIGID

SURFACE option. An analytical rigid surface yields a more accurate representative of the doubly curved die and results in computational savings. The rigid die surfaces are offset from the tube by half the thickness of the tube because the contact algorithm in ABAQUS/Explicit takes the shell thickness into account. The mechanical interaction between the contact surfaces was assumed to be frictional contact. The coefficient of friction between tube and die was taken to be 0.1.

For finite-strain shell elements, such as SAX1, the transverse shear stiffness is computed by matching the shear response for the shell to that of a three-dimensional solid for the case of bending about one axis. When VUMAT (user subroutine for ABAQUS/Explicit) is used to define a shell element's material response, the *TRANSVERSE SHEAR STIFFNESS option must be used. The definition of the transverse shear stiffness of the section of a shear flexible shell element is defined in ABAQUS (see Theory Manual).

A linearly increasing hydrostatic pressure was applied on the inside of the tube. The final pressure was 14 Mpa (2030psi) as measured from the experiment. Simultaneously, the ends of the tube were subjected to an axial displacement of 3mm from each side, which was measured from the experiment and provided as input for the simulation. A viscous pressure load was applied to the surface of the shell during the simulation to damp out transient wave effects so that quasi-state equilibrium could be reached quickly. The coefficient of viscous pressure was chosen to be approximately 1% of the value of ρc_d , where ρ is the material density of the tube and c_d is the dilatational wave speed.

Finite element sensitivity analysis

As the material (aluminum alloy) is rate-independent, time was the only parameter used in order to drive the loading process. However, in this case, the polycrystal model (rate-independent itself) was implemented into the explicit code to represent material response, and therefore the speed of the analysis, namely the loading rate, became very crucial in the simulation. The loading rate can be increased so that the same physical event occurs in less time (compared to the natural time in physical process), as long as the solution remains nearly the same as the true solution and dynamic effects remain insignificant (see ABAQUS Manual).

Smooth amplitude curves were required for accurate and efficient quasi-state analysis, even though the exact loading curve extracted from the experimental loading profile was applied. The number of grains was also an important parameter in the FE simulations. The prediction of the texture evolution usually required a large number of orientations to be used in order to track and predict texture in the pole figures.

Sensitivity with respect to total simulation time

First, the influence of the total simulation time on the material response was investigated. The simulations were carried out using 10 SAX elements and only 1 grain was considered for each integration point. It should be noted that one grain does not represent the anisotropy of the extruded aluminum tube, but provides for a CPU-efficient analysis. The total simulation times of 0.1ms, 0.5ms, 1.0ms, 5.0ms, 10.0ms and 50.0ms were tested. Table 3-2 shows the maximum hoop strains predicted by ABAQUS/Explicit code. It was noted that as the total simulation time was increased, approaching the actual

deformation time, the rigid plastic model's prediction of hoop strain also increased. However, the predicted hoop strain of 14.3% for a total simulation time of 10ms was far below the experimental maximum hoop strain of 20%. On the other hand, the predicted hoop strain of 39% for the total simulation time of 50ms was much higher than the experimental maximum hoop strain of 20%. To find out the optimal total simulation time at which the maximum hoop strain no longer changes, we had to try higher simulation times. However, due to the extremely large CPU time (approaching several weeks) needed to simulate the case of 50ms, longer total simulation times were not attempted.

Total Time (ms)	0.1	0.5	1.0	5.0	10.0	50.0
Maximum Hoop Strain	6.88%	9.22%	9.37%	11.3%	14.3%	39%

Table 3-2 Sensitivity with respect to total simulation time (1 grain orientation, 10 elements)

Sensitivity with respect to number of grain orientations

Next, the sensitivity of the numerical solution to the total number of grain orientations used in the simulation of tube bulging was investigated. For this purpose a total simulation time of 1.0ms and 10 SAX elements were used.

Number of Grain Orentations	1	10	20	40
Maximum Hoop Strain	9.37%	10.0%	9.26%	9.24%

Table 3-3 Sensitivity with respect to number of grain orientatins (1.0ms, 10 elements)

As could be seen Table 3-3, the variation in predicted maximum hoop strain, as a function of the number of grain orientations used in the finite element simulation, is negligible.

However, when the total simulation time was increased from 1.0ms to 10.0ms, the predicted maximum hoop strain increased significantly, as a function of the number of grain orientations used in the finite element simulation, as shown in Table 3-4.

Grain Orientation Number		10	20	
Maximum Hoop Strain	14.3%	20.4%	23.0%	

Table 3-4 Sensitivity with respect to number of grain orientations (10ms, 10 elements)

The explanation for this increase in predicted hoop strain can be found in equations 3-35 and 3-36. That is, by increasing the total simulation time, the accuracy of the model improves, since simulation time approaches the actual deformation time. Also, the number of simulation increments proportionally increases with increases in total simulation time. Since the polycrystal model is based on the rigid plasticity theory, which treats total strain as plastic strain, the predicted final strain increases as the simulation increments double. Finally, the results from Table 3-4 indicate that the simulation case with 10 elements, 10 grains and 10ms predicts a maximum hoop strain of 20% which is similar to the experimental strain.

Sensitivity with respect to number of elements

Another set of numerical experiments was performed to study the sensitivity of predicted maximum hoop strain to the number of elements used in the finite element simulation. Table 3-5 shows that by increasing the number of elements two and four folds, the maximum hoop strain increases slightly. Unfortunately, by increasing the number of elements by four folds the CPU time also increased by four folds. Therefore, it was not

feasible to try larger number of elements, in order to find the optimum number of elements for tube bulging simulation.

Element Number	10	20	40
Maximum Hoop Strain	9.37%	10.2%	12.7%

Table 3-5 Sensitivity with the number of elements (1 grain orientation, 1ms)

Figure 3-10 shows a typical plot of the history of the kinetic and internal energies versus the total simulation time (e.g., 10.0ms). It can be seen that the internal energy increases smoothly to the final value, while the kinetic energy remains as much as 3-4 orders of magnitude smaller than that, indicating that the dynamics effects are eventually dampened and that the simulation is close to being quasi-static.

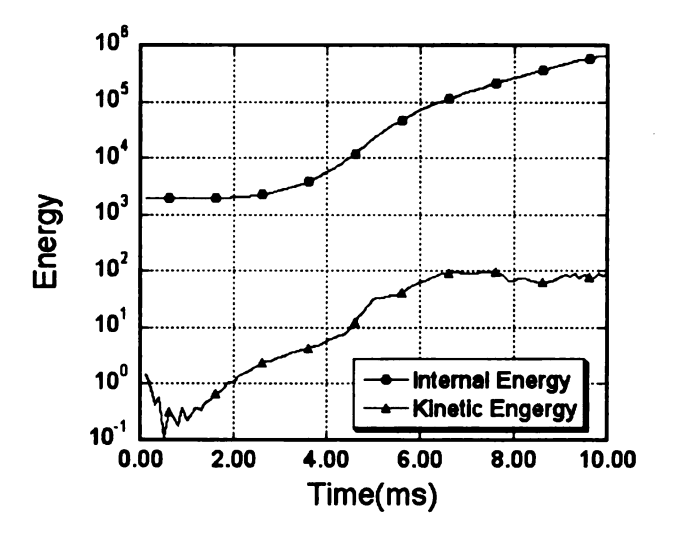


Figure 3-10 Kinetic and internal energy histories for 10ms, 10 grain orientations, 10 element simulation

Figure 3-11 shows the undeformed and deformed shapes of the bulged tube for the case of 10ms, 10 grain orientations and 10 elements. Figures 3-12a-d show the corresponding

strain and stress distributions. The axisymmetric elements can be swept circumferentially to produce (visually) three-dimensional tube.

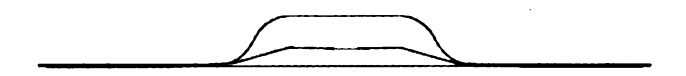
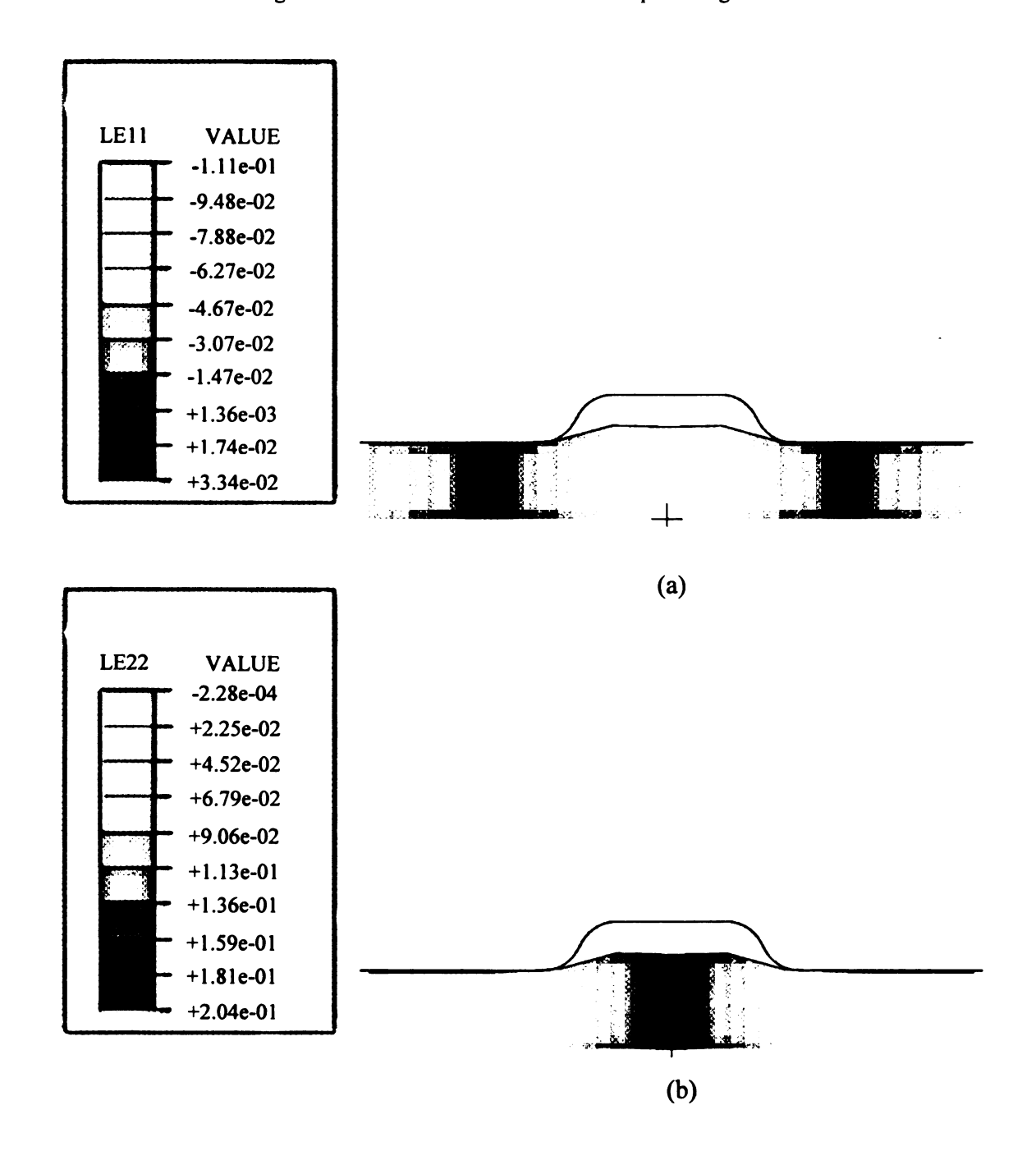


Figure 3-11 Undeformed and deformed shape of bulged tube



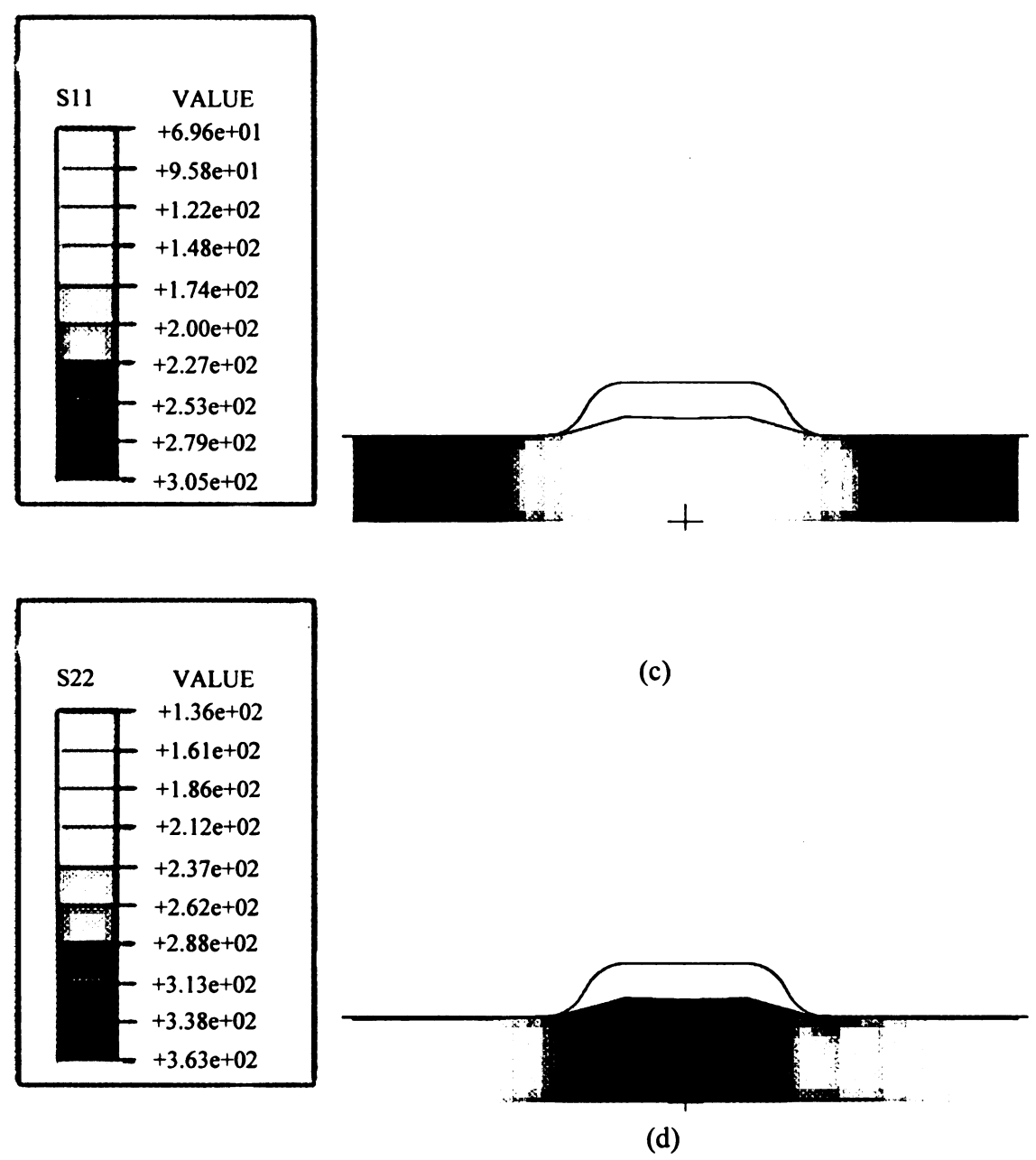


Figure 3-12 strain and stress distribution of the bulged tube (a) hoop strain, (b) axial strain, (c) hoop stress, (d) axial stress

3.8 Observations on texture evolution

Texture information for more than 90,000 grain orientations was measured from the undeformed tube sample by OIM at Alcoa (see Figure 3-3). From that set 1005 grain

orientation were extracted to represent the initial texture orientation of the tube, and to use as input data to carry out the numerical simulation of the hydraulic bulging with polycrystal model. The evolved texture of the hydraulically bulged extruded aluminum tube was also measured by OIM at Alcoa. For the deformed tube sample, texture information for more than 58,000 grain orientations was collected by OIM, from which 1011 grain orientations were again extracted to represent the deformed texture of the tube (see Figure 3-16).

For comparison with OIM, strain paths (Figure 3-13a-b) for tube bulging were obtained from ABAQUS explicit and implicit simulations (Yld96) and then used in the polycrystal model (outside of ABAQUS) to predict the texture evolution.

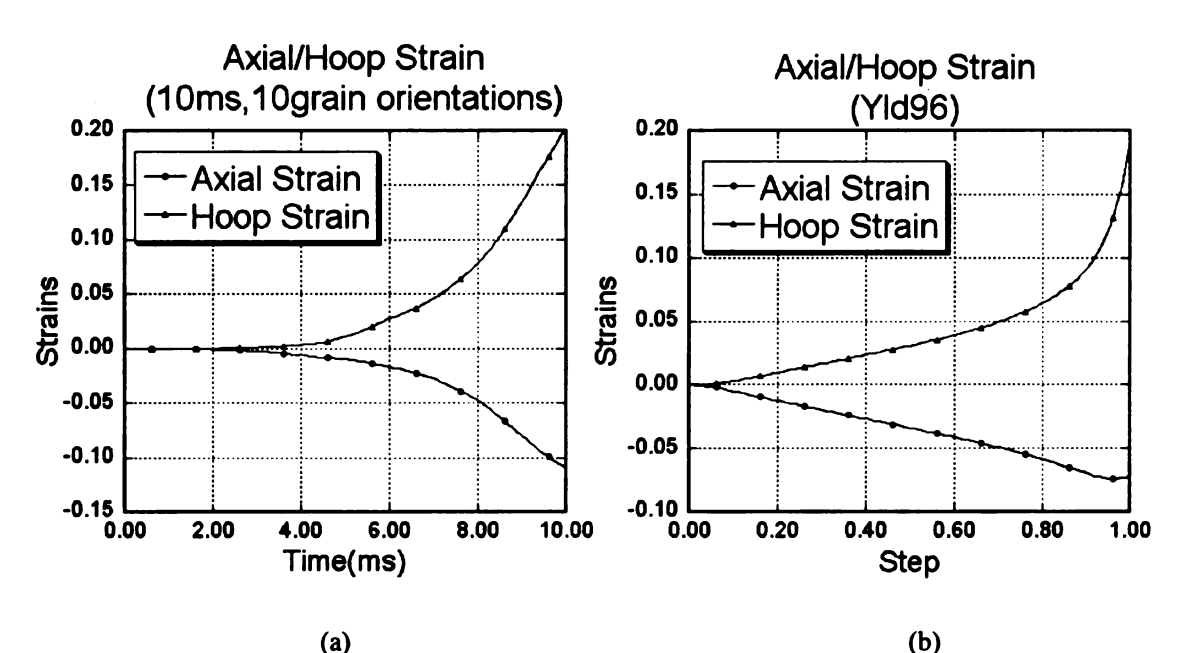


Figure 3-13 (a) strain path from explicit simulation (10ms, 10 grain orientations)

(b) strain path from implicit simulation (Yld96)

Figures 3-14 and 3-15 show the predicted (111) pole figure for the aluminum tube after the bugle test using the strain paths from the explicit simulation (10ms, 10 grain orientations, 10 elements) and the implicit simulation with Barlat's Yld96; respectively. The details of the implicit simulation of bulge test using Barlat's Yld96 can be found in Chapter 4. A comparison of the two pole figure plots indicate that the two predicted textures are comparable to each other. That is, predicted location and the intensity of grains with (111) orientation are similar in both models. A comparison of predicted textures with that obtained from OIM (Figure 3-16) indicates that the actual intensity is somewhat underestimated by the models. Two possible explanations for this observed difference in texture could be offered. First, it is shown before that the Taylor model's texture prediction is always different from the actual texture, since grain boundary interactions are ignored, which results in unrealistic rotation of the grains. Second, this could have been caused by the fact that the location on the deformed tube where texture was measured was different from the location where it was measured on the undeformed tube. Although it is generally assumed that the texture information represents a statistical distribution of grains that is independent of the location where it is measured on the part, the initial texture may have in fact been very different in the two locations where they were measured before and after the deformation.

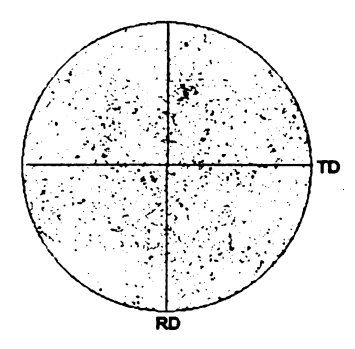


Figure 3-14 (111) pole figure after bulging (strain path obtained from ABAQUS/explicit)

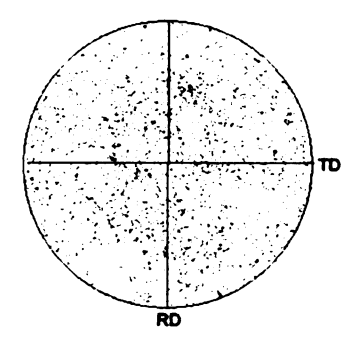


Figure 3-15 (111) pole figure after bulging (strain path obtained from ABAQUS/implicit)

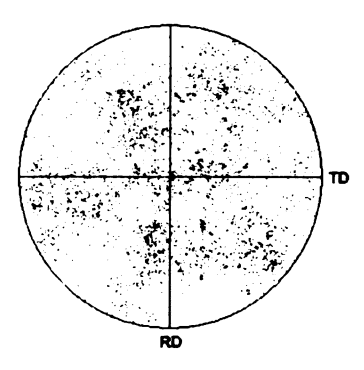


Figure 3-16 (111) pole figure after bulging obtained from OIM

The complete pole figure and CODF measured from OIM for the bulged tube can be seen in Figures 3-17a-b.



Figure 3-17a OIM pole representing the bulged 6061-T4 aluminum tube

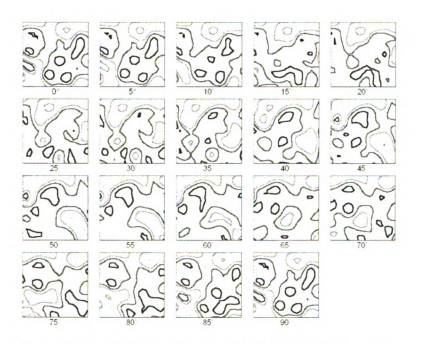


Figure 3-17b CODF representing the bulged 6061-T4 aluminum tube

CHAPTER 4

PHENOMENOLOGICAL MODELING

As shown in Chapter 3, the main advantage in using polycrystalline constitutive model is that it can predict anisotropic strain hardening effects due to the crystallographic texture evolution during the hydroforming process. However, in practice, numerical simulation with polycrystal models is difficult, time-consuming and therefore not feasible for iterative design process. So, developing accurate phenomenological constitutive models that could be implemented into commercial FE codes would be desirable.

4.1 Phenomenological Yield Function

In the phenomenological approach, the plastic behavior of the metal is well described by an analytical yield function. The yield surface defines the critical stress levels for plastic yielding, and it often serves as a plastic potential for the plastic strain increment according to the associated flow rule. For finite element analysis of forming processes, the yield surface and the stress-strain curve (strain hardening) are important material property data.

Several anisotropic yield functions associated with isotropic work hardening have been proposed. Hill's 1948 yield function is certainly the most popular for describing the plastic behavior of anisotropic materials such as rolled steel sheets [Hill 1948]. Hosford (1972) introduced an isotropic yield function based on the results of polycrystal calculations. Hill (1990) proposed a nonquadratic yield function that can be used to improve the yielding description for aluminum alloys. However, Barlat et al. (1997) proposed the most accurate yield function for aluminum sheet alloys. This so-called Yld96 yield function simultaneously accounts for the anisotropy of the uniaxial yield

stresses as well as r-values (i.e., width to thickness strain ratio). In order to describe the anisotropic behavior of extruded aluminum tubes one must calculate the anisotropic coefficients of the Yld96 yield function using known yield stresses and r-values.

4.2 Yld96 yield function

The yield function proposed by Barlat et al. (1997) is given by

$$\phi = \alpha_3 |S_1 - S_2|^m + \alpha_1 |S_2 - S_3|^m + \alpha_2 |S_3 - S_1|^m = 2\bar{\sigma}^m$$
(4-1)

where $\overline{\sigma}$ is the effective stress and m is a material parameter which is typically set to 8 for FCC and 6 for BCC materials. Parameters $S_{i=1,2,3}$ correspond to the principal values of a symmetric matrix $S_{\alpha\beta}$ defined with respect to the components of the Cauchy stress as

$$S = \begin{bmatrix} \frac{C_{3}(\sigma_{xx} - \sigma_{yy}) - C_{2}(\sigma_{zz} - \sigma_{xx})}{3} & C_{6}\sigma_{xy} & C_{5}\sigma_{zx} \\ C_{6}\sigma_{xy} & \frac{C_{1}(\sigma_{yy} - \sigma_{zz}) - C_{3}(\sigma_{xx} - \sigma_{yy})}{3} & C_{4}\sigma_{zy} \\ C_{5}\sigma_{zx} & C_{4}\sigma_{zy} & \frac{C_{2}(\sigma_{zz} - \sigma_{xx}) - C_{1}(\sigma_{yy} - \sigma_{zz})}{3} \end{bmatrix}$$
(4-2)

In the yield function, $\alpha_{k=1-3}$ are defined as

$$\alpha_{k} = \alpha_{x} p_{1k}^{2} + \alpha_{y} p_{2k}^{2} + \alpha_{z} p_{3k}^{2}$$
 (4-3)

where p_{ik} represents the components of the transformation matrix **p** between the orthogonal anisotropy axes of the material and the principal axes of S. Here, α_x , α_y are constant coefficients. For plane stress condition in which $\sigma_z = 0$ and the z-direction is the third principal direction,

$$\alpha_z = \alpha_{z0} \cos^2 2\beta + \alpha_{z1} \sin^2 2\beta \tag{4-4}$$

where β is the angle between the major principal direction of the stress tensor S and the rolling direction of the sheet or the extrusion direction of the tube. Also S can be simplified to

$$\left[S_{\alpha\beta} \right] = \begin{bmatrix} S_{xx} & S_{xy} & 0 \\ S_{xy} & S_{yy} & 0 \\ 0 & 0 & S_{zz} \end{bmatrix} = \begin{bmatrix} \frac{C_3(\sigma_{xx} - \sigma_{yy}) + C_2 \sigma_{xx}}{3} & C_6 \sigma_{xy} & 0 \\ C_6 \sigma_{xy} & \frac{C_1 \sigma_{yy} - C_3(\sigma_{xx} - \sigma_{yy})}{3} & 0 \\ 0 & 0 & -S_{xx} - S_{yy} \end{bmatrix}$$
(4-5)

The quantities C_1 , C_2 , C_3 , C_6 , α_x , α_y , α_{z0} and α_{z1} are the material coefficients which describe the anisotropic properties of the material.

Utilizing the normality rule, the associated plastic strain increment $\Delta \varepsilon_{\alpha\beta}^{p}$ is obtained from the yield function ϕ as

$$\Delta \varepsilon_{\alpha\beta}^{P} = \gamma \frac{\partial \phi}{\partial \sigma_{\alpha\beta}} \tag{4-6}$$

where γ is a scalar function. Using plastic incompressibility, we can express the r-value (width to thickness strain ratio) for any angle θ as [Barlat and Lian, 1989]

$$r_{\theta} = -\frac{\dot{\varepsilon}_{22}}{\dot{\varepsilon}_{11} + \dot{\varepsilon}_{22}} = \frac{\dot{\varepsilon}_{11}}{\dot{\varepsilon}_{11} + \dot{\varepsilon}_{22}} - 1 = \frac{\dot{\varepsilon}_{11}}{\dot{\varepsilon}_{xx} + \dot{\varepsilon}_{yy}} - 1 = \frac{\overline{\sigma}}{\left(\frac{\partial \overline{\sigma}}{\partial \sigma_{xx}} + \frac{\partial \overline{\sigma}}{\partial \sigma_{yy}}\right) \sigma_{\theta}} - 1$$
(4-7)

For plane stress ($\sigma_z = 0$), when the shear stress s_{xy} is equal to 0, the yield function is

$$\phi(s) = \alpha_x |s_y - s_z|^a + \alpha_y |s_z - s_x|^a + \alpha_{z0} |s_x - s_y|^a = 2\overline{\sigma}^a$$
 (4-8)

where

$$s_x = \frac{c_3 + c_2}{3} \sigma_x - \frac{c_3}{3} \sigma_y$$

$$s_{y} = -\frac{c_{3}}{3}\sigma_{x} + \frac{c_{3} + c_{1}}{3}\sigma_{y}$$

$$s_{z} = -\frac{c_{2}}{3}\sigma_{x} - \frac{c_{1}}{3}\sigma_{y}$$
(4-9-1-3)

Assume that ν is a constant, then

$$\phi\left(\frac{\alpha_x}{v^a}, \frac{\alpha_y}{v^a}, \frac{\alpha_{z0}}{v^a}, w_1, w_2, w_3, \sigma_x, \sigma_y, \sigma_z\right) = \phi(\alpha_x, \alpha_y, \alpha_{z0}, c_1, c_2, c_3, \sigma_x, \sigma_y, \sigma_z)$$
(4-10)

Therefore, among the C_1 , C_2 , C_3 , α_x , α_y and α_{z0} material coefficients that describe anisotropy, five of them are independent. To that end, it is suggested to set $\alpha_{z0}=1$. When the shear stress is not equal to zero, two other coefficients are also used to characterize anisotropy, C_6 and α_{z1} . In this case, the total number of anisotropy coefficients increases to seven. Therefore, it is necessary to use seven experimental tests or polycrystal model results to calculate these coefficients (see Appendix B for details).

4.3 Material characterization of 6061-T4 extruded aluminum tube

The 6061-T4 extruded aluminum tube samples were characterized using polycrystalline model (Chapter 3), while working at the Alcoa Technical Center during the summer of 2002. The strain-stress curve along the tube axis (Extrusion Direction, ED) was measured using a tensile test and the following Voce model was fitted to the experimental data (see Figure 4-1):

$$\overline{\sigma} = 338.56 - 206.29 \exp(-9.822\overline{\varepsilon})$$
 (4-11)

Using the method described in Appendix B, the stress-strain curves in other three directions (tangential direction (TD), radial direction (RD) and 45 degree between ED and TD) can be calculated. Figure 4-2 shows the stress vs. plastic work curves. The flow stresses $(\sigma_{ED}, \sigma_{RD}, \sigma_{TD}, \sigma_{45})$ used to calculate the anisotropy coefficients were

determined at the plastic work amount of 50 Mpa (mm/mm). Flow stresses, r-values and yield function coefficients for 6061-T4 are shown in Table 4-1. Figure 4-3 shows the corresponding Yld96 yield surface for the 6061-T4 extruded aluminum tube.

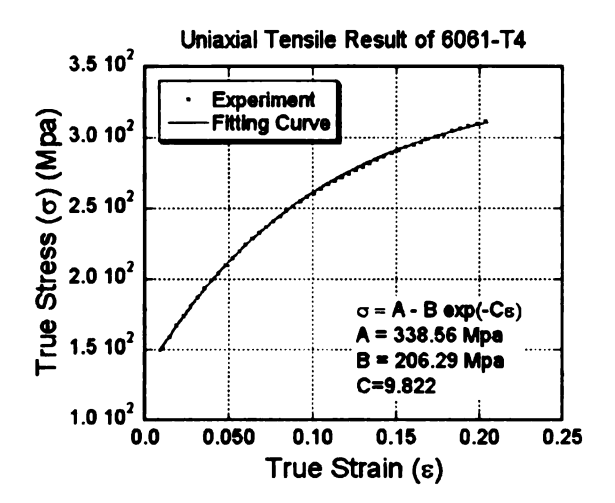


Figure 4-1 Experimental stress-strain curve measured in the extrusion direction (ED)

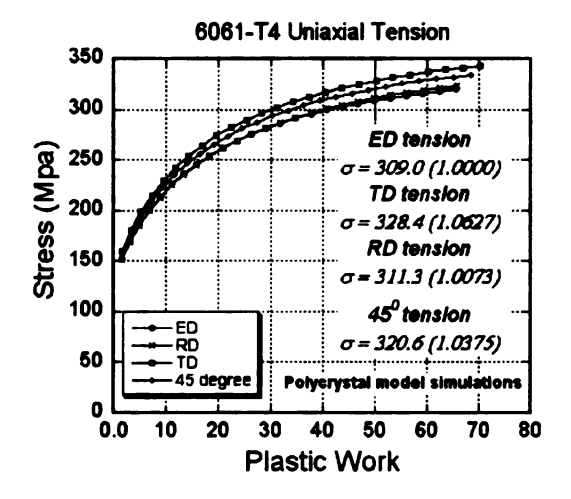


Figure 4-2 Stress vs. plastic work in various directions

Inpu	t Data	Coefficients of		
-		Yld96		
$\sigma_{ ext{ED}}$	1.0000	Cı	0.9068	
σ ₄₅	1.0375	C ₂	1.0313	
σ_{TD}	1.0627	C ₃	0.9474	
$\sigma_{ m RD}$	1.0073	C ₆	0.9265	
r _{ED}	0.6667	α_{x1}	1.265	
r ₄₅	0.8519	α_{yl}	1.15	
r _{TD}	0.9011	α_{z1}	1.3	
r _{RD}	0.6667	α_{z0}	1.0	

Table 4-1 Yld96 yield function coefficients for 6061-T4 extruded aluminum tube

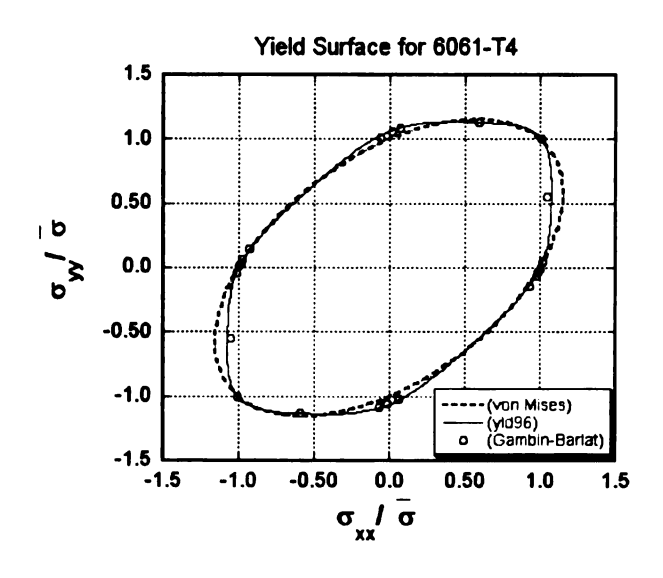


Figure 4-3 Yield surface (Yld96) for 6061-T4 (plane stress case and shear stress is equal to zero)

4.4 Implementation of Barlat's Yld96 into ABAQUS

Barlat's criterion (Yld96) was implemented into ABAQUS/Standard via the user material subroutine (UMAT) (see ABAQUS manual). With UMAT, users can implement their own material properties into ABAQUS by providing the expression of a stress increment with respect to a strain increment. Isotropic (von Mises) and anisotropic (Hill) material models were also used to compare with the Yld96 yield function.

4.4.1 Finite element simulation of the uniaxial tensile test

The specimen used in the uniaxial tensile test was cut directly from the extruded aluminum tube sample, as shown in Figure 4-4.



Figure 4-4 Specimen used for uniaxial tensile test

Due to the shape of the tube, this tensile specimen had a slight curvature. For simplicity and without the loss of accuracy, a flat dog bone shape model was used to simulate the tension test (see Figure 3-8). Due to symmetry, only a quarter model was set up and 250 S4R elements were used. The predicted stress-strain curve was then compared with the experimental result from Alcoa, as shown in Figure 4-5. The predicted stress-strain curve matched the experimental one very accurately.

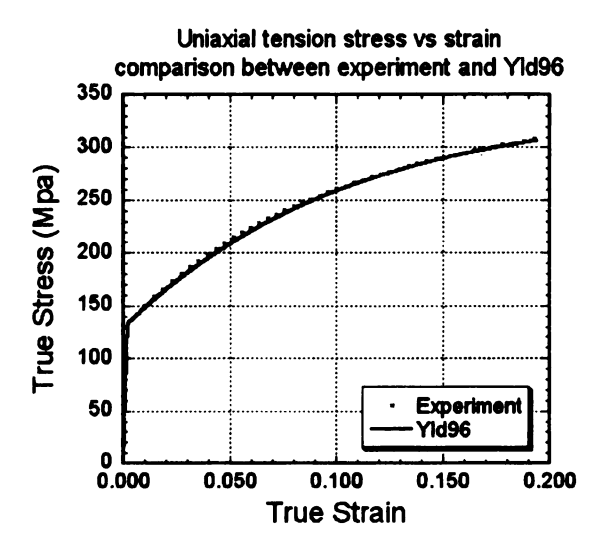


Figure 4-5 Stress/strain curve comparison between experiment and Yld96

The material properties and tube geometry shown in Table 3-1 are used for the bulge test and square die simulations. In this implicit analysis, two different dies; hydraulic bulge die and square section hydroforming die were used for the numerical simulation. Both dies were modeled as rigid body in the simulations. The *ORIENTATION option was used with the S4R elements to define a local orientation that is initially coincident with the global direction. The reason for using this option was to obtain the stress and strain output given in a co-rotational framework (i.e. material axes).

4.4.2 Hydraulic Bulge Test

Hydraulic bulge test was conducted to study the formability of the 6061-T4 extruded aluminum tube. A maximum internal pressure of 2030 psi (14 Mpa) was applied just before the tube burst in the experiment. Due to symmetry, again only a quarter model was used to simulate the tube bulging process.

Figure 4-6 shows a comparison of the measured and predicted hoop strain distributions. In the numerical simulations, von Mises and Hill's 1948 material models were also used

with ABAQUS's S4R shell element and compared with Yld96 result. As expected, the isotropic material model (von Mises) had the worst results and significantly underestimated the magnitude of the maximum hoop strain (16.7%). Hill's model, which accounts for transverse anisotropy of the tube showed some improvement, but still underestimated the measured hoop strain (18.1%). Although not perfect, the best strain predictions were obtained with Yld96 yield function (19.18%), accounting for planner anisotropy but assuming isotropic hardening. The maximum hoop strain measured experimentally was about 20.2%.

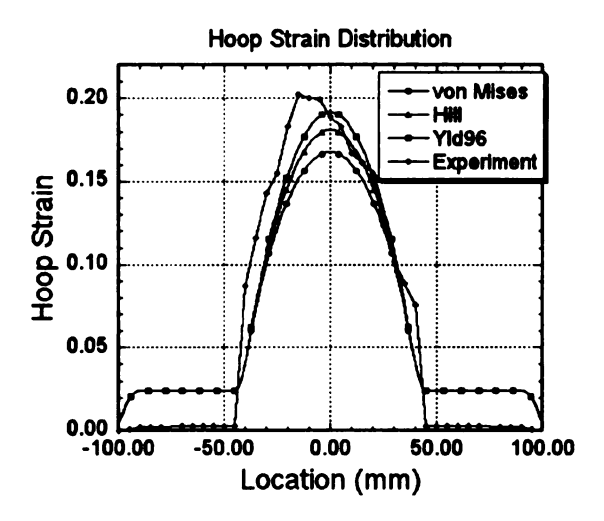
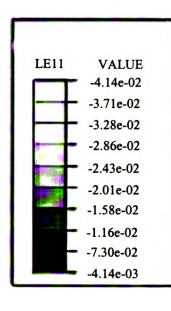


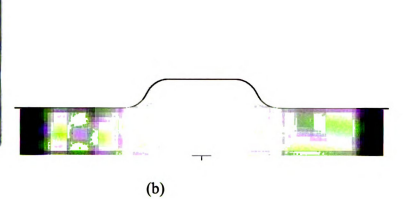
Figure 4-6 Hoop strain comparison for different yield functions

Figure 4-7-a-e show the bulged tube and the stress/strain contour in the ABAQUS simulation.

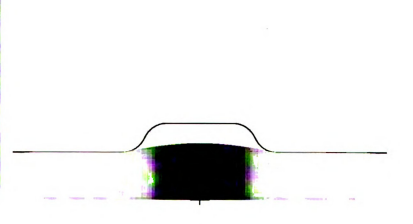


(a)





LE22 VALUE
+2.73e-03
+2.41e-02
+4.55e-02
+6.69e-02
+8.83e-02
+1.10e-01
+1.31e-01
+1.74e-01
+1.95e-01



(c)

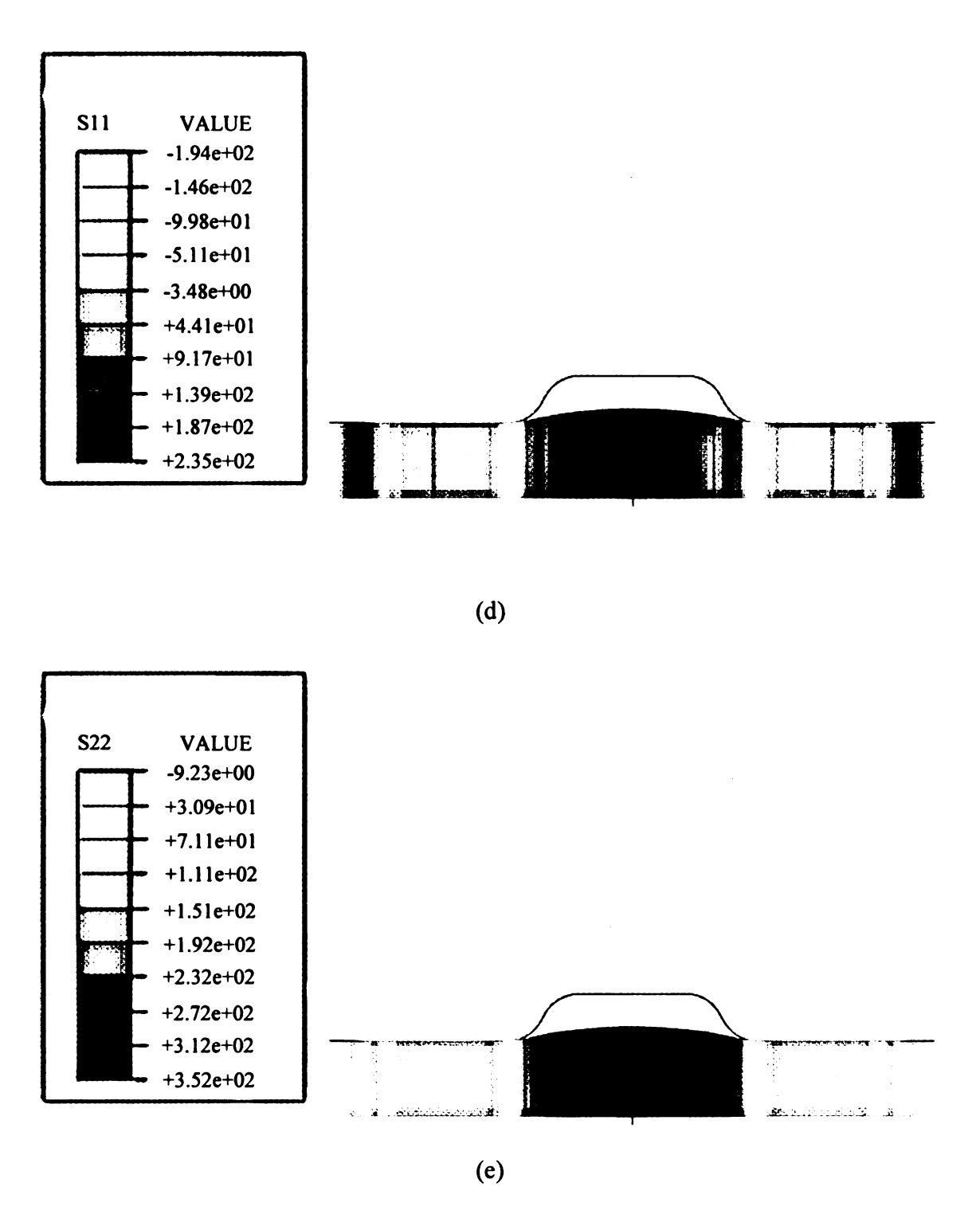


Figure 4-7 Deformation and strain/stress distribution for bulged tube
(a) deformation, (b) hoop strain, (c) axial strain, (d) hoop stress, (e) axial stress

4.4.3 Hydroforming a round tube into a square section

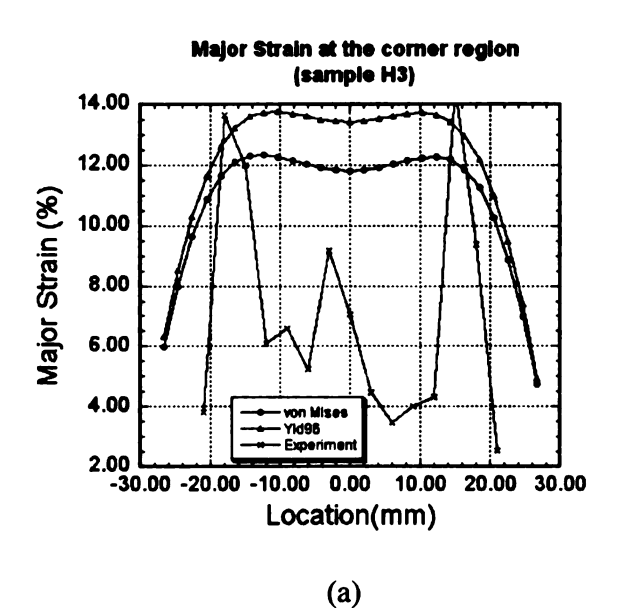
The simulation of hydroforming a round tube into a square section was also performed. Due to the complex geometry of the square die, the geometry of the square die was created with the UNIGRAPHICS software and then imported into HYPERMESH to create the mesh used in the ABAQUS. The major strains at the corner region of the hydroformed tube were measured for comparison, as shown in Figure 4-8.

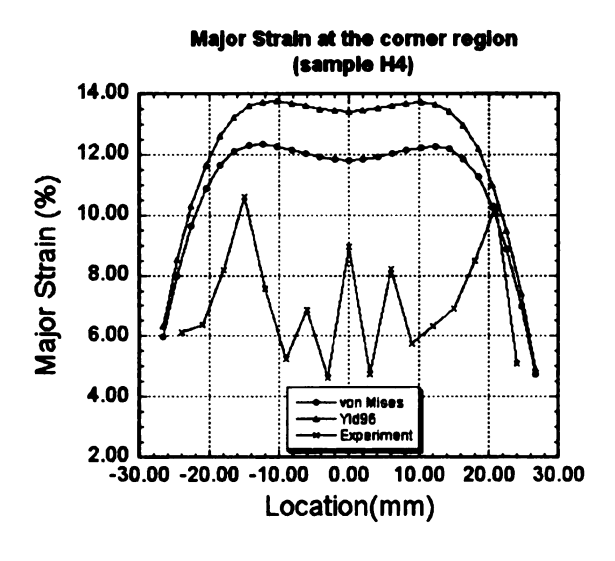


Figure 4-8 Corner region of the tube deformed in a square die (circle grids were used to measure the strains)

Figures 4-9a-c show the comparison between the numerically predicted major strains at the corner of the tube with the experimentally measured ones obtained from three different tube samples (designated as H3, H4 and H5). These figures show that strain predictions with Yld96 are higher than those predicted by the von Mises material model. The comparison with the experimental data is more difficult, since there is quite a bit of variation in the experimental data depending upon which sample is used. One consistent observation that could be made is that the magnitude of the measured strains in the middle of the tube are lower than those predicted by either model. However the distribution of the measured strains along the length of tube are similar to those predicted by both models. That is maximum at the ends and dropping in the middle of the tube.

Due to the difficulties that were experienced in the strain measurement process, the experimental results were not very consistent, which made verification of the numerical results more difficult. More accurate strain measurement will be done on the deformed tube in the near future.





(b)

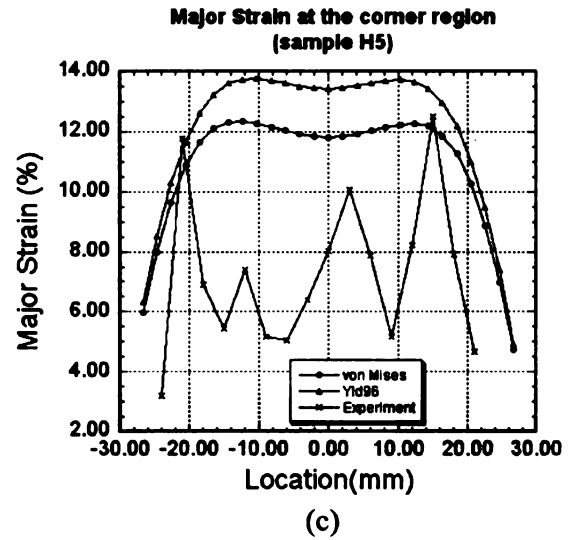
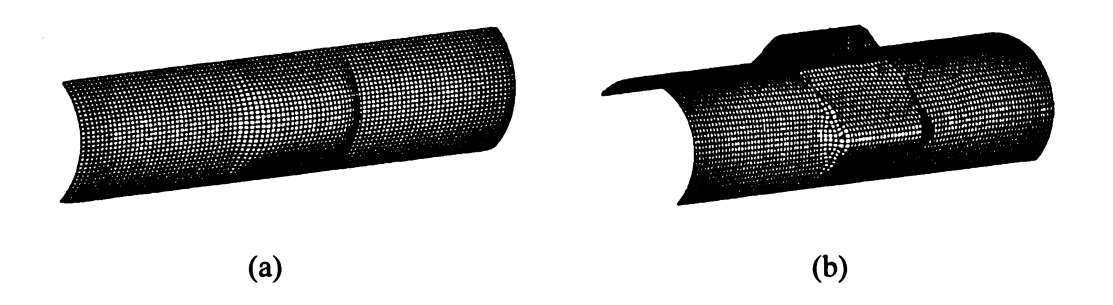


Figure 4-9a-c Major strain distribution comparison between numerical simulation and experiment

Figure 4-10a-d show the shape of deformed tube, mesh of the square die and the strain distributions of the deformed tube.



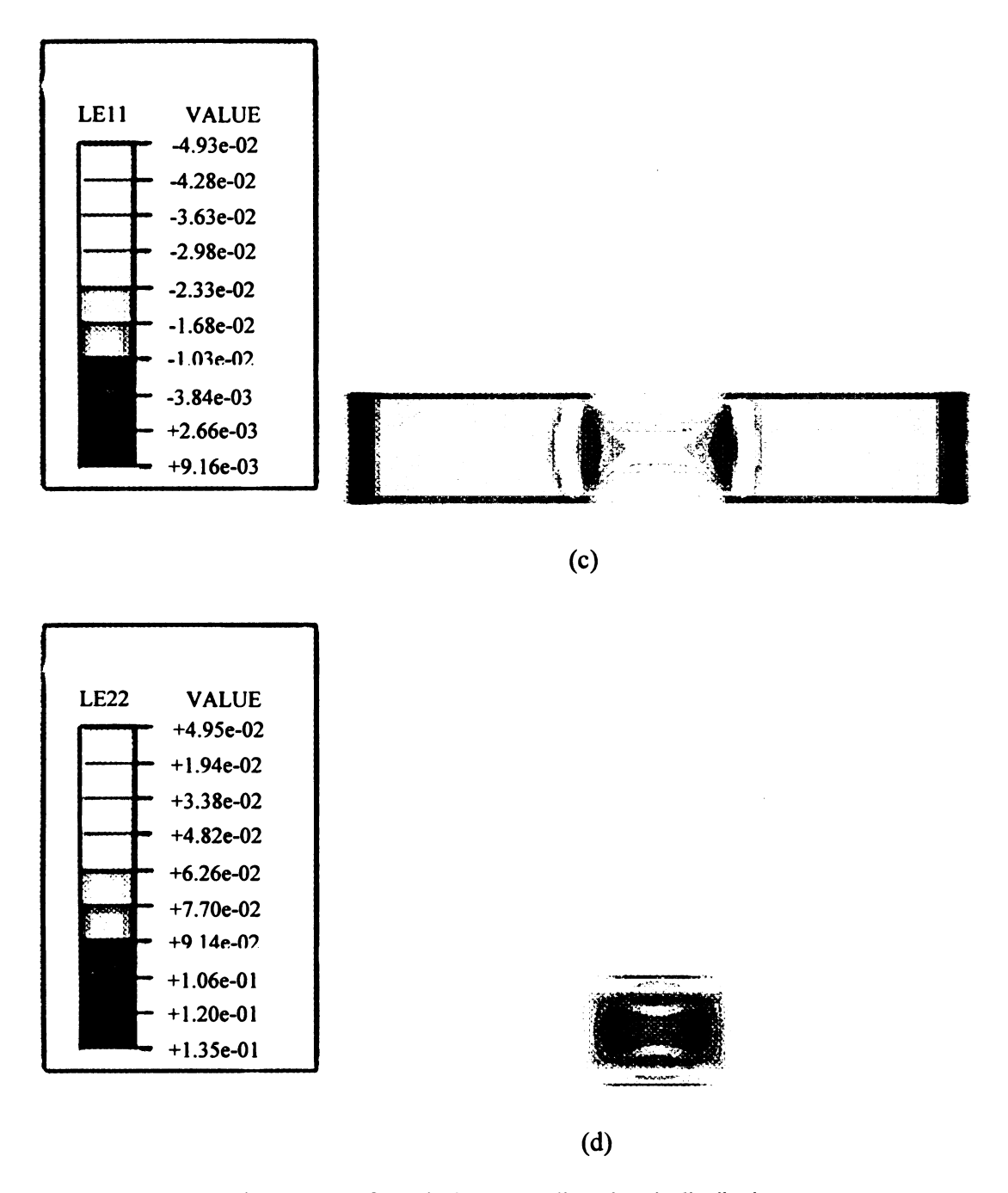


Figure 4-10 Deformed tube, square die and strain distributions (a) deformed tube, (b)square die,(c) axial strain (d) hoop strain

CHAPTER 5

PHENOMENOLOGICAL MODELING WITH

ANISOTROPIC STRAIN HARDENING

5.1 Strain Hardening in Single Crystal and Polycrystal

When metals are deformed plastically, the strength and hardness usually increase. This phenomenon is known as work hardening or strain hardening. It should be clarified that this kind of hardening is caused by cold working, not due to precipitation hardening. As mentioned in Chapter 2, slip in single crystal (or dislocation, more accurately), is the primary mechanism for the plastic deformation. In microscopic scale, the strain hardening also can be viewed as the required increase in the stress causing additional slip [Dieter 1976].

In a single crystal, strain hardening is caused by dislocations interacting with each other and with barriers that impede their motion through the crystal lattice. These interactions include dislocation pile up, cross slip etc. In polycrystals, this basic idea remains valid. However, due to the mutual interference of neighboring grains and the problem of compatible deformation among the adjacent grains, multiple slip occurs rather easily and, consequently, there occurs an appreciable work hardening right in the beginning of straining. In a manner similar to that in the single crystals, primary dislocations interact with secondary dislocations, giving rise to dislocation dipoles and loops, which result in local dislocation tangles and eventually a three-dimensional network of sub-boundaries. Generally, the size of these cells decrease with increasing strain. In high stacking fault energy (SFE) FCC metals like Al, the dislocation tangles rearrange into a well-defined

cell structure while in the low-SFE metals (brasses, bronzes, etc) where the cross-slip is rather difficult and dislocations are extended, the sharp sub-boundaries do not form even at very large strains.

Dislocation density and distribution will be changed (dislocation multiplication) due to these interactions when plastic strain increases. Both dislocation density and distribution of dislocations are very sensitive to the crystal structure, stacking fault energy, temperature, and the rate of deformation [Meyers 1984].

5.2 Isotropic and Anisotropic Strain Hardening

Most computations in metal forming are performed using the phenomenological theory of plasticity, which treats the metal as an isotropic material. It is a challenge to incorporate the initial anisotropy of metal into the theory of plasticity and to describe the subsequent anisotropic plastic deformation.

To account for the initial anisotropy, anisotropic yield criteria have been proposed by many researchers (see literature reviews for more detail). When these yield functions are implemented into the finite element analysis, the assumption of isotropic strain hardening is made because it is a reasonable approximation for proportional loading. However, in most metal forming processes, including tube hydroforming, non-proportional loading, unloading, and springback occurs which may require the use of the anisotropic hardening. The experimental investigations of anisotropic hardening of metals have been proposed. Phillips et al. (1972) presented the results of experiments in which thin-walled tubes of commercially pure aluminum in the annealed condition were loaded in combined tension and torsion in the plastic region at elevated temperatures. In this procedure, the yield surfaces were determined by probing in many different stress directions from the elastic

region into the plastic range. Kuwabara et al. (2000) and Kuroda et al. (1999) proposed a method for determining the subsequent yield surface in the vicinity of a current loading point by using an abrupt strain path change and also applied this idea to real experimental studies. Large strains can occur in many different loading paths. In the search for a unified description of strain hardening, it is important to study the strain hardening under different strain paths. Kopacz et al. (1999) presented the construction of equivalent stress-equivalent strain curves. The equivalent strain and equivalent stress are based on the average accumulated crystallographic shear and resolved shear stress respectively. Hu (2000) proposed several anisotropic hardening models for sheet metal based on the combination of the experimental stress-strain curves in different directions. Lopes et al. (2003) obtained the uniaxial and simple shear stress-strain curves for an aluminum alloy sheet sample in different specimen orientations with respect to the material symmetry axes. The stress-strain curves were predicted using the self-consistent polycrystal code [Lebensohn and Tome 1993].

The macroscopic parameters, such as normalized yield stress and r-values, are used to determine the constant coefficients in the anisotropic yield functions [Barlat et al. 1997] using the initial texture or experimental mechanical behavior data as input. However, sometimes these yield functions with constant coefficients are not sufficient to describe the anisotropic strain hardening after the onset of the initial yield. Lee (2002) proposed an optimization method to predict the change in the anisotropic coefficients of the yield functions [Barlat et al. 89; Barlat et al. 1991] using von Mises and Tresca yield potentials as the upper and lower bound surfaces, respectively. This method assumes that the

direction of the change in anisotropic coefficients varies predominantly in the direction of the yield surface gradient with respect to the anisotropic coefficients.

In this chapter, the linear directionality of the yield potential assumption is made and the change of anisotropic coefficients is simply determined by a single parameter. The evolution of the yield surface (Yld96) based on different loading path were calculated and compared with those based on the crystallographic approach developed in chapter 3.

5.3 Formulation of the Anisotropic Strain Hardening

5.3.1 Evolution of the Anisotropy Coefficients

In order to describe the anisotropic strain hardening after the initial yield, the coefficients of the yield function must evolve and can no longer remain constant. Therefore, the yield surface will be assumed to be a function of the anisotropy coefficients and deviatoric stresses:

$$\phi = \phi(c_i, \sigma_{ij}) \tag{5-1}$$

Furthermore, it will be assumed that the evolution of these anisotropy coefficients can be expressed as following:

$$c_i^{n+1} = c_i^n + \alpha \frac{\partial \phi}{\partial c_i} \tag{5-2}$$

where α is a scalar that should be calibrated based on experimental observations, c_i represents all the coefficients involved in the yield function, and $\frac{\partial \phi}{\partial c_i}$ represents the variation of the yield function as a function of the anisotropy coefficients. This former parameter could also be regarded as representing the dependency of the yield surface on

the strain path. In this research, for simplicity, it will be assumed that the value of the parameter α remains constant and independent of the strain path.

5.3.2 Evolution of the Yld96 Anisotropy Coefficients

For the plane stress case of the Yld96 yield function, the variation of the yield function with respect to the coefficients of anisotropy, $\frac{\partial \phi}{\partial c_i}$, can be determined based on the quantities derived in Yoon et al. (2000), as follows.

Given that the stress components are:

$$\begin{bmatrix} \tilde{\sigma}_{k} \end{bmatrix} = \begin{bmatrix} \sigma_{xx} \\ \sigma_{yy} \\ \sigma_{xy} \end{bmatrix}$$
 (5-3)

And the symmetric matrix S in Eq.4-5 is:

$$\left[\tilde{L}_{k}\right] = \begin{bmatrix} S_{xx} \\ S_{yy} \\ S_{xy} \end{bmatrix} = \begin{bmatrix} \frac{C_{3}(\sigma_{1} - \sigma_{2}) + C_{2}\sigma_{1}}{3} \\ \frac{C_{1}\sigma_{2} - C_{3}(\sigma_{1} - \sigma_{2})}{3} \\ C_{6}\sigma_{3} \end{bmatrix}$$
 (5-4)

The principal values of S can be found as follows:

$$[\tilde{\eta}_{k}] = \begin{bmatrix} S_{1} \\ S_{2} \\ S_{3} \\ \theta \end{bmatrix} = \begin{bmatrix} \frac{\tilde{L}_{1} + \tilde{L}_{2}}{2} + \sqrt{\left(\frac{\tilde{L}_{1} - \tilde{L}_{2}}{2}\right)^{2} + \tilde{L}_{3}^{2}} \\ \frac{\tilde{L}_{1} + \tilde{L}_{2}}{2} - \sqrt{\left(\frac{\tilde{L}_{1} - \tilde{L}_{2}}{2}\right)^{2} + \tilde{L}_{3}^{2}} \\ -(S_{1} + S_{2}) \\ \tan^{-1}\left(\frac{S_{1} - \tilde{L}_{1}}{\tilde{L}_{3}}\right)$$
 (5-5)

Then, $\bar{\sigma}(\sigma)$ in Eq.4-1 can b e written as

$$\overline{\sigma} = \left\{ \frac{1}{2} \phi \right\}^{\frac{1}{m}} = \left\{ \frac{1}{2} \left(\alpha_1 \left| S_2 - S_3 \right|^m + \alpha_2 \left| S_3 - S_1 \right|^m + \alpha_3 \left| S_1 - S_2 \right|^m \right) \right\}^{\frac{1}{m}}$$
 (5-6)

Given that the coefficients α_1 , α_2 and α_3 are defined as (see Eq. 4-3)

$$\begin{bmatrix} \tilde{v}_k \end{bmatrix} = \begin{bmatrix} \alpha_1 \\ \alpha_2 \\ \alpha_3 \end{bmatrix} = \begin{bmatrix} \alpha_x \cos^2 \theta + \alpha_y \sin^2 \theta \\ \alpha_x \sin \theta + \alpha_y \cos^2 \theta \\ \alpha_{z0} \cos^2 \theta + \alpha_{z1} \sin^2 \theta \end{bmatrix}$$
 (5-7)

And by defining the following new vectors:

$$\left[\tilde{q}_{k} \right] = \begin{bmatrix} \alpha_{x} \\ \alpha_{y} \\ \alpha_{z1} \end{bmatrix}, \ \alpha_{z0} = 1$$
 (5-8)

$$\begin{bmatrix} \tilde{c}_k \end{bmatrix} = \begin{bmatrix} c_1 \\ c_2 \\ c_3 \\ c_6 \end{bmatrix} \tag{5-9}$$

Then, the quantities $\frac{\partial \overline{\sigma}}{\partial \tilde{q}_k}$ and $\frac{\partial \overline{\sigma}}{\partial \tilde{c}_k}$ can be derived, using the chain rule, to be

$$\frac{\partial \overline{\sigma}}{\partial \tilde{q}_{k}} = \left\{ 2m\overline{\sigma}^{(m-1)} \right\}^{-1} \frac{\partial \phi}{\partial \tilde{q}_{k}} \\
= \left\{ 2m\overline{\sigma}^{(m-1)} \right\}^{-1} \sum_{a}^{3} \frac{\partial \phi}{\partial \tilde{v}_{a}} \frac{\partial \tilde{v}_{a}}{\partial \tilde{q}_{k}} \quad \text{(for k=1~3)}$$

$$\frac{\partial \overline{\sigma}}{\partial \tilde{c}_{k}} = \left\{ 2m\overline{\sigma}^{(m-1)} \right\}^{-1} \frac{\partial \phi}{\partial \tilde{c}_{k}}$$

$$= \left\{ 2m\overline{\sigma}^{(m-1)} \right\}^{-1} \sum_{a}^{4} \sum_{b}^{3} \frac{\partial \phi}{\partial \tilde{\eta}_{a}} \frac{\partial \tilde{\eta}_{a}}{\partial \tilde{L}_{b}} \frac{\partial \tilde{L}_{b}}{\partial \tilde{c}_{k}} \quad \text{(for k=1~4)}$$

5.3.3 Evolution of the Yield Surface Based on the Polycrystal Model

In Chapter 4, it was shown that the coefficients of Yld96 are determined by fitting the yield function to the yield stresses and r-values obtained from uniaxial tension, plane strain and balanced biaxial tests (see Table 4-1). Given a plastic strain path, initial crystallographic texture (Figure 3-3), and an offset plastic strain, the polycrystal model can be used to define the evolved shape of the yield surface. In this method, however, the value of the offset plastic strain has a direct impact on the size of the predicted yield surface [Kuwabara et al. 2000 and Kuroda et al. 1999], and must be carefully chosen. In this work, the value of the offset plastic strain is determined iteratively such that the initial yield surface obtained by the phenomenological model matches that obtained by the polycrystal model very closely. For the 6061-T4 extruded aluminum tubes it was determined that an offset plastic strain value of 0.5% would result in the best match, as shown in Figure 5-1.

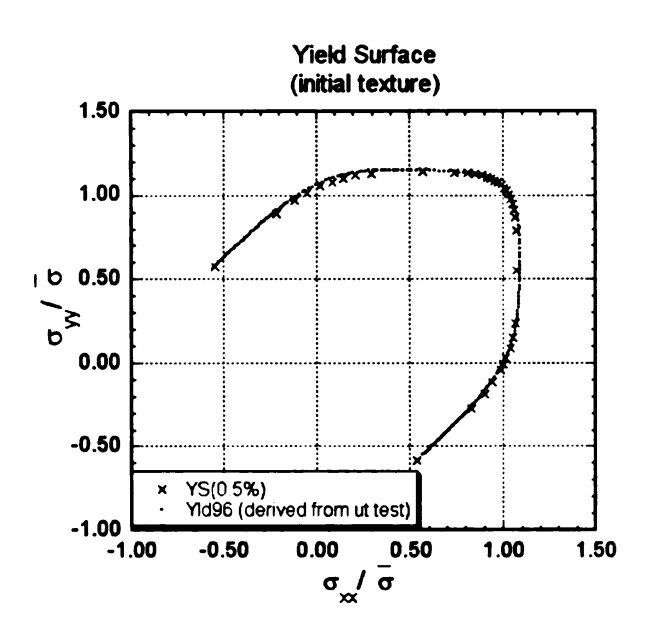


Figure 5-1 Predicted initial yield surface based on a 0.5% plastic strain offset for the 6061-T4 extruded aluminum tube

5.3.4 Evolution of the Yield Surface Based on the Yld96 Yield Function

Based on the method described above, the scalar parameter α was introduced into the ABAQUS implicit code through the UMAT (user material subroutine) written for Barlat's Yld96 yield function. During a finite element run, the anisotropic coefficients c_i are evolved based on Eq. 5-2 for a given value of the scalar parameter α , and the deformation strain path. At the end of the FE run, the evolved anisotropic coefficients c_i are retrieved and used to plot the new yield surface. In this work, all yield surfaces are presented in a normalized form. That is, all stresses are normalized by the effective flow stress, before being plotted. This method allows one to see the evolution of the yield surface shape clearly.

5.4 Evaluation of the Anisotropic Strain Hardening Model

5.4.1 Yield Surface Evolution under Proportional Loading

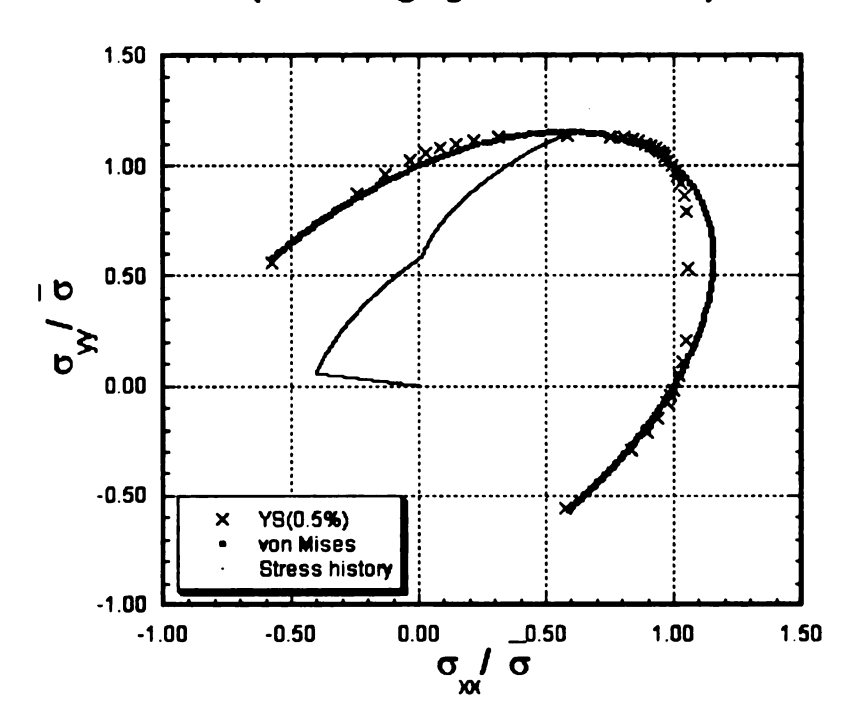
The evolution of the Yld96 yield function following proportional loadings, such as uniaxial tension, plane strain and balanced biaxial tension were investigated. For comparison, the shape of the evolved Yld96 yield function was compared to those predicted by the polycrystal model. Appendix C shows the results of all these yield surface comparisons for those specific proportional loadings mentioned above. In general, it can be concluded that for all loading cases the yield surface shape predicted by the Yld96 yield function and the polycrystal model are in good agreement for all plastic strains less than 25%. This is particularly true for uniaxial and balanced biaxial cases. This comparison is not as good, however, for plane strain cases, and this deviation becomes exacerbated with increased plastic deformation. This deviation could be attributed to that fact that the initial anisotropy coefficients for the Yld96 yield function were fitted to the yield stresses and r-values obtained from uniaxial and balanced biaxial tests and not to the plane strain values.

5.4.2 Yield Surface Evolution under Non-Proportional Loading -Tube Bulging

For the bulge test, with a few iterations it was determined that a value of $\alpha = -0.00001$ would predict a maximum hoop strain of 18.4%, which although not optimal is reasonably close to the experimentally measured value of 19%. The result from the isotropic hardening case (α =0.0) was 19.18%. Figures 5-2a-c show the yield surfaces predicted by several material models for the location where the maximum hoop strain occurs. In this study, strain paths were first obtained from finite element analysis of tube bulging using von Mises, isotropic hardening Yld96, and anisotropic hardening Yld96

models. Figure 5-3 shows that predicted strain paths are different for different material models. Furthermore, Figure 5-3 shows that the von Mises material model predicts a maximum hoop strain of 15.9%. Figures 5-2a-c show the comparison of the phenomenological yield surfaces versus those predicted by the polycrystal model. They also show the corresponding stress paths leading to the final deformation. Figure 5-2a shows that 1) the two yield surfaces do not match very closely, and 2) at the final deformation point, the von Mises yield surface is above the polycrystal yield surface. Figures 5-2b and 5-2c show that 1) the two yield surfaces match closely, and 2) at the final deformation point, both isotropic and anisotropic Yld96 yield surfaces and polycrystal yield surfaces are very close to each other. Considering that the von Mises material model underestimated the experimental hoop strain, while the isotropic and anisotropic Yld96 material models did not, it can be concluded that the above comparison method has some merits. That is, the polycrystal model's result could be used as a mean to evaluate the accuracy of the phenomenological models' strain predictions, where experimental results are either missing or not reliable.

Yield Surface Comparison (element #1429) (Tube bulging with von Mises)



Yield Surface Comparison (element #1429) (Tube bulging with von Mises)

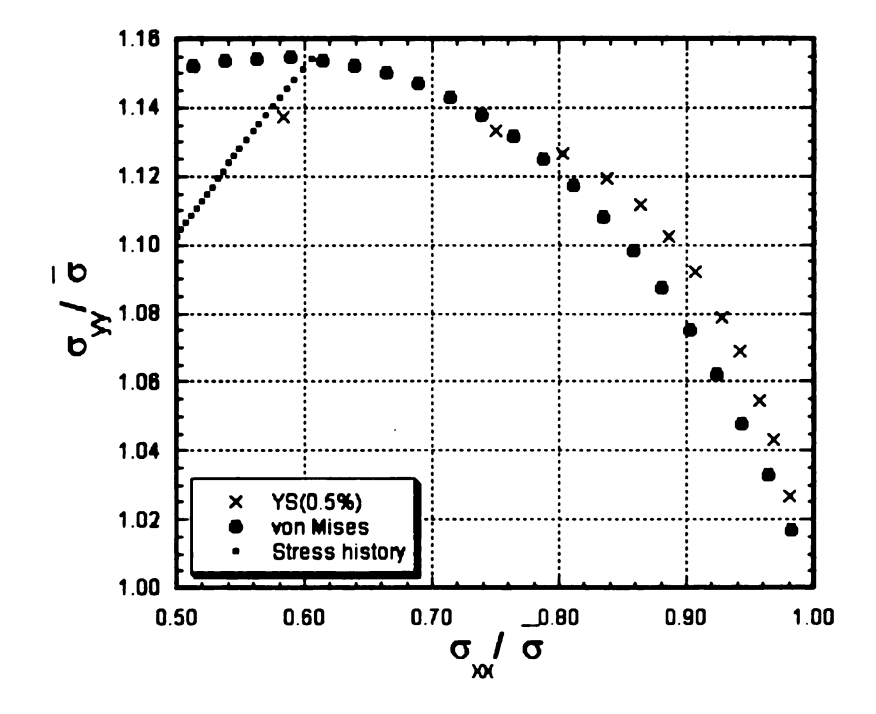
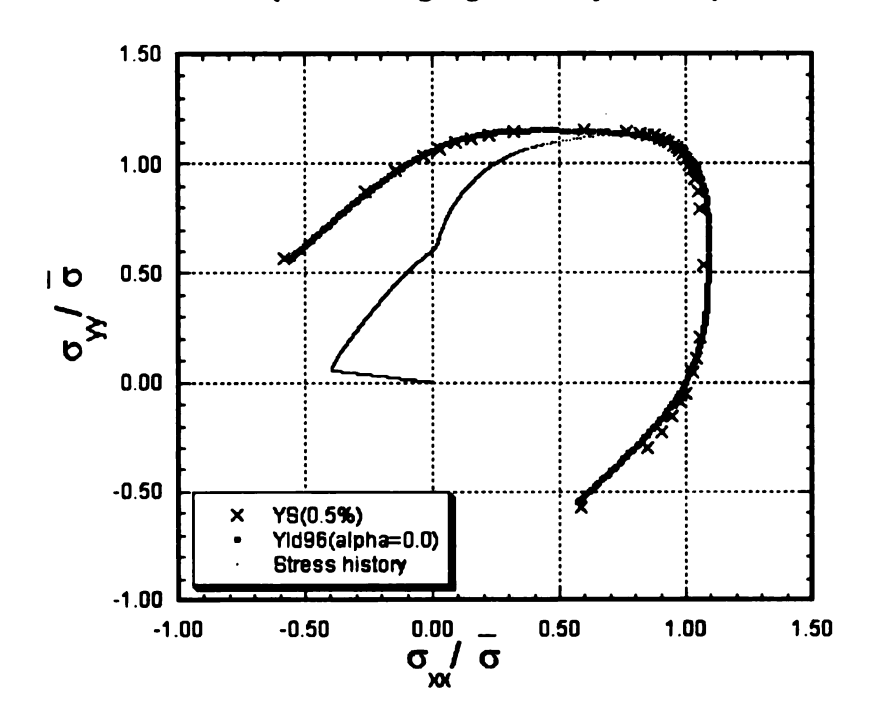


Figure 5-2a Yield surface based on von Mises model

Yield Surface Comparison (element #1429) (Tube bulging with alpha=0.0)



Yield Surface Comparison (element #1429) (Tube bulging with alpha=0.0)

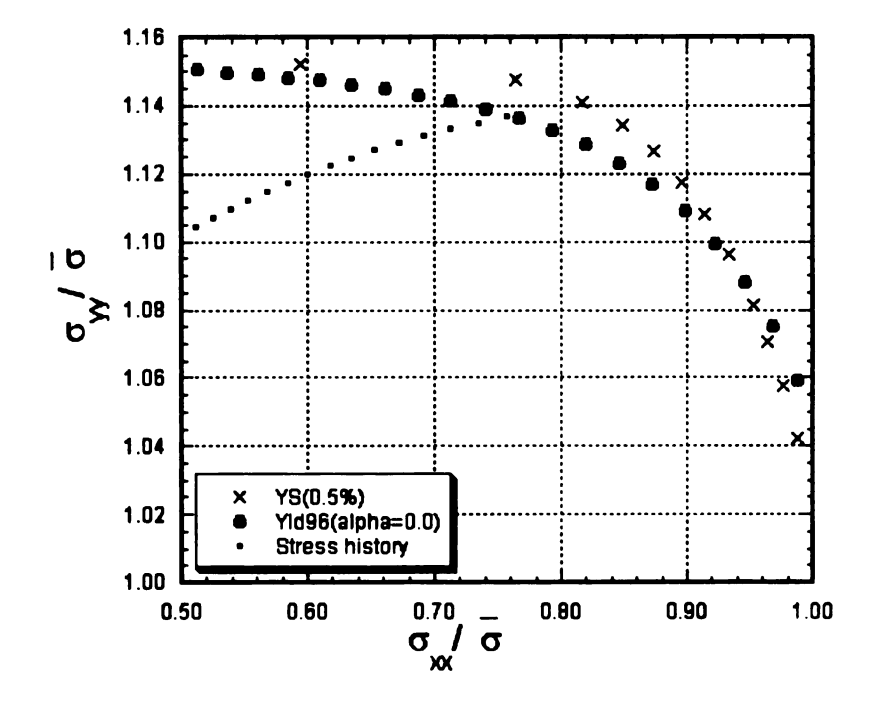
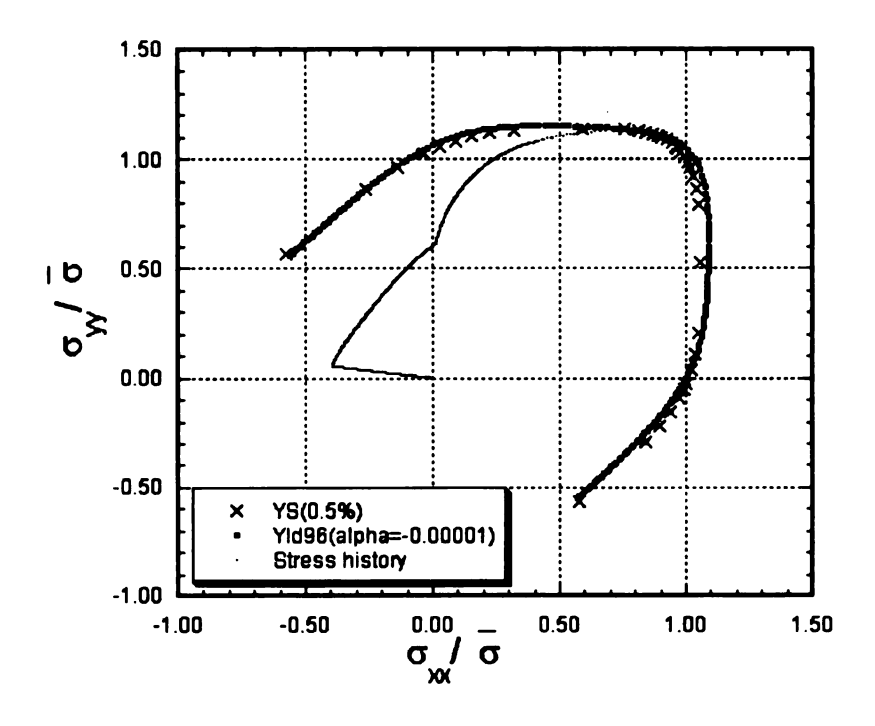


Figure 5-2b Yield surface based on isotropic hardening Yld96 model, α equal to zero

Yield Surface Comparison (element #1429) (Tube bulging with alpha=-0.00001)



Yield Surface Comparison (element #1429) (Tube buiging with alpha=-0.00001)

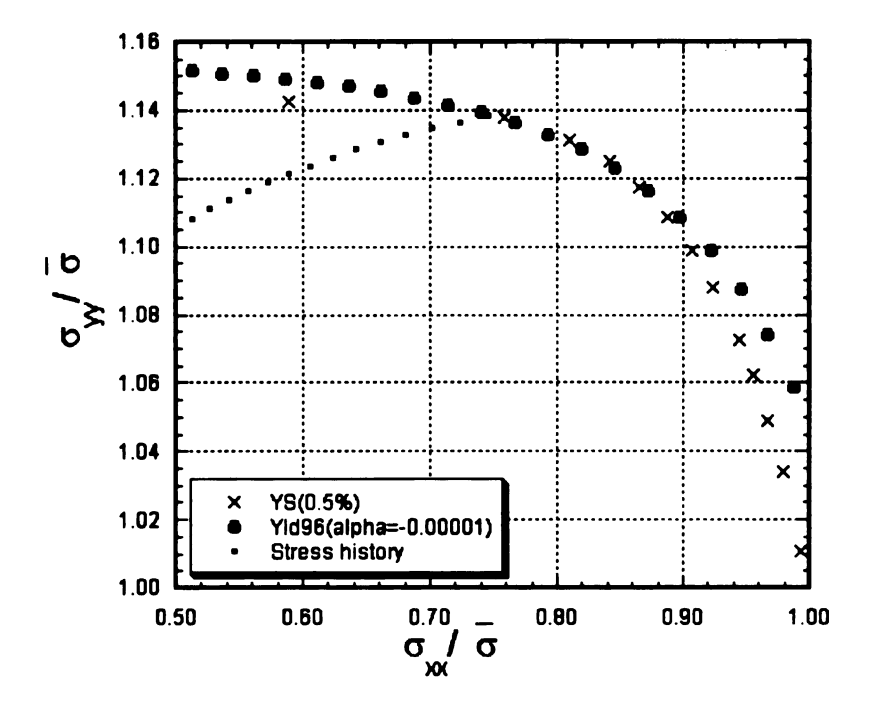


Figure 5-2c Yield surface based on anisotropic hardening Yld96 model, α equal to -0.00001

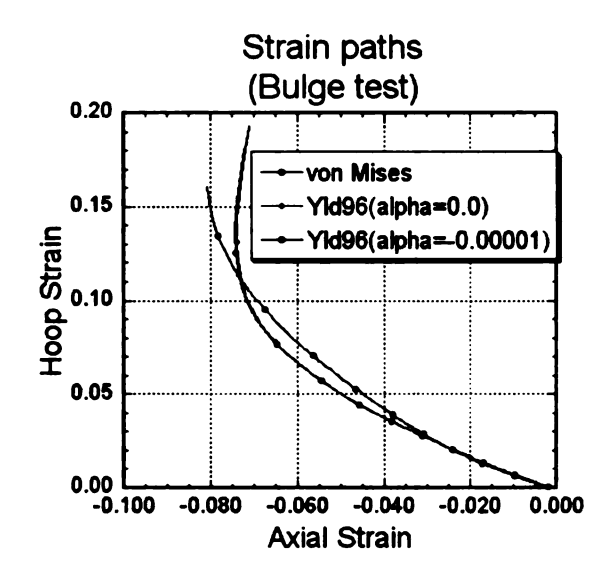


Figure 5-3 Different strain paths predicted by different material models

5.4.3 Yield Surface Evolution under Non-Proportional Loading – Square Die Hydroforming

For the square die simulation, two different locations on the deformed tube were investigated. Element number 1429 was located on the top of the corner region and element number 1421 was located on the region where the tube contacted the die. The strain paths for these two locations obtained from von Mises, isotropic and anisotropic Yld96 material models are shown in Figures 5-4a-b. It is clear that for element 1429, the strain paths for different material models are very different. Interestingly, the anisotropic Yld96 material model with a value of $\alpha = -0.0002$ follows a similar path as that for the von Mises, however, strain paths for Yld96 model with values of $\alpha = -0.00001$ and $\alpha = 0$ are very different. It can also be seen that the von Mises material model predicts a maximum strain of 12.5%, while Yld96 material model predicts 11% (with $\alpha = -0.0002$), 13.8% (with $\alpha = -0.00001$), and 14% (with $\alpha = 0$), respectively.

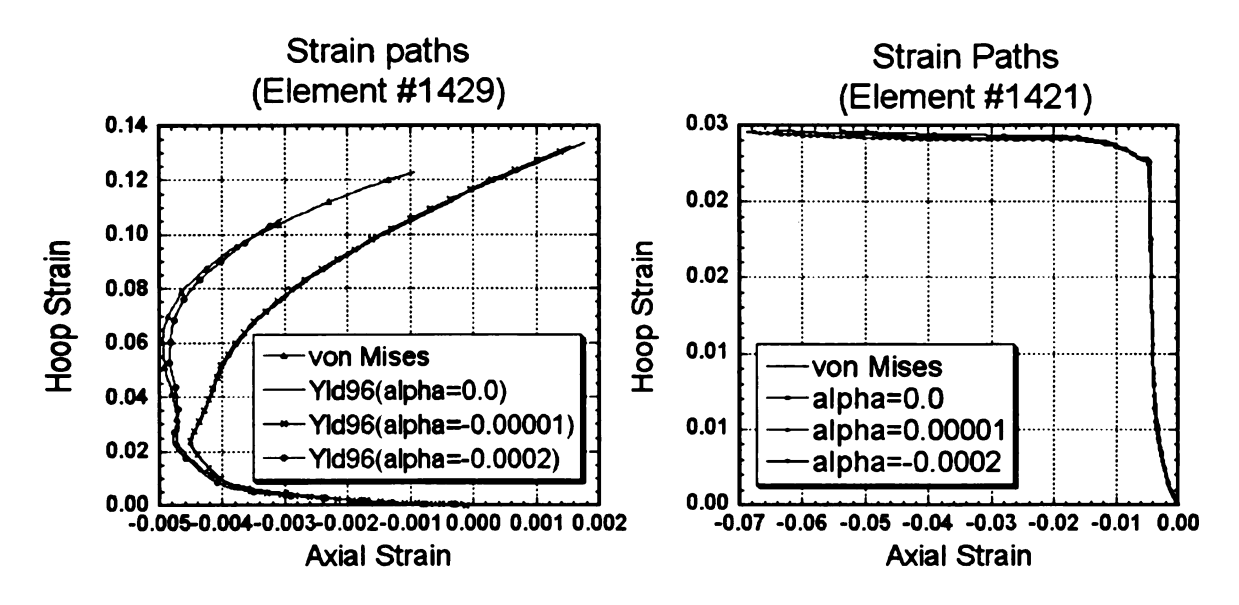


Figure 5-4 (a) Strain paths for element #1429 (b) strain paths for element #1421

The corresponding yield surfaces with different strain paths for element 1429 are shown in Figures 5-5a-d. Figure 5-5a shows that at the final deformation point the von Mises yield surface is slightly above the polycrystal yield surface, indicating that strain prediction with von Mises will slightly underestimate the experimental value. Figures 5-5b and 5-5c show an almost perfect match between the two yield surfaces, indicating a very close match between the predicted and measured strain values. Figure 5-5d represents the worse case, where the Yld96 yield surface with $\alpha = -0.0002$ is grossly above the polycrystal yield surface, indicating a gross underestimation of the predicted strain. In fact, this case had the lowest strain prediction. A comparison of these strain predictions with the experimentally measured strains in Figures 4-9a-c indicates that probably strain measurements for sample H4 are not reliable.

Figures 5-6a-d show the yield surface comparisons for element 1421. It can be seen that Yld96 isotropic and anisotropic material models, regardless of the value of α , obtain the best matches. The worst match is for the case of von Mises material model (Figure 5-6a)

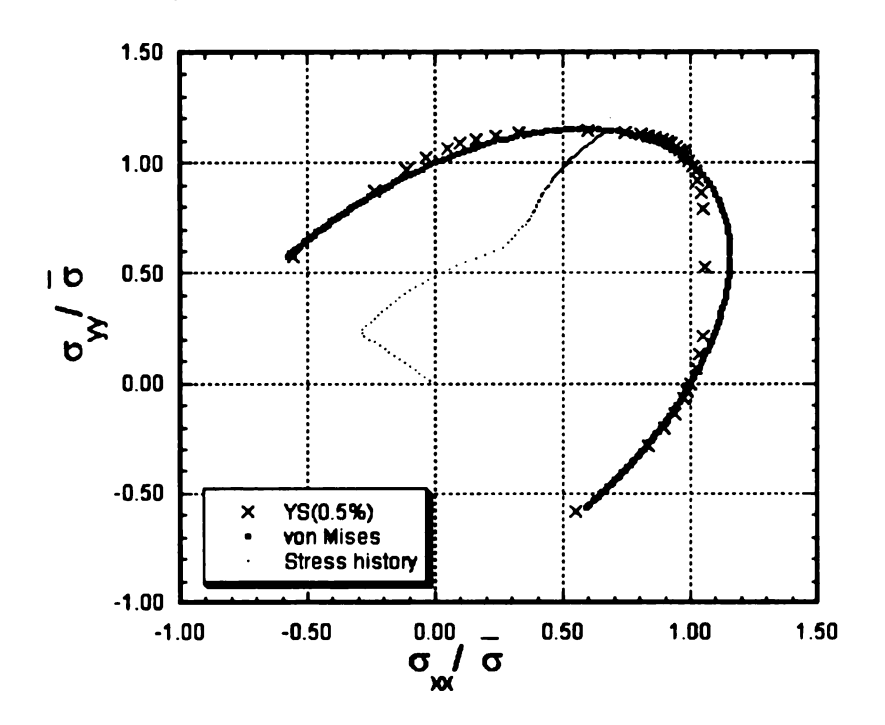
where it is expected for the strains to be underestimated. It can be concluded that since total strain for element 1421 is very small (~ 3%), any small variation in the strain prediction by the four models may be difficult to distinguish. Table 5-1 shows the hoop strain of element 1421 for different yield functions.

	Element #1421	Element #1429
Von Mises	0.0247	0.1231
Yld96 (α=0.0)	0.0246	0.1337
Yld96 (α=-0.00001)	0.0246	0.1323
Yld96 (α=-0.0002)	0.0246	0.1057

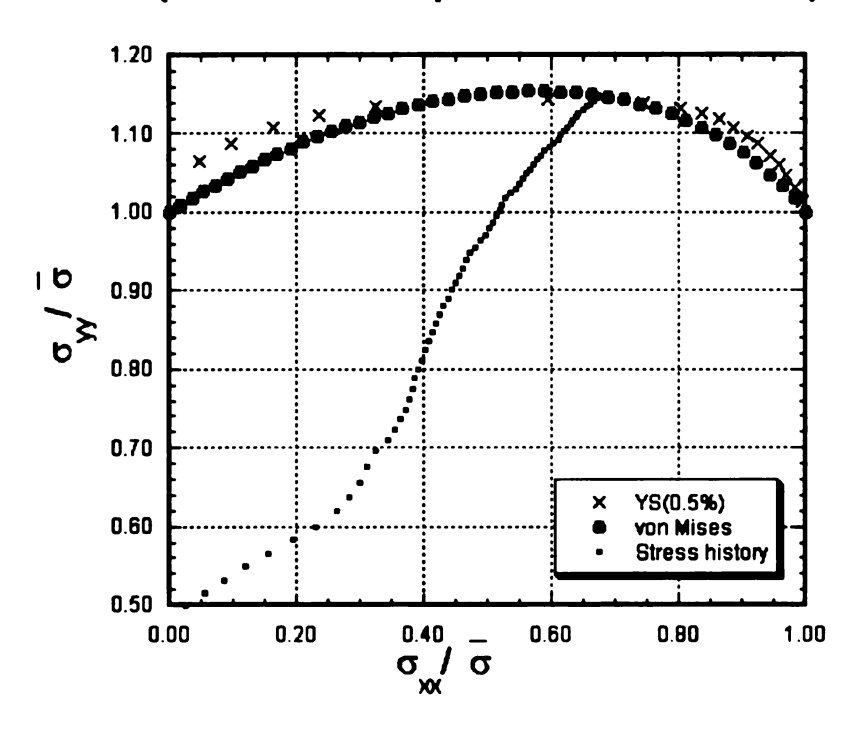
Table5-1 Hoop strain at element 1421&1429 for different yield functions

Finally, Figure 5-7 shows the variation in the strain prediction for square die hydroforming as a function of different α -values. It can be seen that with different α -values, vastly different strain distribution can be predicted, which is not possible with other material models such as von Mises, or the original Yld96 with isotropic hardening. However, to verify which α -value is correct will require the comparison of the phenomenological yield surfaces with those obtained from the polycrystal model. In the case of 6061-T4 extruded aluminum tube, the value of α = -0.00001 is the correct value to use.

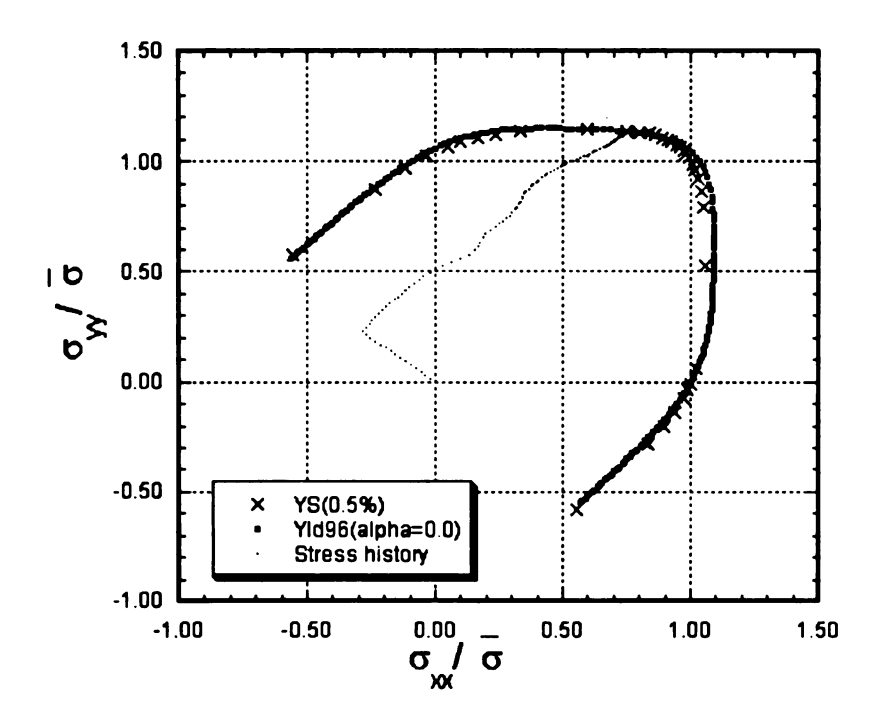
Yield Surface Comparison (element #1429) (Deformation in square die with von Mises)



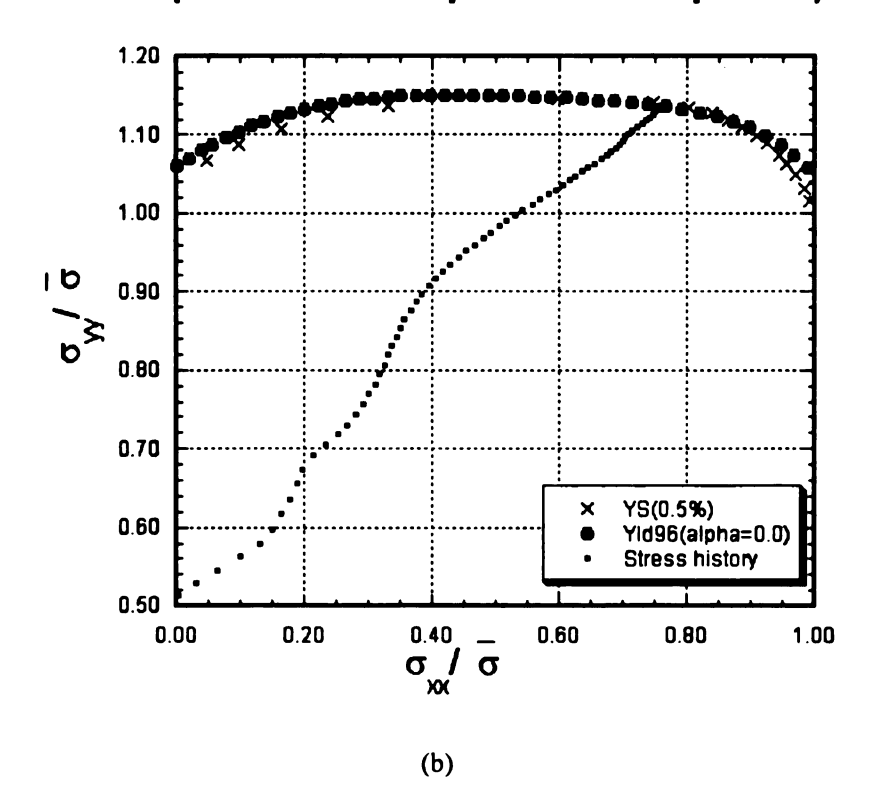
Yield Surface Comparison (element #1429) (Deformation in square die with von Mises)



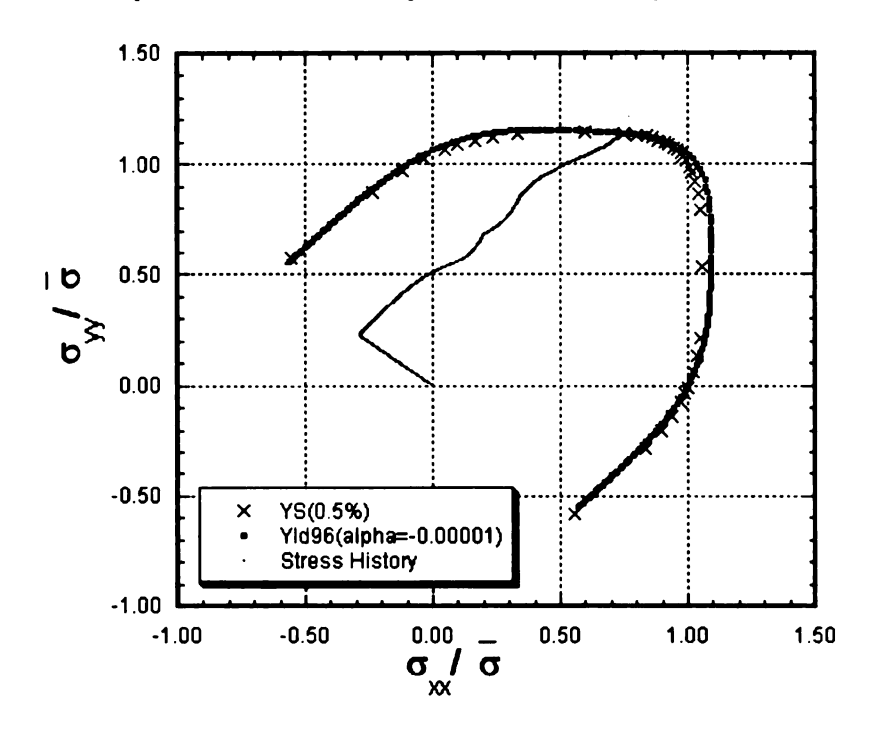
Yield Surface Comparison (element #1429) (Deformation in square die with alpha=0.0)



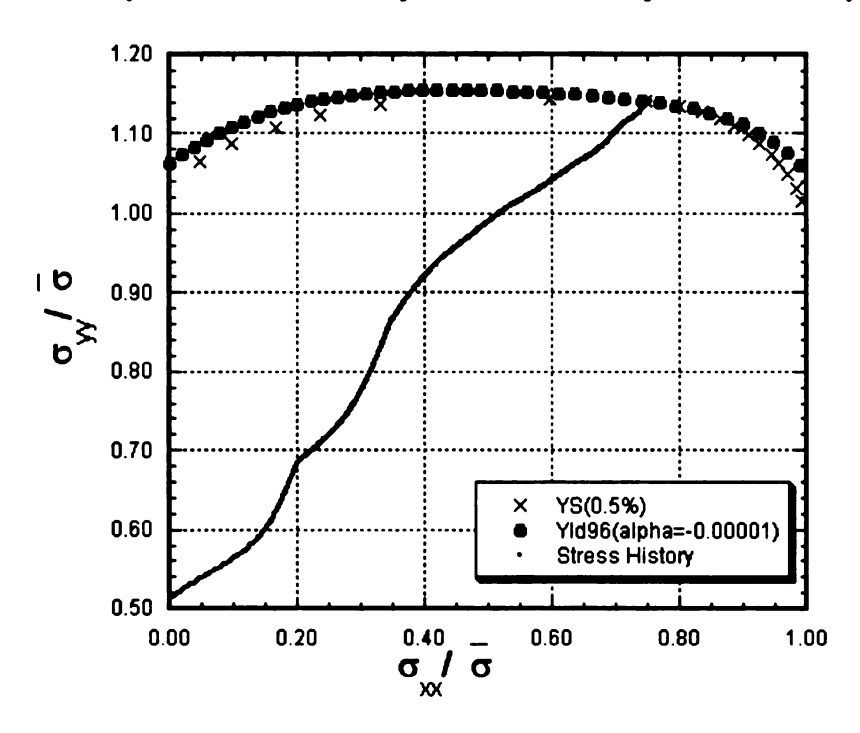
Yield Surface Comparison (element #1429) (Deformation in square die with alpha=0.0)



Yield Surface Comparison (element #1429) (Deformation in square die with alpha=-0.00001)



Yield Surface Comparison (elemet #1429) (Deformation in square die with alpha=-0.00001)



Yield Surface Comparison (element #1429) (Deformation in square die with alpha=-0.0002)

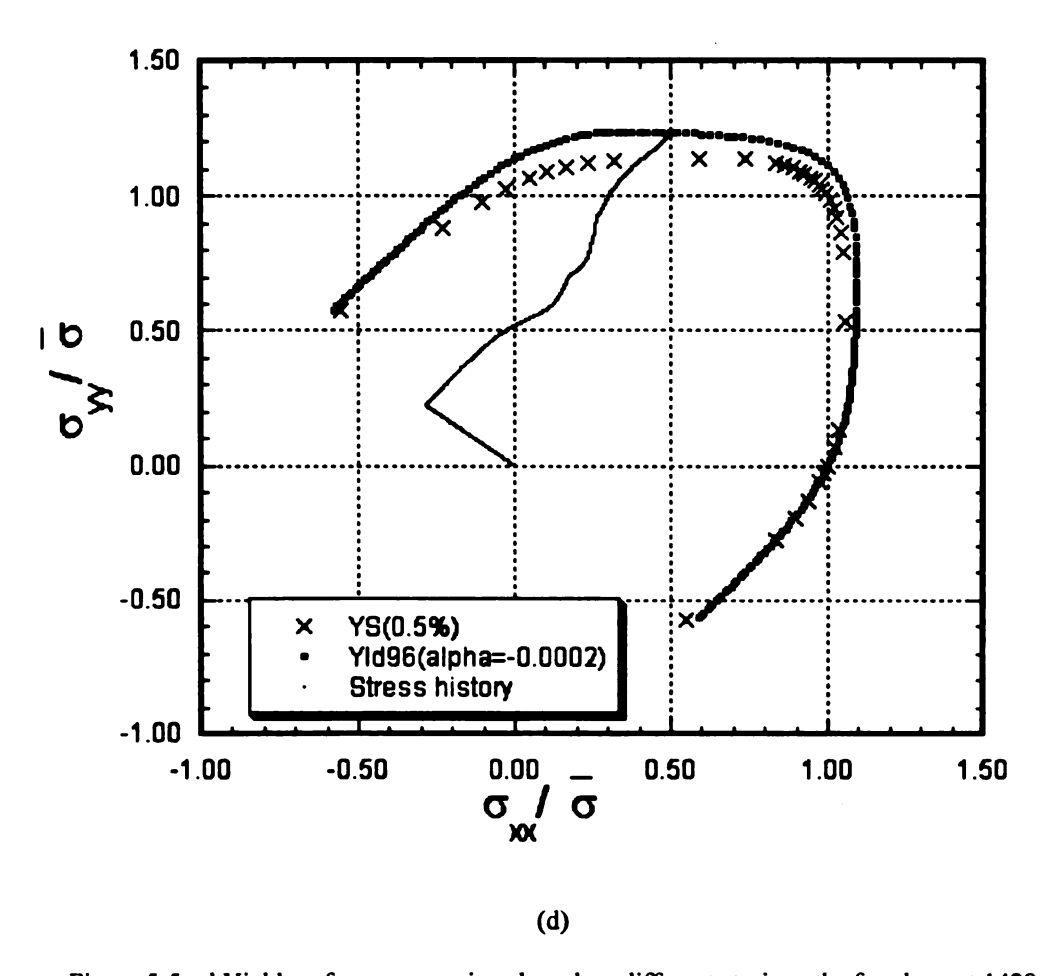
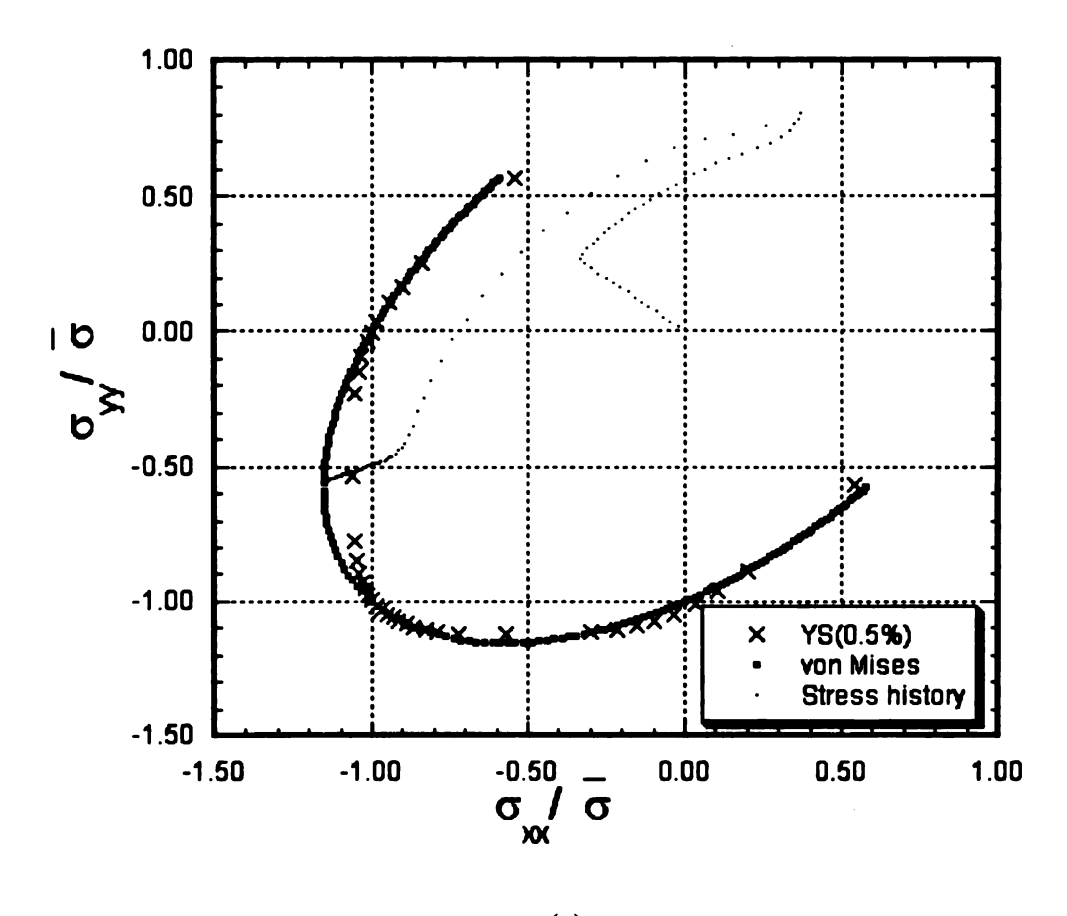
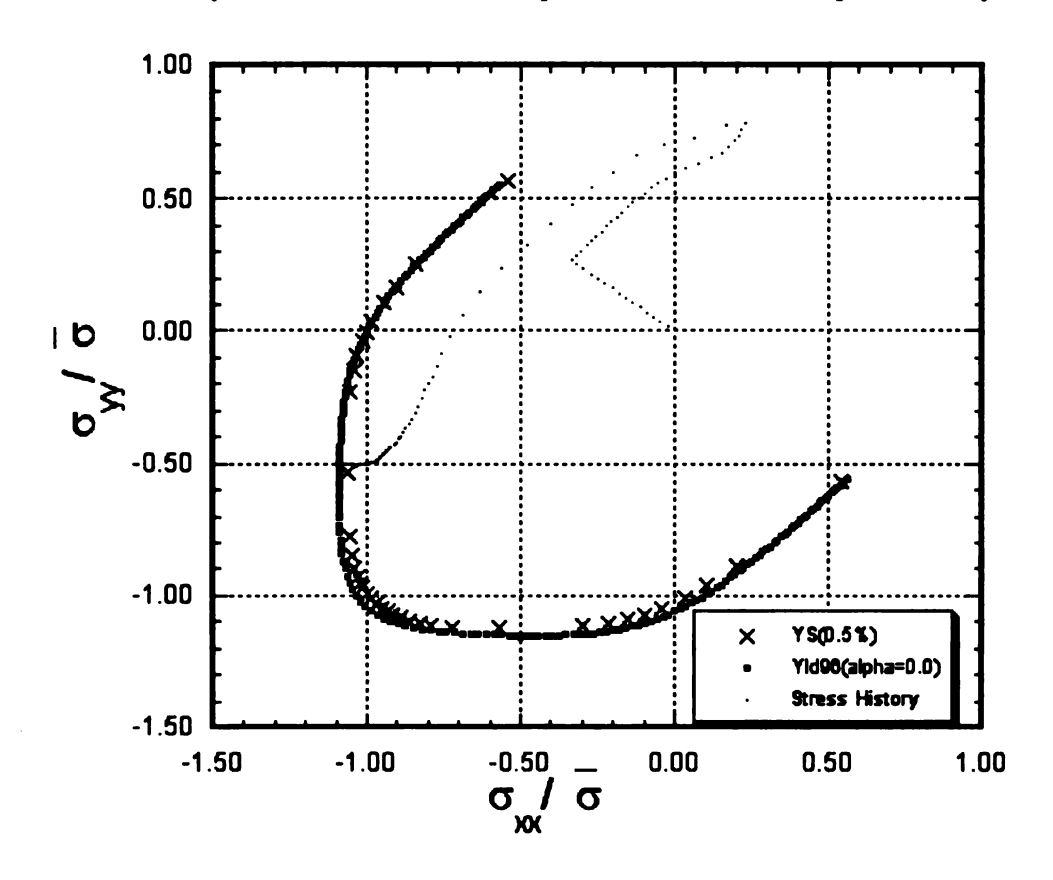


Figure 5-5a-d Yield surfaces comparison based on different strain paths for element 1429

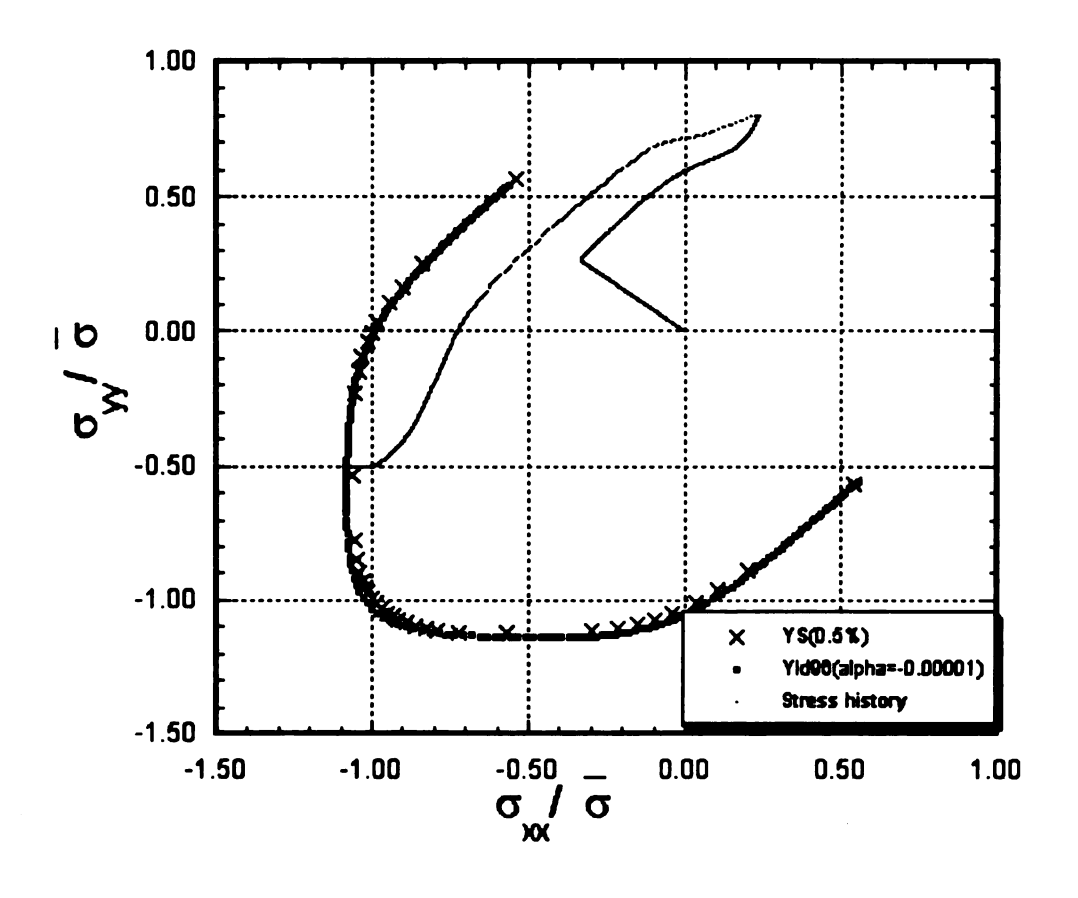
Yield Surface Comparison (element #1421) (Deformation in square die with von Mises)



Yield Surface Comparison (element #1421) (Deformation in square die with alpha=0.0)



Yield Surface Comparison (element #1421) (Deformation in square die with alpha=-0.00001)



Yield Surface Comparison (element #1421) (Deformation in square die with alpha=-0.0002)

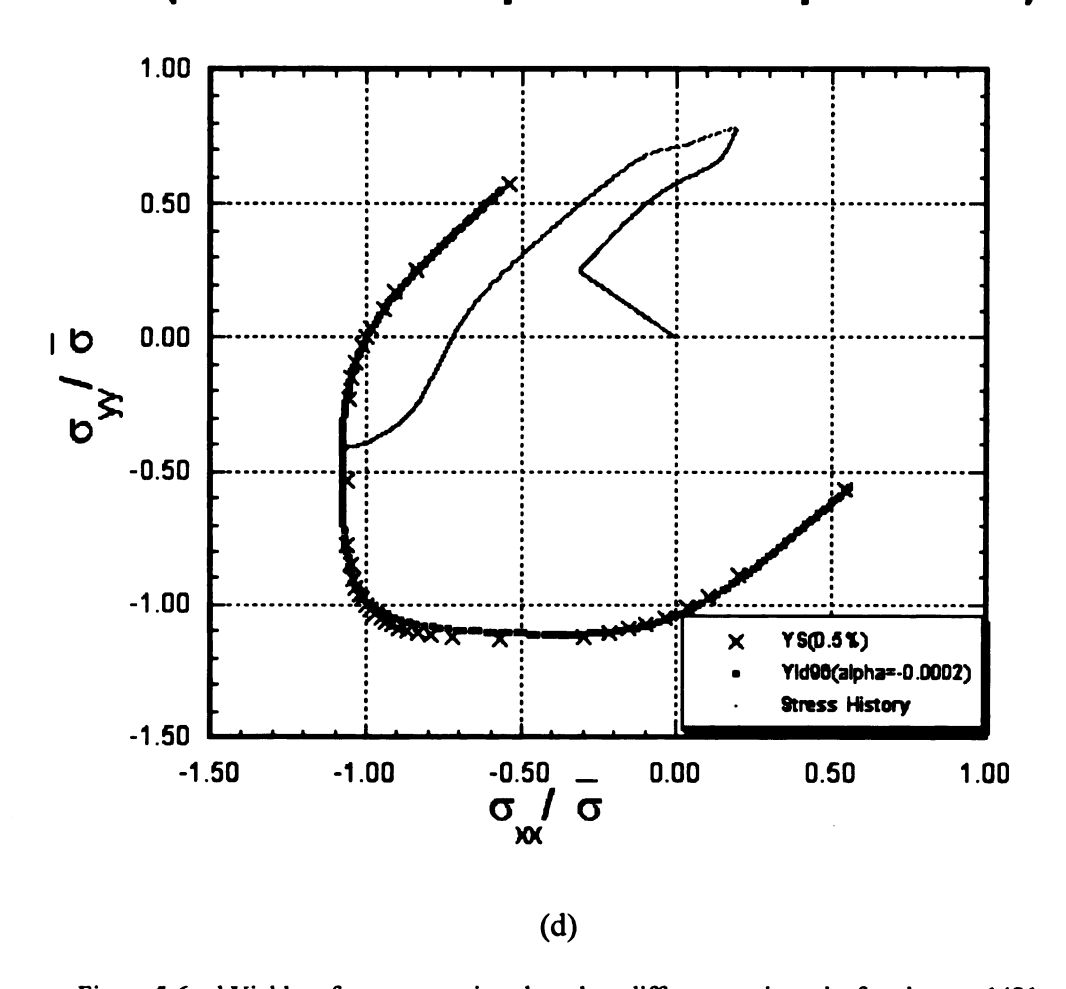


Figure 5-6a-d Yield surfaces comparison based on different strain paths for element 1421

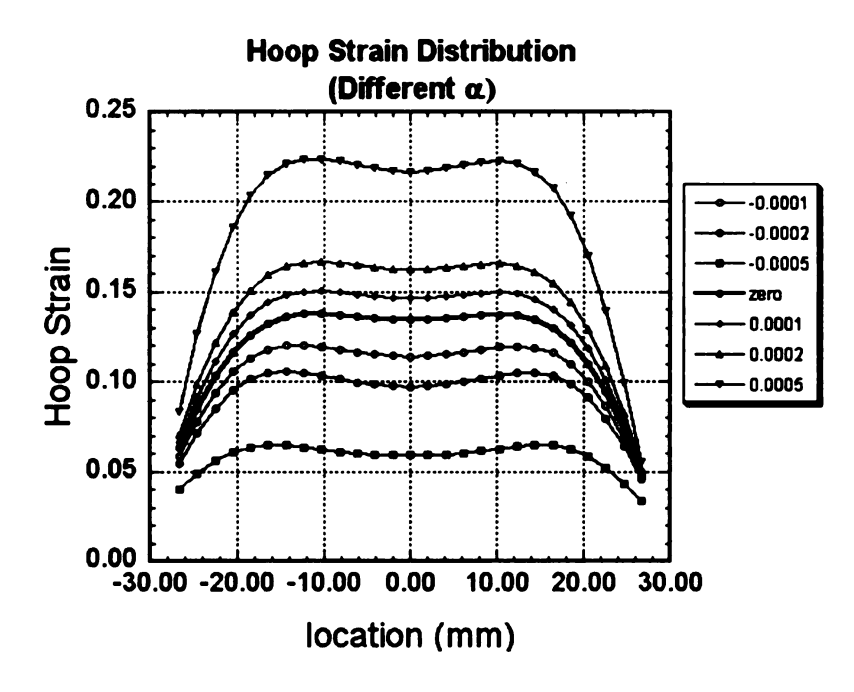


Figure 5-7 Hoop strain distributions with different α -values

CHAPTER 6

EXPERIMENTAL SETUP AND PROCESS

6.1 Experiment Setup

The experiments on tube hydroforming were conducted in the MSU laboratory using a tube hydroforming press system purchased from Interlaken Technology Corporation (see Figure 6-1). This hydroforming press system consists of the following sub-systems: hydraulic press (ServoPress), hydroforming feed actuators, pressure intensifier, tooling and controller.

The ServoPress is a single acting servo-controlled hydraulic press including Interlaken's UniPress control hardware and software. The ServoPress provides clamp force and punch force that is used for sealing of tube ends and end feed of specimen. Both punch and clamp are controlled using either load or position as the primary feedback. High speed data acquisition records and displays all measured variables on the computer screen.

The pressure intensifier system is a cabinet mounted system powered by shop air (80-120 psi). The system is completely plumbed and includes all manifolds and pressure control valves. The pressure intensifier system provides fluid pressure of up to 30,000 psi and is also controlled by the system computer.

The standard tooling is designed for tubes with 2.00" OD (outer diameter). Standard tooling provides changeable inserts for hydroforming various shapes and various strains. Complete die set (see Figure 6-2) for performing both constrained forming and unconstrained burst tests of 2.00 OD tubes is available. More specifically, the following Cavity shapes are available: Unconstrained burst; square section 2.00 inches (. 250 corner

radii); square section 2.50 inches (.375 corner radii); constrained hydraulic bulge (2.00 spherical radius). The system also includes docking rods and pressure porting to bring high pressure fluid from pressure intensifier.



Figure 6-1 Experimental setup in MSU laboratory

6.2 Tube hydroforming process

Generally in internal high pressure forming processes a tube is sealed at both ends. Then the tube is filled with a hydraulic fluid e.g. a mixture of oil/water. The sealed tube is placed into an encapsulating die and the component is formed by the application of hydrostatic pressure. In addition, an axial force is applied with horizontal rams (plunger) to seal the tube and to introduce axial compressive stress into the tube wall and force the material to move towards the forming zone (Figure 6-3).

Important for the successful employment of this process is the knowledge of the necessary process characteristic. The load paths of the internal pressure and the axial forces have decisive influence on the forming process [Asnafi 2000, Trana 2002, Manish et al. 2003]. Too low internal pressure and too high axial forces can lead to bucking or wrinkling in the tube. Too high internal pressure together with too low axial forces can

lead to bursting of the tube (Figure 6-4). Failure modes occurring in tube hydroforming can be seen in Figure 6-5.



Figure 6-2 The die set used for experiment

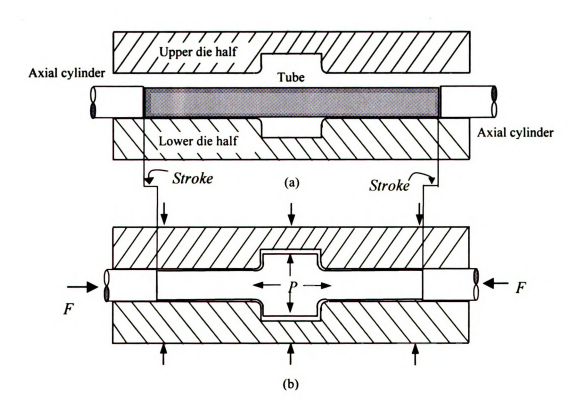


Figure 6-3 The principle of tube hydroforming: (a) original tube shape and (b) final tube shape (before unloading). The figure is extracted fromAsnafi (2000)

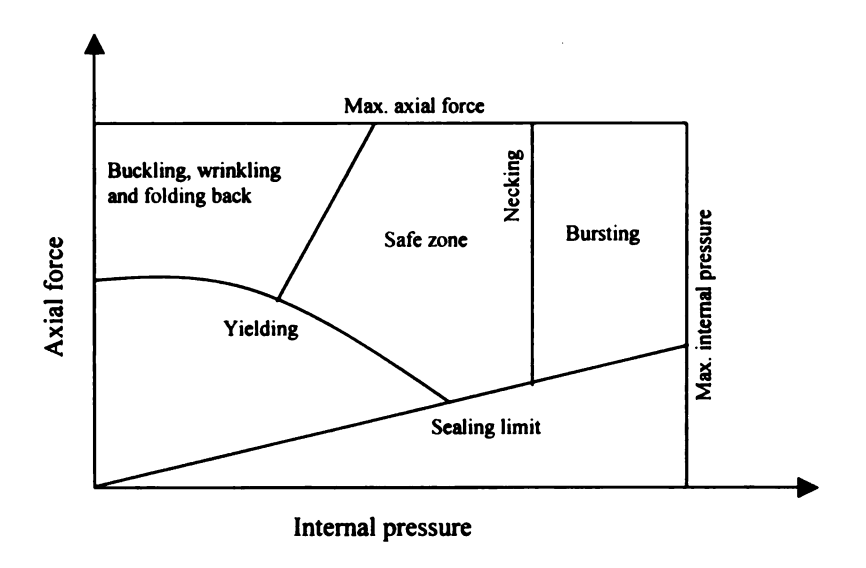


Figure 6-4 Working diagram for the hydroforming process (extracted from Trana (2002))



Figure 6-5 Failure modes occurring in tube hydroforming

6.3 Sequence of operation in experiment

The typical sequence of operations comprising the tube hydroforming process in MSU is as follows:

- 1. The tube is placed in the lower die.
- 2. The upper die is brought down to closed position.
- 3. The seal are advanced to sealing position.
- 4. The tube is filled with liquid and pressurized to hydroforming pressure.

- If axial feed is required, the end seals are simultaneously advanced to push the required amount of material into the die cavity.
- 6. Pressure in the tube is reduced to atmospheric level.
- 7. The upper die goes up.
- 8. The hydroformed part is withdrawn from the lower die.

Figure 6-6 shows some deformed tubes made from both bulge and square die without failure.





Figure 6-6 Deformed tubes without failure

APPENDIX A

INTRODUCTION TO SPIN AND ROTATION

A rotation matrix for small (infinitesimal) rotations

(From Crisfield, 1991)

In the Figure A1(b), a vector r_0 is rotated in the 1-2 plane through $\Delta\theta$ to become a vector \mathbf{r}_n . We could therefore write

$$\mathbf{r}_{n}^{T} = r_{0} \left\{ \cos(\theta_{0} + \Delta \theta), \sin(\theta_{0} + \Delta \theta), 0 \right\}$$
(A1)

Alternatively, an approximation would involve

$$\mathbf{r}_{\mathbf{n}} = \mathbf{r}_{0} + \Delta \mathbf{r} = r_{0} \mathbf{t} + r_{0} \Delta \theta \mathbf{n}$$
 (A2)

where $r_0 = ||\mathbf{r}_0||$, \mathbf{n} is the unit vector orthogonal to both \mathbf{r}_0 and the z-direction(or \mathbf{e}_3) so that $\mathbf{t}^T \mathbf{n} = \mathbf{e}_3^T \mathbf{n} = 0$ and hence

$$\mathbf{n}^{\mathsf{T}} = \{-\sin\theta_0, \cos\theta_0, 0\} \tag{A3}$$

Hence (A2) can be rewritten as

$$\mathbf{r}_{n} = \begin{bmatrix} 1 & 0 & 0 \\ 0 & 1 & 0 \\ 0 & 0 & 1 \end{bmatrix} + \begin{bmatrix} 0 & -\Delta\theta & 0 \\ \Delta\theta & 0 & 0 \\ 0 & 0 & 0 \end{bmatrix} \mathbf{r}_{0}$$
 (A4)

or

$$\mathbf{r}_{0} = \mathbf{R}\mathbf{r}_{0} = [\mathbf{I} + \mathbf{S}(\Delta \mathbf{\theta})]\mathbf{r}_{0} \tag{A5}$$

This relationship can be accompanied by

$$\mathbf{\theta}_{n} = \mathbf{\theta}_{0} + \Delta \mathbf{\theta} = \theta_{0} \mathbf{e}_{3} + \Delta \theta \mathbf{e}_{3} = (\theta_{0} + \Delta \theta) \mathbf{e}_{3}$$
 (A6)

because in two dimensions rotations are additive. For the two-dimensional problem of Figure A1(b), there is no point in adopting (A4) instead of the simpler exact form of (A1). However, (A2) can be generalized (Figure A1(c)) to

$$\mathbf{r}_{n} = \mathbf{r}_{0} + \Delta \mathbf{r} = \mathbf{r}_{0} + (\Delta \mathbf{\theta} \times \mathbf{r}_{0}) \tag{A7}$$

where the symbol x denotes a cross-product so that $(\Delta \theta \times \mathbf{r}_0)$ is orthogonal to both $\Delta \theta$ and \mathbf{r}_0 and is of magnitude $\Delta \theta r_0 \sin \beta$, where (Figure A1(c)) β is the angle between $\Delta \theta$ and \mathbf{r}_0 . Equation (A7) can be recast in the form of (A5) with

$$\mathbf{S}(\Delta \boldsymbol{\theta}) = \begin{bmatrix} 0 & -\Delta \theta_3 & \Delta \theta_2 \\ \Delta \theta_3 & 0 & -\Delta \theta_1 \\ -\Delta \theta_2 & \Delta \theta_1 & 0 \end{bmatrix}$$
(A8)

With infinitesimal rotation, $\Delta \theta$ represents the 'spin'.

Large rotations (Euler's theorem)

(From Belytschko, 2000)

A fundamental concept in large rotations is the Euler's theorem. This theorem states that in any rigid body rotation, there exists a line which remains fixed: the body rotates about this line. From this theorem general formulas for the rotation matrix can be developed. Consider the rotation of vector \mathbf{r} by an angle θ about the axis defined by the unit vector $\mathbf{e} = \mathbf{e}_1$. The vector after the rotation is denoted by \mathbf{r}' as shown in Figure A2. The rotation matrix \mathbf{R} relates \mathbf{r}' to \mathbf{r} by

$$\mathbf{r}' = \mathbf{R}\mathbf{r} \tag{A9}$$

where R is to be determined. We will first derive the formula

$$\mathbf{r}' = \mathbf{r} + \sin \theta \mathbf{e} \times \mathbf{r} + (1 - \cos \theta) \mathbf{e} \times (\mathbf{e} \times \mathbf{r})$$
 (A10)

where e is a unit vector along the axis of rotation, whose existence we know by Euler's theorem. The schematic on the right hand side of Figure A2 shows the body as viewed along the e axis. It can be seen from this schematic that

$$\mathbf{r}' = \mathbf{r} + \mathbf{r}_{PQ} = \mathbf{r} + \alpha \sin \theta \mathbf{e}_2 + \alpha (1 - \cos \theta) \mathbf{e}_3 \text{ where } \alpha = r \sin \phi$$
 (A11)

From the definition of the cross-product it follows that:

$$\alpha \mathbf{e}_2 = r \sin \phi \mathbf{e}_2 = \mathbf{e} \times \mathbf{r}, \ \alpha \mathbf{e}_3 = r \sin \phi \mathbf{e}_3 = \mathbf{e} \times (\mathbf{e} \times \mathbf{r})$$
 (A12)

Substituting (A12) into (A11) yields (A10).

Replacing
$$\mathbf{e} \times (\mathbf{e} \times \mathbf{r}) = (\mathbf{e} \cdot \mathbf{r})\mathbf{e} - (\mathbf{e} \cdot \mathbf{e})\mathbf{r} = (\mathbf{e} \cdot \mathbf{r})\mathbf{e} - \mathbf{r}$$
 into A(10)

We obtain

$$\mathbf{r}' = \cos\theta\mathbf{r} + (\mathbf{e}\cdot\mathbf{r})(1-\cos\theta)\mathbf{e} + \sin\theta\mathbf{e}\times\mathbf{r}$$
 (A13)

This will be implemented to calculate the spin for each single crystal in the polycrystal modeling in Chapter 3.

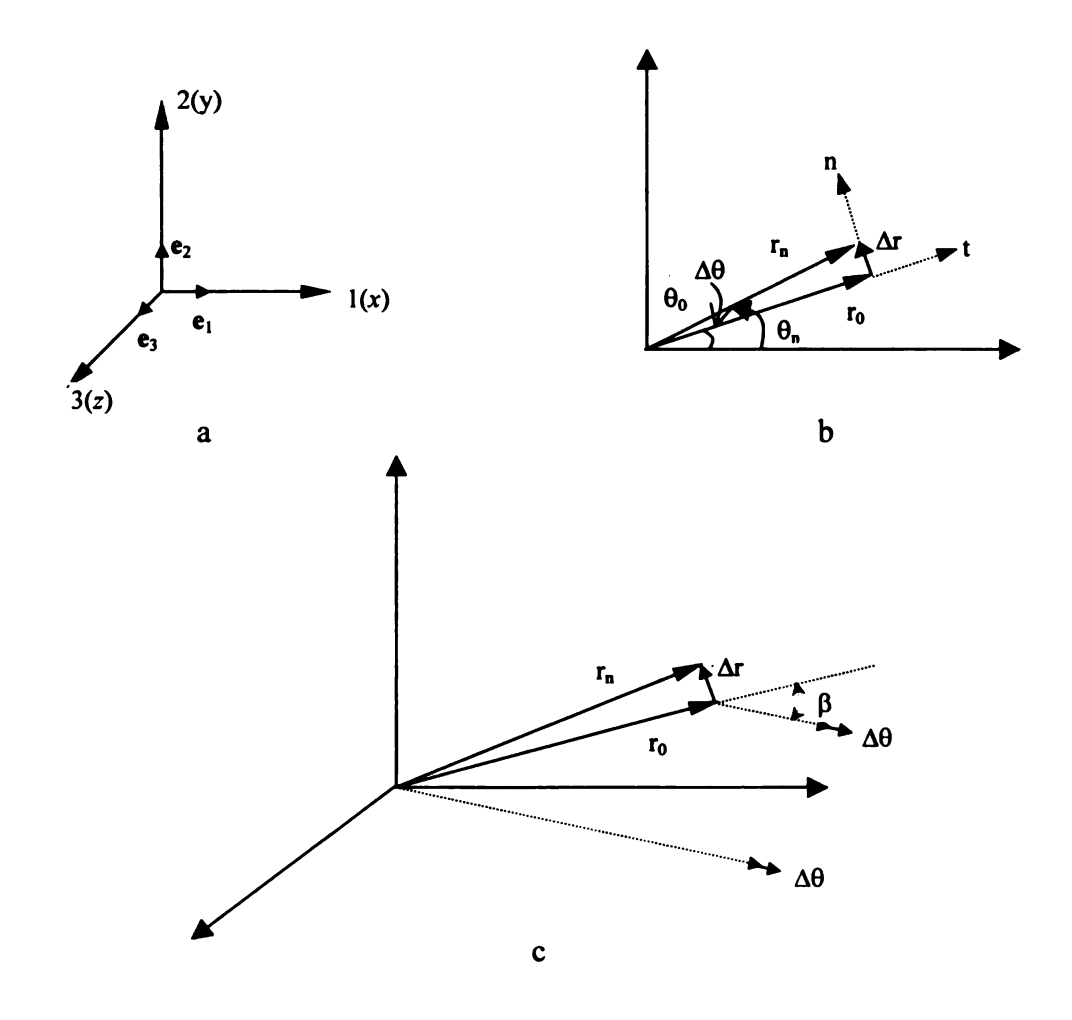


Figure A1 (a) Axes and unit base vectors; (b) two-dimensional rotation; (c) small three-dimensional rotation.

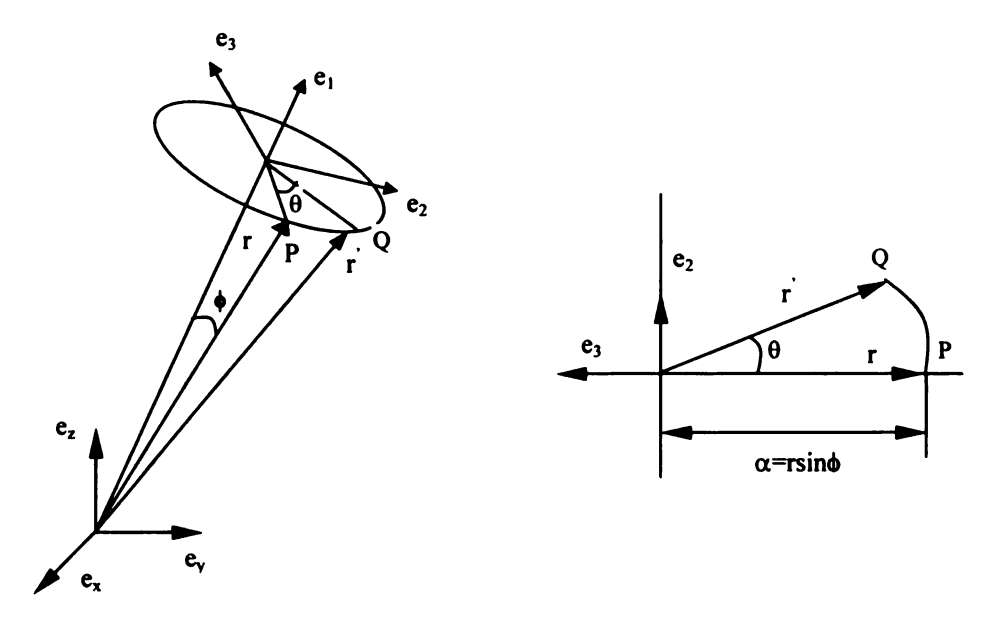


Figure A2 Rotation of a vector \mathbf{r} viewed as a rotation about a fixed axis θ = θ e according to Euler's theorem; on the right a top view along the θ axis is shown

APPENDIX B

CALCULATION OF ANISOTROPIC COEFFICIENTS FOR PLANE STRESS CASE OF YLD96

Definition of the Input Data

The yield function coefficients can be calculated from the results of the following four mechanical tests; uniaxial tension test in three different directions and hydraulic bulge test), or from polycrystalline model which can numerically predict the flow stresses and r-values for the material.

For an aluminum sheet, balanced biaxial yield stress σ_b , the three uniaxial yield stresses $(\sigma_0, \sigma_{45}, \sigma_{90})$ and r-values (r_0, r_{45}, r_{90}) are determined at 0, 45 and 90 degree from the rolling direction. For an extruded aluminum tube, the yield stress in the extrusion direction (ED) can be measured from a uniaxial tensile test; however, it is very difficult to measure the yield stress and r-value in the tangential direction (TD), radial direction (RD) and the 45 degree between ED and TD. In this work, all the coefficients were determined from the polycrystal model using the undeformed tube's crystallographic texture information as input. Actually, we used the flow stresses as input data instead of yield stresses. The reasons being that: 1) The yield stress is determined in the region of the stress-strain curve where the slope is the steepest and this may provide additional inaccuracy, 2) The yield stress is associated with a very small plastic strain and might not reflect the anisotropy of the material over a larger strain range, 3) for aluminum alloys, experimental observation show that after a few percent plastic strain, this flow stress does not vary significantly [Barlat et al. 1997].

Calculation of the Yield Function Coefficients

For an aluminum alloy sheet, seven experimental input data $(\sigma_b, \sigma_0, \sigma_{45}, \sigma_{90}, r_0, r_{45}, r_{90})$ and for an aluminum extruded tube, flow stresses and r values in 4 directions are numerically determined by polycrystal model $(\sigma_{ED}, \sigma_{RD}, \sigma_{TD}, \sigma_{45}, r_{ED}, r_{TD}, r_{TD}, r_{45})$ in order to calculate the seven independent anisotropic coefficients $(C_1, C_2, C_3, C_6, \alpha_x, \alpha_y, \alpha_{z1})$.

For uniaxial tension in the extrusion direction, the components of the tensor s (see Eq4-9-1-3) becomes

$$s_{x} = \frac{c_{3} + c_{2}}{3} \sigma_{ED}$$

$$s_{y} = -\frac{c_{3}}{3} \sigma_{ED}$$

$$s_{z} = -\frac{c_{2}}{3} \sigma_{ED}$$
(B.1)

Combined with the yield function (Eq.4-8), it is possible to write the following equation:

$$F_{1} = \alpha_{x} |c_{2} - c_{3}|^{a} + \alpha_{y} |2c_{2} + c_{3}|^{a} + \alpha_{z0} |c_{2} + 2c_{3}|^{a} - 2 \left(\frac{3\overline{\sigma}}{\sigma_{ED}}\right)^{a} = 0$$
 (B.2)

Similarly, for uniaxial tension in the tangential direction and compression in the radial direction (equivalence of balanced biaxial tension in hydraulic bulge test), it is possible to write the following equations

$$F_{2} = \alpha_{x} |c_{3} + 2c_{1}|^{a} + \alpha_{y} |c_{3} - c_{1}|^{a} + \alpha_{z0} |2c_{3} + c_{1}|^{a} - 2\left(\frac{3\overline{\sigma}}{\sigma_{TD}}\right)^{a} = 0$$
 (B.3)

$$F_3 = \alpha_x |2c_1 + c_2|^a + \alpha_y |c_1 + 2c_2|^a + \alpha_{z0} |c_1 - c_2|^a - 2\left(\frac{3\overline{\sigma}}{\sigma_{RD}}\right)^a = 0$$
 (B.4)

It is possible to find c_1, c_2 , and c_3 through these equations (B.2-B.4) using Newton-Raphson method. To solve this system, it is necessary to assume some values for α_x and α_y , for instance $\alpha_x = \alpha_y = 1$. Then α_x and α_y are modified in an iterative manner in order to modify the slope of the yield surface at the uniaxial loading stress state which is related to the corresponding r values [Yoon et al. 2000].

The above method allows the calculation of c_1, c_2, c_3, α_x and α_y . A similar iterative procedure is used to calculate c_6 and α_{z1} by matching the flow stress σ_{45} and r-value, r_{45} , for the uniaxial tension at 45° between ED and TD.

Flow Stresses and r-values in 4 Different Directions Along the Tube

The predicted uniaxial tension stress-strain curves up to a strain of ε =0.25 in different specimen orientations were used to numerically determine r values and flow stresses at equal amount of plastic work [Barlat et al. 1997]. The uniaxial directions considered were the extrusion direction, ED; the tangential direction, TD; the radial direction, RD; and the direction at 45° between ED and TD. In order to simulate uniaxial tension tests in different orientation, either the test boundary condition was keep constant with respect to the reference frame, but the texture information was transformed into different reference frame, but the texture information was keep constant with respect to the reference frame, but the texture information was keep constant with respect to the reference frame, but the texture information was transformed into different reference frames. The latter approach was used in this work.

To calculate the flow stresses $(\sigma_{ED}, \sigma_{RD}, \sigma_{TD}, \sigma_{45})$ and r-values $(r_{ED}, r_{TD}, r_{TD}, r_{45})$ in 4 different directions, the crystallographic textures, as measured by orientation imaging microscopy (OIM) provided by the ATC, were used as input to the polycrystal model that

was introduced in Chapter 3. The crystallographic textures were expressed in the reference frame (RD, TD, ED), the radial, tangential, and extrusion directions respectively. Before the polycrystal computations, these textures were slightly rotated in order to recover the expected symmetry due to the material flow.

For simulations, the voce parameters A', B', C' (see Eq.3-24) were determined by a trialand-error method, repeating the polycrystal simulations until the experimental ED stressstrain curve was satisfactorily predicted (see Figure B1).

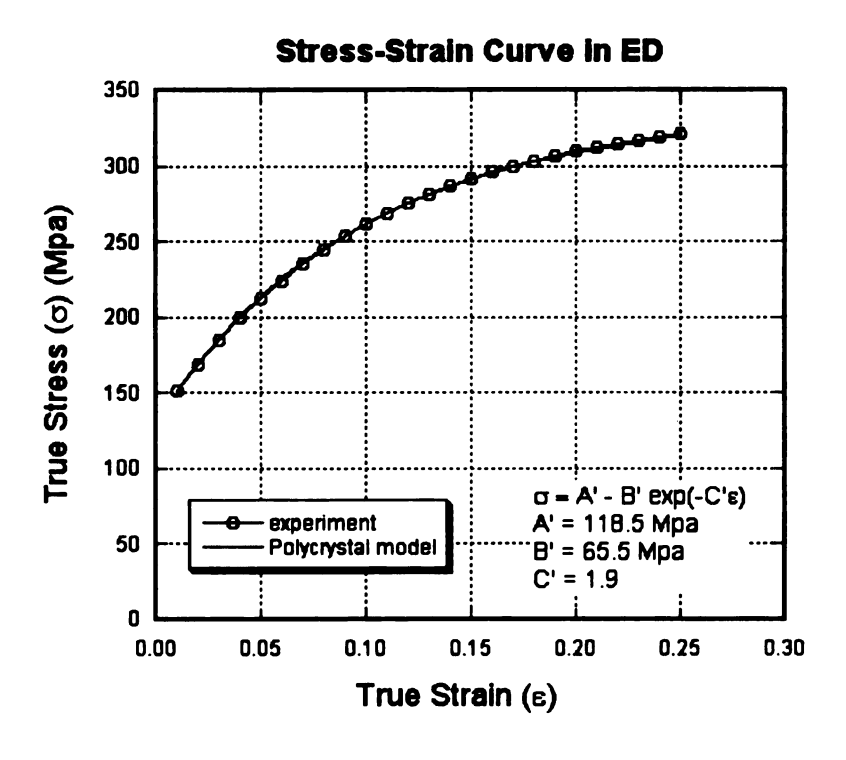


Figure B1 Stress-strain curve (extrusion direction) from polycrystal simulation and experimental result

As mentioned before, to predict the stress-strain curve in other three directions, we have to keep the texture information in reference frame and transfer the boundary condition to different frame. For instance, in the case of uniaxial tension simulation in TD, the strain increment tensor was expressed in the reference frame (RD', TD', ED'). It was transformed in the reference frame (RD, TD, ED) and the stress calculation was carried out by polycrystal model while the input texture orientation was updated with respect to reference frame (RD, TD, ED). The stress result was then transformed back to reference frame (RD, TD, ED). Various possible strain increment tensors (depending on the different r-values) were implemented as input along with texture orientation until approximately uniaxial stress state was reached. Using this approach, the r-value in ED could be obtained. Similarly, r-values for other directions are obtained using a similar approach (See Figure B2).

The work hardening behavior (trends) in the different directions was consistent for all amounts of plastic work (isotropic hardening assumption), the flow stress used to calculate the anisotropy coefficients were determined at the plastic work amount of 50 Mpa mm/mm.

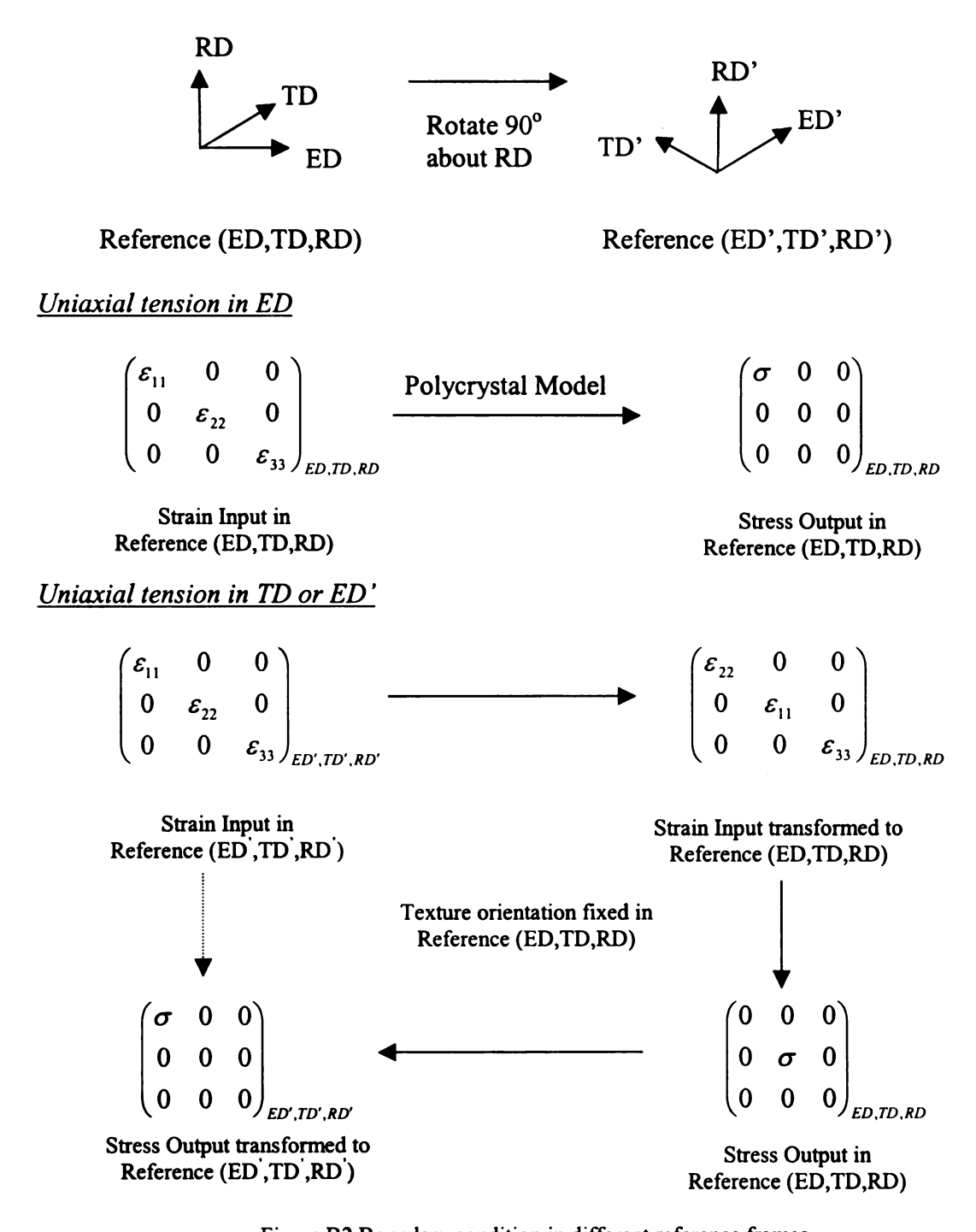


Figure B2 Boundary condition in different reference frames

Appendix C

Predicted yield surfaces based on the proportional loading

Case 1: Uniaxial tension in extrusion direction

Yield Surface Comparison Uniaxial Tension(extrusion direction) (10%) $(\alpha = -0.00025, -0.0001)$ 1.00 0.50 10 0.00 -0.50 alpha=-0.00025 alpha=-0.0001 YS(polycrystal) -1.00 -1.00 -0.50 0.00 _0.50 1.00 1.50 $\sigma_{xx}/\bar{\sigma}$

Figure C1-a

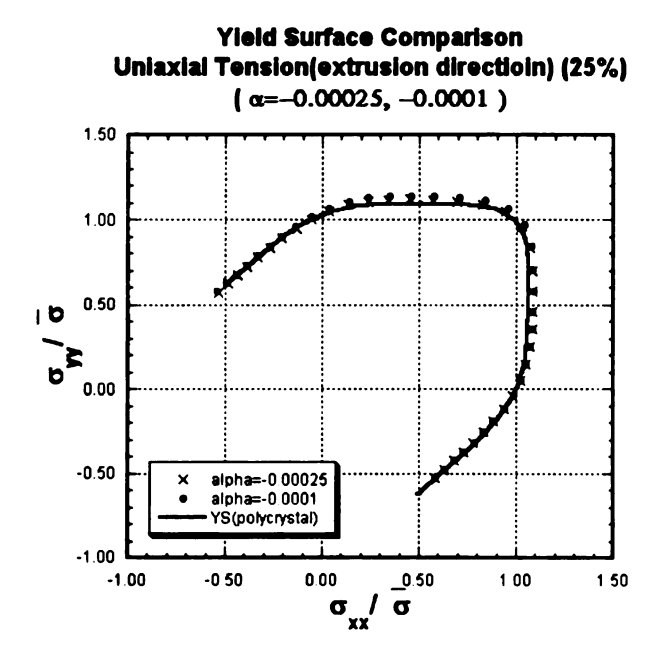


Figure C1-b

Yield Surface Comparison Uniaxial Tension(extrusion direction) (50%) $(\alpha=-0.00025, -0.0001)$ 1.50 1 00 0.50 16 0 00 -0.50 alpha=-0 00025 alpha=-0 0001 YS(polycrystal) -1.00 -1.00 -0.50 0.00 _0.50 1.00 1.50 σ_{xx} σ

Figure C1-c

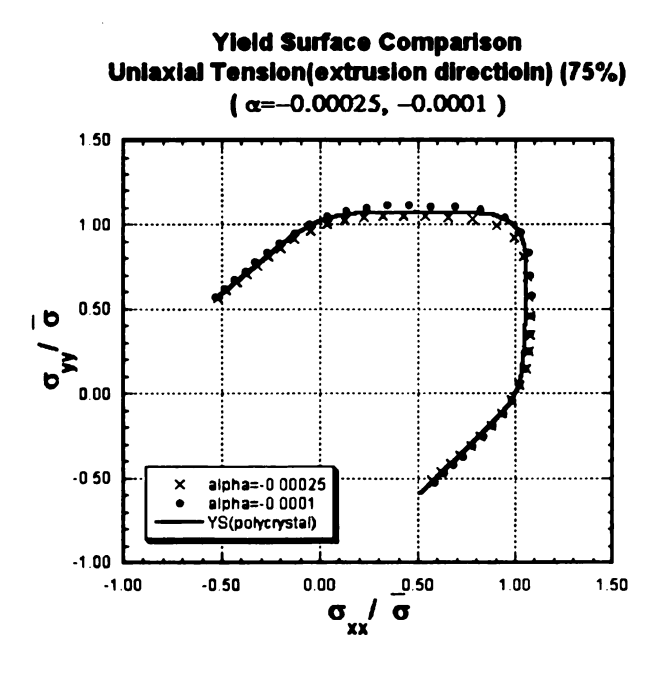


Figure C1-d

Figure C1a-d Yield surface comparison for uniaxial tension (ED)

Case 2: Uniaxial tension in tangential direction

Figure C2-a

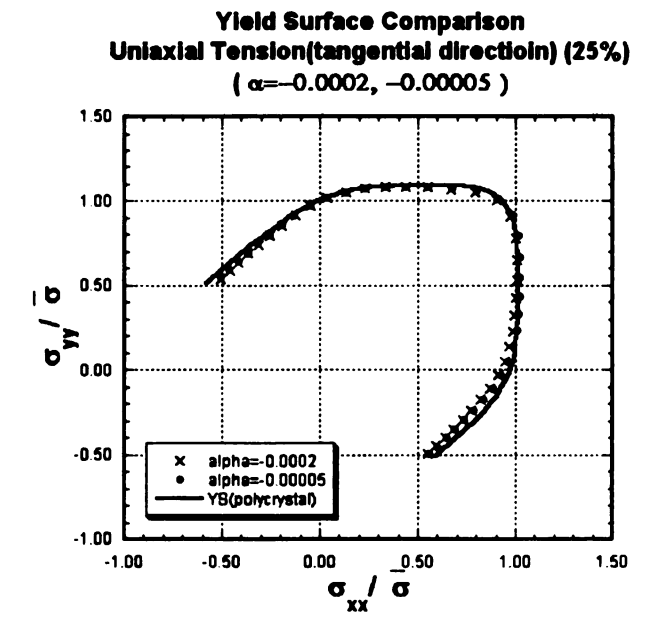


Figure C2-b

Yield Surface Comparison Uniaxial Tension(tangential direction) (50%) $(\alpha=-0.0002, -0.00005)$ 1.50 1.00 0.50 0.00 -0.50 alpha=-0.0002 alpha=-0.00005 YS(polycrystal) _0.50 -0.50 0.00 1.00 1.50 -1.00 σ

Figure C2-c

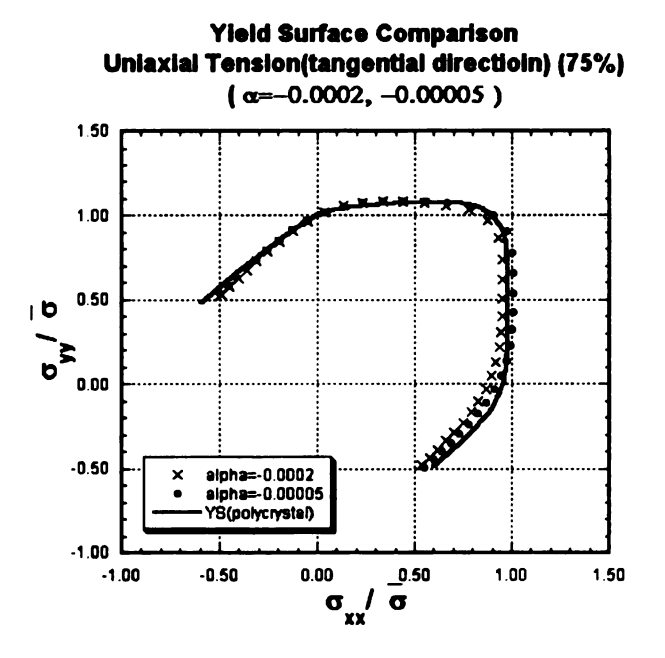


Figure C2-d

Figure C2a-d Yield surface comparison for uniaxial tension (TD)

Case 3: Plane strain ($\epsilon_{22} = 0$)

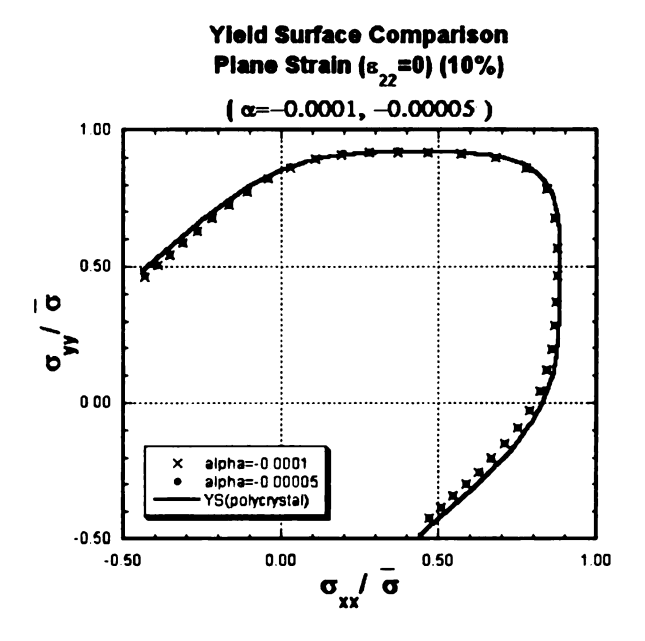


Figure C3-a

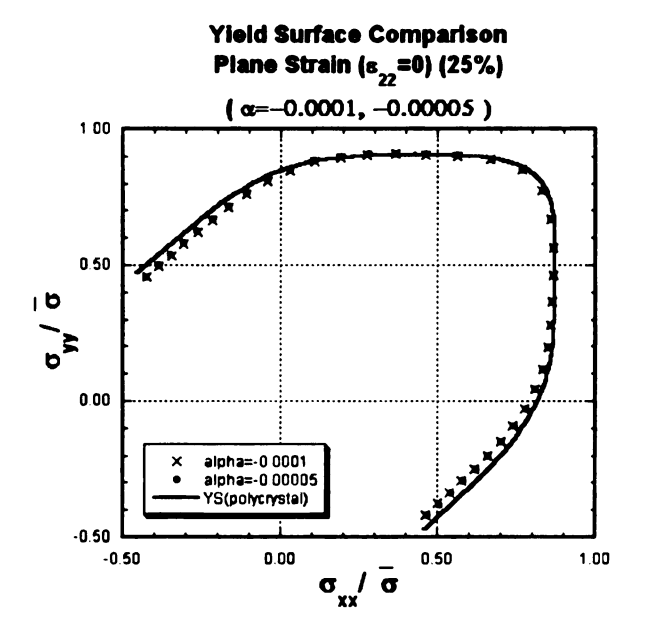


Figure C3-b

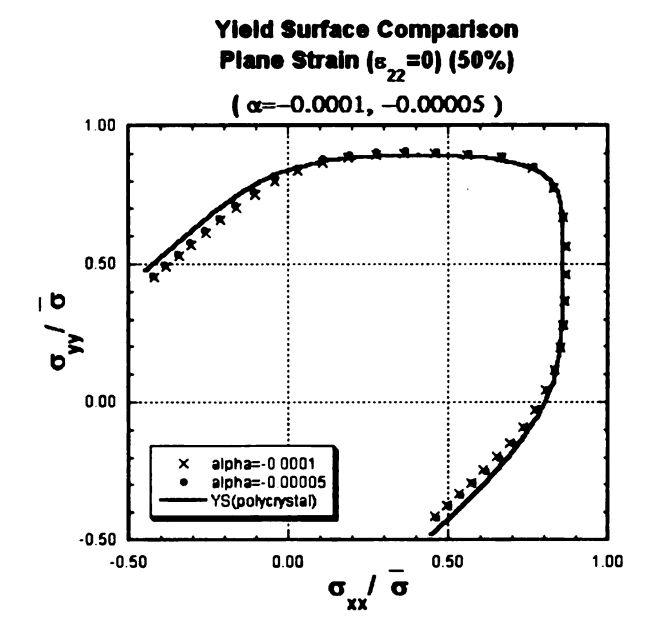


Figure C3-c

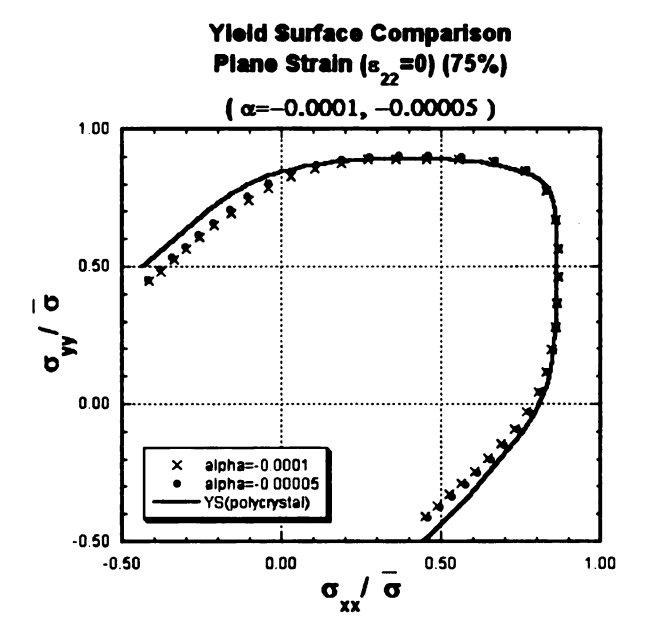


Figure C3-d

Figure C3a-d Yield surface comparison for plane strain ($\epsilon_{\rm 22}=0$)

Case 4: Plane strain ($\epsilon_{11} = 0$)

Yield Surface Comparison Plane Strain (ε₁₁=0) (10%) (α=-0.0001, -0.00005) 100 × alpha=-0.0001 • alpha=-0.00005 • YS(polycrystal) -0.50 0.50 1.00

Figure C4-a

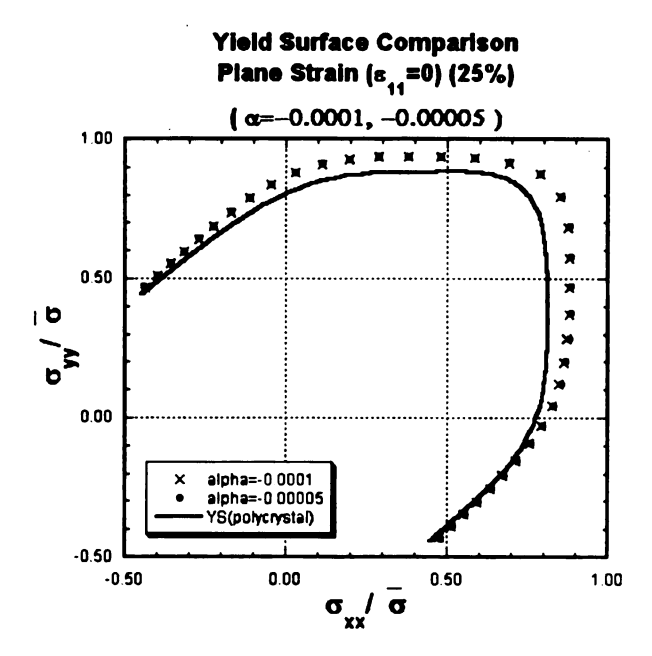


Figure C4-b

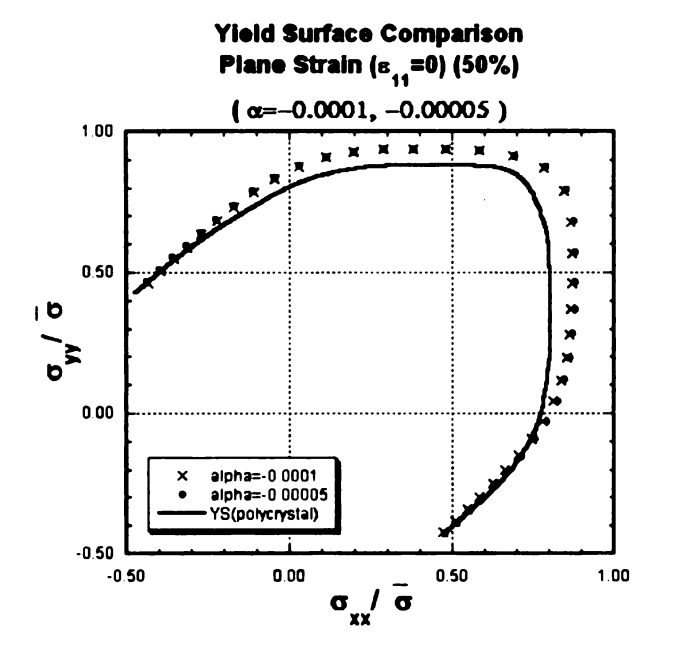


Figure C4-c

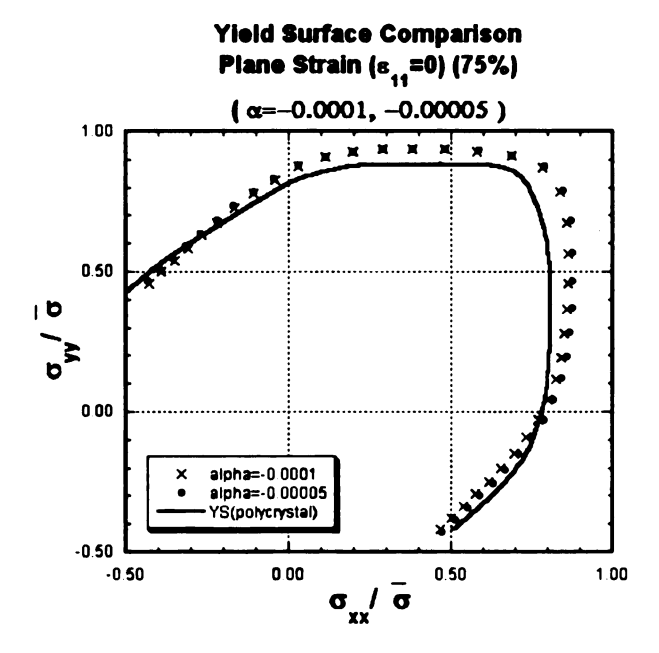


Figure C4-d

Figure C4a-d Yield surface comparison for plane strain ($\epsilon_{11} = 0$)

Case 5: Balanced biaxial tension

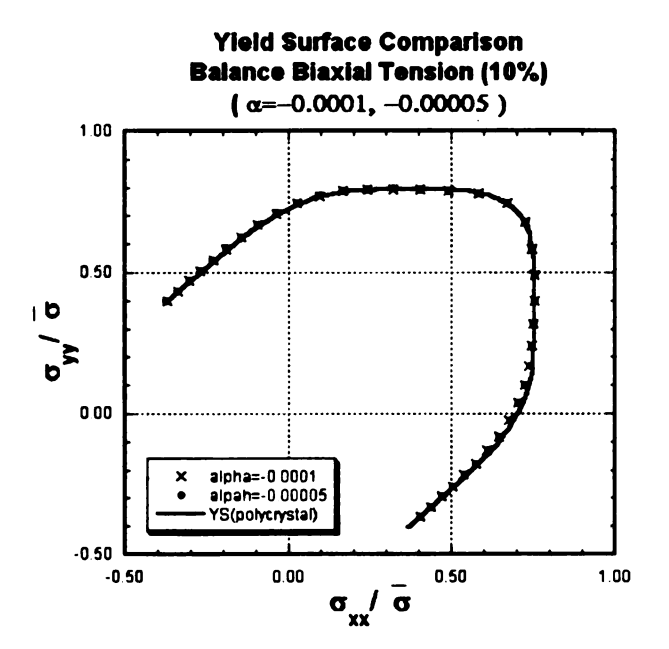


Figure C5-a

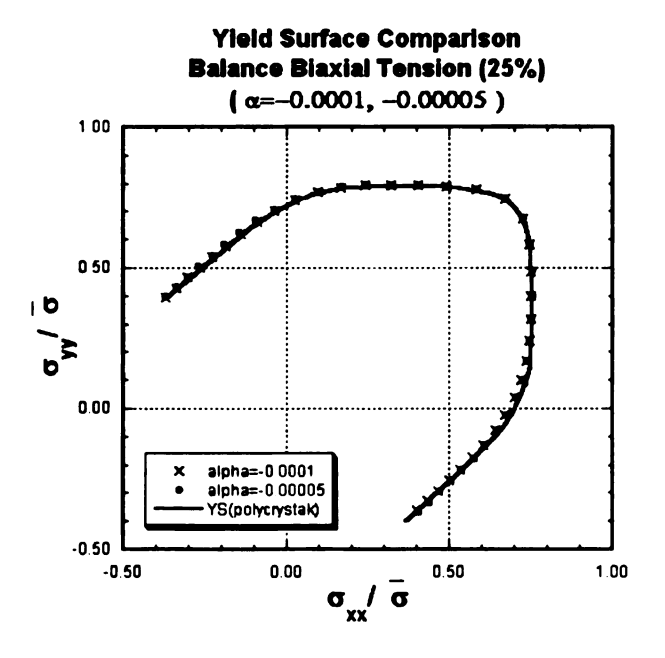


Figure C5-b

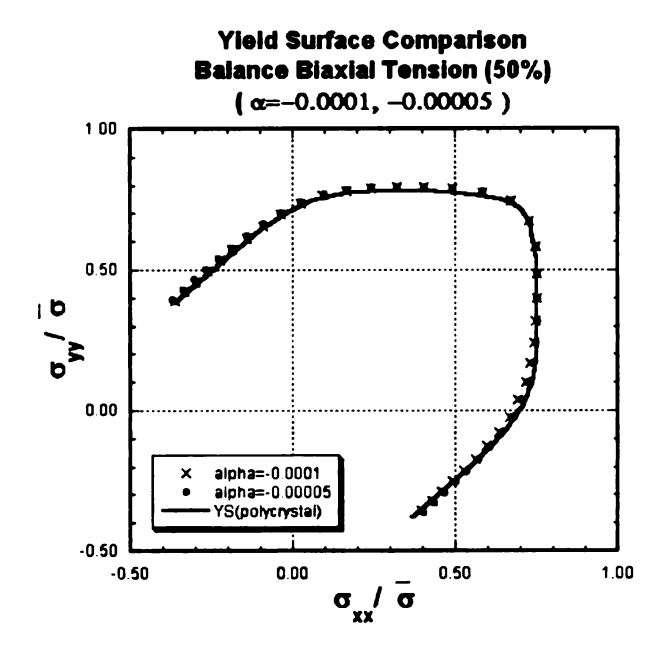


Figure C5-c

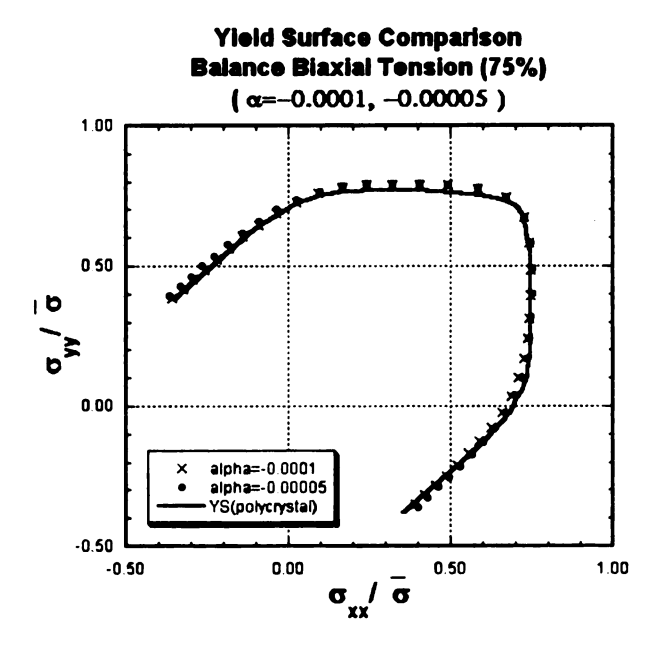


Figure C5-d

Figure C5a-d Yield surface comparison for balanced biaxial tension

REFERENCE

ABAQUS Manual, Hibbit, Karlsson & Sorensen, Inc., Providence, RI, Version 5.8

Ahzi, S., Asaro, R.J. and Parks, D.M. (1993). Application of crystal plasticity theory mechancially processed BSCCO superconductors. Mech. Mater. 15(3). 201-222.

Arminjon, M. (1991). A regular form of the Schmid law. Application to the ambiguity problem. Textures and Microstructures 14, 1121-1128.

Anand, L. and Kothari M. (1996). A computational procedure for rate independent crystal plasticity. J. Mech. Phys. Solids. 44(4), 525-558.

Asaro, R.J. and Needleman, A., (1985). Texture development and strain hardening in rate dependent polycrystals, Acta Metall. 33(16), 923-953.

Asaro, R.J. (1983a). Micromechanics of crystals and polycrystals. Adv. Appl. Mech. 23,1-115.

Asaro, R.J.(1983b). Crystal plasticity. ASME J. Appl. Mech. 50(4B), 921-934.

Asaro, R.J. (1983c). Micromechanics of crystals and polycrystal, Advances in Applied Mechanics, Vol 23, 1-115.

Asaro, R.J. and Rice, J.R. (1977). Strain localization in ductile single crystals. J. Mech. Phys. Solids 25(5), 309-338.

Asnafi N. and Skogsgardh A., (2000). Theoretical and experimental analysis of stoke-controlled tube hydroforming. Material Science and Engineering A-structure, 279, 95-110.

Bassani, J.L. (1977). Yield characterization of metals with transversely isotropic plastic properties. Int. J. Mech. Sci. 19(11), 651-660.

Beaudoin, A.J., Mathur, K.K., Dawson, P.R. and Johnson, G.C., (1993). Three-dimensional deformation process simulation with explicit use of polycrystalline plasticity model, Int. J. Plasticity 9(7), 833-860.

Besdo D. and Wojtasik N.W. (2001). The influence of large torsional prestrain on the texture development and yield surface of polycrystal, Plasticity of Metals, Edited by Steck E. and Ritter R. 131-148.

Barlat, F. and Lian, J. (1989). Plastic behavior and stretchability of sheet metals. Part I: A yield function for orthotropic sheets under plane stress conditions. Int. J. Plasticity 5(1), 51-66.

Barlat, F., Lege, D.J. and Brem, J.C., (1991). "A six-component yield function for anisotropic materials", Int. J. Plasticity 7(7), 693-712.

Barlat, F., Maeda, Y., Chung, K., Yanagawa, M., Brem, J.C., Hayashida, Y., Lege, D.J., Matsui, K., Murtha, S.J., Hattori, S., Becker, R.C., Makosey, S., (1997). Yield function development for aluminum alloy sheets, J. Mech. Phys. Solids 45(11-12), 1727-1763.

Barlat, F., Brem, J.C., Yoon J.W., Chung K., Dick R.E., Lege, D.J., Pourboghrat, F., Choi, S.H., and Chu, E. (2003). Plane stress yield function for aluminum alloy sheets-part 1: theory. Int. J. Plasticity 19(9), 1297-1319.

Becker, R. (1991). Analysis of texture of evolution in channel-die compression—1: Effects of grain interaction, Acta Metall. Mater. 39(6), 1211-1230.

Bishop, J.F.W. and Hill, R. (1951a). A theory of the plastic distortion of a polycrystalline aggregate under combined stresses, Phil. Mag., 42, 414-427.

Bishop, J.F.W. and Hill, R. (1951b). A theoretical derivation of the plastic properties of a polycrystalline face-centered metal, Phil. Mag., 42, 1298-1307.

Bishop, J.W.F., (1953). A theoretical examination of the plastic deformation of crystals by glide, Phil. Mag. 44, 51-64.

Chen K.K. (2000). Deformation, strain and stress in expansion of tubes in hydroforming, SAE Technical Paper Series 2000-01-0769.

Dao, M. and Li, M., (2001). A micromechanics study on strain localization induced fracture initiation in bending/hemming using crystal plasticity models. Phil. Mag. A 81(8), 1997-2020.

Davies R, Grant G, Herling D and Smith M (2000). Formability investigation of aluminum extrusions under hydroforming conditions, SAE Technical Paper Series 2000-01-2675.

Dawson, P.R. and Beaudoin, A.J., (1998). Finite element simulations of metal forming, Ed. Kocks, U.F., Tome, C.N. and Wenk, H-R., Cambridge University Press, pp. 532-558.

Dawson PR and Marin EB, (1998). Computational mechanics for metal deformation process using polycrystal plasticity, Advances in applied mechanics vol. 34, pp77-169.

Dieter G.E. (1976). Mechanical Metallurgy, Second Edition, pp143.

Dohmann, F. and Hartl, Ch., (1997). Tube hydroforming: research and practical application, J. Mater Process Tech 71(1) 174-186.

Ewing, J.A. and Rosenhain, W. (1900). The crystalline structure of metals. Philos. Trans. R. Soc. London 193, 353-375.

Franciosi, P., Berveiller, M., Zaoui, A. (1980). Latent hardening in copper and aluminum single crystals, Acta Metallurgica, 28(3), 273-283.

Gambin, W., (1991). Plasticity of crystals with interacting slip systems, Engineering Transactions 39, 3-4, 303.

Gambin, W., (1992). Refined analysis of elastic-plastic crystals, Int. J. Solids Struct. 29(16), 2013-2021.

Gambin, W. and Barlat, F., (1997). Modeling of deformation texture based on rate independent crystal plasticity, Int. J. Plasticity 13(1-2), 75-85

Gelin JC and Labergere C, (2002). Application of optimal design and control strategies to the forming of thin walled metallic components, J. of Mater Process Tech 125, 565-572.

Gotoh, M. (1977). Theory of plastic anisotropy based on a yield function of fourth order(plane stress state). Int. J. Mech. Sci. 19(9), 513-520.

Guan, Y. Pourboghrat F. and Barlat F. (2003). Polycrystal modeling and finite element analysis of hydroforming of aluminum extruded tubes. Proceeding of the NSF design service and manufacturing Grantees and Research Conference, University of Alabama.

Guan, Y. Pourboghrat F. (2003). Fourier series based finite element section analysis of tube hydroforming-part 1: plane strain model. submitted to Engineering Computations.

Hershey, A.V. (1954). The plasticity of an isotropic aggregate of anisotropic face centered cubic single crystals. J. Appl. Mech. 21, 241-249

Hill, R. (1948). A theory of the yielding and plastic flow of anisotropic metals. Proc. R. Soc. London 193A, 281-297.

Hill, R. (1966). Generalized constitutive relations for incremental deformation of metal crystals by mutlislip. J. Mech. Phys. Solids 14, 95-102.

Hill, R. and Rice, J.R. (1972). Constitutive analysis of elastic-plastic crystal at arbitary strain. J. Mech. Phys. Solids 20(6), 401-413.

Hill, R. (1979). Theoretical plasticity of textured aggregates. Math. Proc. Camb. Phil.Soc. London 85, 179-191.

Hill, R. (1990). Constitutive modeling of orthotropic plasticity in sheet metals. J. Mech. Phys. Solids, Vol. 38(3), 405-417.

Hosford, W.F. (1972). A generalized isotropic yield criterion. J. Appl. Mech. 39(2), 607.

Hsu, Tze-Chi and Chu, Chan-Hung, (1995). A finite element analysis of sheet metal forming processes, J Mater Process Tech 54(1-4), 70-75.

Hu, P.,Liu, Y.Q., Li, Y.X. and Lian, J., (1997). Rigid viscoplastic finite element analysis of the gas-pressure constrained bulging of superlastic circular sheets into cone disk shape dies, Int. J. Mech. Sci. Vol. 39, No.4, pp. 487-496.

Hu, WL, (2000). Experimental strain-hardening behaviors and associated computational models with anisotropic sheet metals, Computational Materials Science, 18(3-4), 355-361.

Hull D and Bacon DJ (1984). Introduction to dislocation, Third Edition.

Kalidindi, S.R. Bronkhorst, C.A. and Anand, L. (1992). Crystallographic texture in bulk deformation processing of fcc metals, J. Mech. Phys. Solids 40(3), 537-569.

Karafillis, A.P., Boyce, M.C. (1993). A general anisotropic yield criterion using bounds and a transformation weighting tensor. J. Mech. Phys. Solids 41(12), 1859-1886.

Kim J and Kang BS (2002). Implementation of backward tracing scheme of the FEM for design of initial tubular blank in hydroforming, J. of Mater Process Tech 125, 839-848.

Kocks U.F. et al (2000). Texture and anisotropy, Cambridge University Press.

Kopacz I, Toth L.S., Zehetbauer M. and Stuwe HP, (1999). Large strain hardening curves corrected for texture development, Modeling Simul. Mater. Sci. Eng.,7(5), 875-891.

Kuroda M., Tvergarrd V., (1999). Use of abrupt strain path change for determining subsequent yield surface: illustrations of basic idea, Acta mater., 47(14), 3879-3890.

Kuwabara T., Kuroda M., Tvergarrd V. and Nomura K. (2000). Use of abrupt strain path change for determining subsequent yield surface: experimental study with metal sheets. Acta mater., 48(9), 2071-2079.

Lademo, O.G., Hopperstad O.S. and Langseth M. (1999). An evaluation of yield criteria and flow rules for aluminum alloys. Int. J. Plasticity, 15(2), 191-208.

Lebensohn, R.A. and Tome, C.N. (1993). A self-consistent anisotropic approach for the simulation of plastic deformation and texture development in polycrystals – Application to zirconium alloys, Acta Metall Mater 41(9), 2611-2624.

Lee, C.H., (2002). Prediction of deformation induced anisotropy in profile extrusion of aluminum alloys, Ph.D. Dissertation.

Lei LP, Kim J and Kang BS (2002). Bursting faiture prediction in tube hydroforming process by using rigid-plastic FEM combined with ductile fracture criterion, Int. J. Mech. Sci. 44(7), 1411-1428.

Lloyd, D.J., Sang, H., (1979). The influence of strain path on subsequent mechanical properties - Orthogonal tensile paths. Metall. Trans. A 10, 1767-1772.

Logan, R.W. and Hosford, W.F. (1980). Upper-bound anisotropic yield locus calculations assuming <111> pencil glide. Int. J. Mech. Sci. 22(7), 419-430.

Lopes, A. B., Barlat, F., Gracio, J. J., Duarte, JFF, Rauch, E. F., (2003). Effect of texture and microstructure on strain hardening anisotropy for aluminum deformed in uniaxial tension and simple shear, Int. J. Plasticity 19(1), 1-22.

MacDonald, BJ and Hashmi MSJ, (2001). Three-dimensional finite element simulation of bulge forming using a solid bulging medium, Finite elements in analysis and design 37(2), 107-116.

Manabe K and Amino M (2002). Effects of process parameters and material properties on Deformation process in tube hydroforming, J. of Mater Process Tech 123(2), 285-291.

Mandel, J. (1965). Generalisation de la theorie de la plasticite de W. T. Koiter. Int J. Solids Struct. 1, 273-295.

Meyers M.A. and Chawla K.K., (1984). Mechanical Metallurgy, Prentice-Hall.

Molinari, A., Canova, G.R. and Ahzi, S. (1987). A self-consistent approach of the large deformation polycrystal viscoplasticity, Acta Metall Mater 35(12), 2983-2994.

Molinari, A., Ahzi, S. and Kouddane R (1997). On the self-consistent modeling of the elastic-plastic behaviour of polycrystals, Mech Mater 26(1) 43-62.

Ni, C.M., (1994). Stamping and hydroforming process simulation with a 3D finite element code, SAE Paper #940753, SAE SP-1021.

Noh, T.S. and Yang, D.Y., (1998). A general formulation for hydroforming of arbitrarily shaped boxes and its application to hydroforming of an elliptic-circular box, Journal of Manufacturing Science and Engineering-T ASME, August, 120(3) 481-488.

Pan, J. and Rice, J.R. (1983). Rate sensitivity of plastic flow and implication for yield-surface vertices. Int. J. Solids Struct. 19(1), 973-987.

Phillips A. and Tang J.L. (1972). The effect of loading path on the yield surface at elevated temperatures, Int. J. Solids Struct., 8, 463-474.

Pourboghrat F. and Barlat F. (2002). Texture evolution during hydroforming of aluminum extruded tubes, NSF-Design conference, Puerto Rico.pp1958-1973.

Rice, J.R. (1971). Inelastic constitutive relations for solids: an internal variable theory and its application to metal plasticity. J. Mech. Phys. Solids 19(6), 433-455.

Sachs, G. (1928). Z. Verein Deut. Ing. 72, 134.

Sang, H., Lloyd, D.J., (1979). Influence of biaxial prestrain on the tensile properties of three aluminum alloys, Metal. Trans. A10(11), 1773-1776.

Sharma M, Guan Y and Pourboghrat F (2003). "Fourier series based finite element section analysis of tube hydroforming-Part2: axisymmetric model", submitted to Engineering Computations.

Taylor, G.I. and Elam, C.F. (1925). The plastic extension and fracture of aluminum crystals. Proc. R. Soc. London, Sec. A 108, 28-51.

Taylor, G.I.(1934). The mechanism of plastic deformation of cyrstals. Part I. –theoretical. Proc. R. Soc. London, Sec. A 145. 362-387.

Taylor, G.I.(1938). Plastic strain in Metals, J. Inst. Met. 62, 307-324.

Tome, C.N. and Canova, G.R., (1998). Self-consistent modeling of heterogenous plasticity, in Texture and Anisotropy, Ed. Kocks, U.F., Tome, C.N. and Wenk, H-R., Cambridge University Press, pp. 466-510.

Tome, C.N. (1999). Self-consistent polycrystal models: a directional compliance criterion to describe grain interactions. Modelling Simul. Mater. Sci. Eng. 7(5), 723-738.

Trana K (2002). Finite element simulation of the tube hydroforming process—bending, preforming and hydroforming. J. of Mater Process Tech 127(3), 401-408.

Vari-Form Inc., The ABCs of Hydroforming.

Von Mises (1928). Z. Angew. Math. Mech., 8, 161.

Wu LW and Yu Y (1996). Computer simulations of forming automotive structural parts by hydroforming process, Numisheet 96.

Wu, P.D., Jain M., Savoie, J., MacEwen S.R., Tugcu P. and Neale K.W. (2003). Evaluation of anisotropic yield functions for aluminum sheets. Int. J. Plasticity 19(1), 121-138.

Yang JB, Jeon BH and Oh SI. (2001). Design sensitivity analysis and optimization of the hydroforming process. J. of Mater Process Tech 113(1-3), 666-672.

Yoon, J.W., F. Barlat, K. Chung, F. Pourboghrat, D.Y. Yang (2000). Earing prediction based on asymmetric nonquadratic yield function, Int. J. Plasticity 16(9), 1075-1104

